The design of a friction-based tissue transportation mechanism for Minimally Invasive Surgery

by

Yinte Verberne

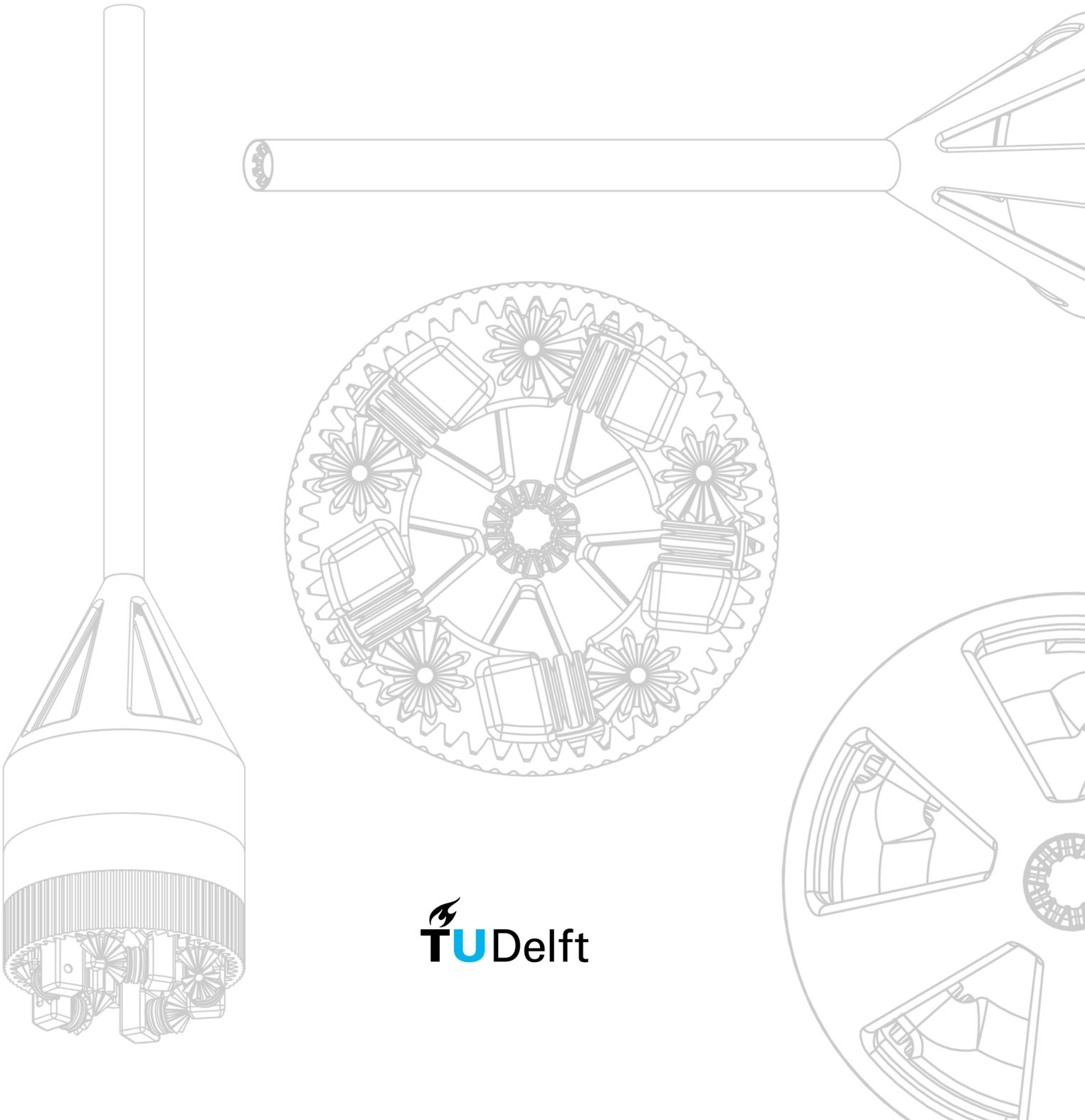

TU Delft

The design of a friction-based tissue transportation mechanism for Minimally Invasive Surgery

by

Yinte Verberne

September 29, 2022

to obtain the degree of
MSc Mechanical Engineering
at the Delft University of Technology

to be defended on
the 6th of October 2022 at 12:00h

Studentnumber:	4541758
Project duration:	March 2022 - October 2022
Thesis supervisors:	Dr. Ir. A. Sakes
	Ir. V. Kortman
Thesis committee:	Dr. T. Horeman (chair)
	Dr. J. Jovanova
	Ir. V. Kortman
	Dr. Ir. A. Sakes

TU Delft

Contents

1 Introduction **1**
- 1.1 Tissue transport in Minimally Invasive Surgery . . . 1
- 1.2 State of the Art . . . 2
- 1.3 Prior work . . . 2
- 1.4 Problem analysis . . . 3
- 1.5 Goal and structure . . . 3

2 Ideation **4**
- 2.1 Design requirements . . . 4
- 2.2 Design structuring . . . 5
- 2.3 Conceptual designs . . . 6
  - 2.3.1 Concept 1 - Transport due to inertia forces . . . 6
  - 2.3.2 Concept 2 - Transport due to applied forces . . . 6
  - 2.3.3 Concept 3 - Friction based transport . . . 7
- 2.4 Final conceptual design . . . 8

3 Final Design **9**
- 3.1 Overview of design concept . . . 9
  - 3.1.1 F1 - Enable tissue transport through thread . . . 11
  - 3.1.2 F2 - Enable thread connection . . . 11
  - 3.1.3 F3 - Enable continuous thread rotation . . . 12
  - 3.1.4 F4 - Enable smooth actuation . . . 14
  - 3.1.5 F5 - Ensure thread positioning . . . 16
  - 3.1.6 F6 - Ensure thread tension . . . 16
  - 3.1.7 F7 - Ensure manufacturability . . . 18
  - 3.1.8 F8 - Ensure compatibility for Minimally Invasive Surgery . . . 19
- 3.2 Final prototype . . . 20

4 Experimental validation **21**
- 4.1 Goal . . . 21
- 4.2 Experiment variables . . . 21
  - 4.2.1 Independent variables . . . 21
  - 4.2.2 Dependent variables . . . 22
- 4.3 Experimental setup . . . 23
- 4.4 Experimental protocol . . . 24
- 4.5 Data analysis . . . 24
- 4.6 Results . . . 25
  - 4.6.1 Transportation velocity . . . 25
  - 4.6.2 Transportation efficiency and reliability . . . 27

5 Discussion **28**
- 5.1 Summary of main findings . . . 28
- 5.2 Limitations . . . 30
  - 5.2.1 Device limitations . . . 30
  - 5.2.2 Experiment limitations . . . 30
- 5.3 Recommendations . . . 32
  - 5.3.1 Redesigns enhancing force distribution . . . 32
  - 5.3.2 Redesigns enhancing material implementation . . . 33
  - 5.3.3 Redesign tensioning mechanism . . . 34

6 Conclusion **35**

A Appendices **39**
A.1 Aspiration catheters . . . 39
A.2 Prior work . . . 40
A.3 Design requirements . . . 41
A.4 Ideation sketches . . . 42
A.5 Conceptual design validation . . . 44
A.5.1 Concept 1 - Transport due to inertia forces . . . 44
A.5.2 Concept 2 - Transport due to applied forces . . . 46
A.5.3 Concept 3 - Friction based transport . . . 47
A.6 Assembly . . . 48
A.7 Tissue phantoms . . . 49
A.8 Instrument failure . . . 50
A.9 Experiment data . . . 50
A.10 Additive manufacturing . . . 54
A.11 Forces bevel gears . . . 54
A.12 Components . . . 55

The design of a friction-based tissue transportation mechanism for Minimally Invasive Surgery

by

Yinte Verberne

September 29, 2022

Abstract

The surgical procedure of tissue extraction from the human body for precautionary or curative measures is common in many medical fields. Currently, aspiration catheters are the golden standard, enabling removal by means of a suction force. By Sakes et al. [27], an alternative mechanism is proposed, transporting tissue based on friction, inspired by the egg-laying structure of wasps. Challenges within these devices comprise clogging and damage prevention, achieving adequate transportation rates, transportation of tissue with differing elasticity properties and satisfying the dimensional restrictions of Minimally Invasive Surgery (MIS). Due to the vital impact of MIS, a tissue extraction device overcoming the previously mentioned barriers is highly desirable. The goal of this research is stated as follows, *'design of a continuous tissue transportation mechanism compatible for MIS in which the transportation velocity is independent of tissue elasticity within the young's modulus range of 1-110 kPa'*. The stated elasticity span resembles a large range of tissue that can be encountered during MIS, whilst aspiration catheters are assumed to be suitable for the removal of liquids. Tissue extraction and retrieval are not included within the scope.

To achieve the stated objective, novel ideas are generated from both a dynamic and nature-based perspective and assessed by means of rapid prototyping. Within the final prototype, a cylindrical conveyor belt is created, consisting of a thread wrapped along a tubular body. Due to friction between the thread and tissue, the latter is transported whenever continuously rotating the thread in the direction of removal. Experiments are performed with the proof of principle prototype to investigate the effects of different rotational velocities, instrument orientation, and tissue shape on the transportation velocity of tissue and the corresponding efficiency and reliability. Maximum mean mass transportation rates of 7.75∓0.48, 8.43∓1.50, and 8.90∓0.56 $\frac{g}{min}$ are attained, as a result of transporting tissue phantoms with a young's modulus of approximately 1-10, 55, and 100-110 kPa respectively. Whether statistically, variance in transportation rates between these categories appears is not determined, as equivalent power supply voltages did not result in identical rotational velocities due to varying thread tension. However, as the transportation velocities match rates of clinically available morcellator and perfect reliability is attained, the potency of the designed mechanism as an alternative for aspiration-based instruments is demonstrated.

Keywords: Medical device design – Tissue extraction – Tissue elasticity – Conveyor belt

1 Introduction

1.1 Tissue transport in Minimally Invasive Surgery

Tissue extraction from the human body is a procedure performed in many medical fields such as cardiology [23], gynaecology [3], and neurology [34]. The removal can serve as precautionary or curative measures [31]. Within the former, (suspicious) tissue is removed for diagnostic purposes. Sufficient sample quality is desired for trustworthy analysis. Alternatively, diseased or obstructing tissue can be removed, such as tumorous tissue or thrombus, respectively.

Transportation mechanisms such as flexible graspers and aspiration-based devices all facilitate tissue extraction. These working principles are implemented in medical instruments such as bioptomes, stent-retrievers, laparoscopic devices and catheters [27]. For example, the performance of biopsy can be aided through colonoscopy [33] whilst percutaneous aspiration catheters are often implemented for the removal of thrombus. As shorter surgery durations are beneficial in order to reduce both anaesthesia time and operation costs [27], it can be substantiated that continuous transportation mechanisms are advantageous. In other words, removal in an ongoing stream, instead of in a step-wise manner like aided through a grasper.

Over the past two decades, traditionally open surgery is gradually being replaced by Minimally Invasive Surgery (MIS) [8]. Within this procedure, tissue damage is limited by making a small incision through which a slender medical instrument is inserted. For example, according to Perigli et al., incision lengths for neck surgeries are reduced by 4.5-6.5 centimetres when making use of these techniques, as opposed to conventional manners [22]. Alternatively, the device can be inserted through existing body orifices, dependent on the location of extraction. Corresponding advantages of MIS are amongst other things, reduced surgery duration, shorter hospital stays, less chance of wound infection, decreased post-operative pain, and improved cosmetic results when compared to open surgery [12] [26].

1.2 State of the Art

Currently, aspiration catheters are most commonly used in practice to facilitate tissue transportation and are therefore referred to as the golden standard [27]. The device consists of a flexible tubular body in which a suction lumen is present. A negative pressure is applied by the suction tool attached to the proximal end of the catheter, transferring the tissue in front of the tip through the lumen outside of the human body. The corresponding suction force can be calculated with the use of Equation 1. Within this formula, F represents the suction force in $[N]$, P the pressure in $[\frac{N}{m^2}]$ and A the surface area of the aspiration port in $[m^2]$. The resulting forces during the removal of tissue are shown in Figure 1. Due to the small diameter of aspiration catheters, MIS is enabled. Additional information concerning the design of aspiration catheters and the most commonly used devices can be read within Subsection A.1.

$$F = P * A \tag{1}$$

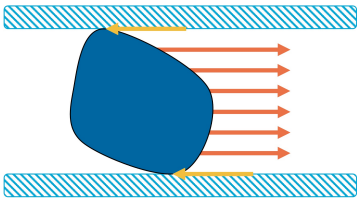

Figure 1: Schematic representation of the forces within an aspiration catheter. The orange lines represent the suction force in the desired direction of translation whilst the yellow lines resemble friction between the transported tissue and the shaft of the device. The effect of gravity is neglected.

1.3 Prior work

Within, Sakes et al. [27], an alternative mechanism for aspiration-based devices is proposed, in which tissue is transported by making use of the physical phenomenon of friction, see Subsection A.2 for a schematic representation. Inspired by the egg-laying structure of the wasp, the device consists of six reciprocating semi-cylindrical blades, which either move forwards or backwards, in a specific moving sequence. Tissue is transported within the tubular body of the device, formed by these blades. Assuming that all blades contribute equally to the total friction with the tissue, the tissue will translate in the direction of the majority of the concerning. Transportation in the opposite direction can be prevented by limiting the number of blades retreating simultaneously, whilst keeping the remaining stationery. In a follow-up study by de Kater et al., the design is altered, introducing a flexible shaft with a similar working principle [15].

1.4 Problem analysis

Even though aspiration-actuated catheters are most commonly used, multiple challenges remain. In order to meet the dimensional restrictions for MIS, miniaturization of medical devices is desired. However, sufficient pressure differential within the shaft of the aspiration catheter is challenging whilst further downscaling the diameter (Equation 1) and enlarging the working length [29]. Further, aspiration catheters are prone to clogging [27]. This phenomenon occurs whenever the friction force between the extracted tissue and shaft exceeds the suction force. These forces are indicated in Figure 1. This subsequently emphasizes the dependency of the reliability of aspiration-based transportation on tissue composition. Stiffer clots are less likely to adjust their shape and therefore experience a higher risk of getting clamped within the shaft of the device [19]. Further, inconsistent suction forces can lead to damaging both the surrounding and transported tissue [27]. The former occurs when undesired tissue is sucked into the tube. The latter is especially a drawback in the case of tissue extraction for diagnostic purposes.

Concerning the design of Sakes et al., even though the mechanism shows promising results, the transportation rate of the tissue is highly dependent on tissue elasticity, showing a statistically significant difference [27]. Within this study, it is hypothesized that soft incoherent tissues potentially deform or shear near the blade surface. On the other extreme, stiff, incompressible, tissues lack tissue deformation. This results in insufficient contact points between the concerning and reciprocating blades for friction-based extraction. The paper mentions an overall transportation rate of 50 to 162 lower than clinically available devices.

To summarize, several challenges can be encountered whilst designing a tissue transportation mechanism. Potential barriers include dimensional restrictions within MIS, tissue elasticity variety, clogging prevention, damage prevention to both surrounding and transported tissue and achieving adequate transportation rates.

1.5 Goal and structure

Based on the challenges of current tissue transportation mechanisms, the goal of this research is defined as follows.

Goal: *design of a continuous tissue transportation mechanism compatible for MIS in which the transportation velocity is independent of tissue elasticity within the young's modulus range of 1-110 kPa.*

The stated tissue elasticity range resembles a large span of tissue that can all be encountered during MIS and will be further elaborated within Subsection 2.1. Continuous removal is desired as time is critical within MIS. Note that the scope of this study does not include the procedure of tissue insertion and extraction. Emphasis is merely paid to the transportation principle of the tissue, assuming that the concerning is already present within the tubular body.

The paper is structured as follows. Initially, the goal of the research is clarified by means of a list of design requirements. Both demands and wishes are elaborated and structured based on functional and procedural specifications. Subsequently, novel ideas are generated and structured through a dynamic and nature-based perspective. The resulting conceptual designs are validated by means of rapid prototyping, resulting in a final conceptual design selected based on feasibility. This final conceptual design is advanced in an iterative manner and elaborated within this report based on the functionality features of the device. Subsequently, the resulting proof of principle prototype is validated by means of experiments. The results are argued within the discussion, including design and experiment limitations and recommendations. Lastly, the report is terminated with a conclusion.

2 Ideation

2.1 Design requirements

Prior to the design phase, the requirements that the transportation device should fulfil were drawn up. Functional and procedural requirements (R) are distinguished. A complete overview with corresponding wishes (W) can be found within Subsection A.3. Within the following list, all items containing numerical conditions are elaborated, and the selected boundary values are highlighted.

- **R2, tissue elasticity:** the mechanical properties of tissue both vary amongst different types and change when diseased. For example, within the research executed by Yu et al., the young's modulus of a tumour within a kidney is approximately 20 kPa higher when compared to healthy parts [35]. Further, strain rates non-linearly influence the measured tissue elasticity [4]. The working range for the to-be-developed transportation mechanism is selected to be 1-110 kPa. This represents a large range of tissues and organs, from brain tissue and adipose tissue at low strain rates (+- 1 kPa [4]) to fibrous tissue such as tendons (51.5 ± 25.1 kPa [2]), which can all be encountered during MIS. The rounded highest measured value within the research of Arda et al., 110 kPa, is selected as upper boundary for the transportation mechanism working range [2]. Aspiration catheters are assumed to be suitable for the removal of liquids. Therefore, this form of matter is excluded.

- **R3, transportation rate:** flow rates of ten commercially available catheters vary between 61.8 and 264.6 $[\frac{g}{min}]$ [18]. These velocities are achieved during the suctioning of water and are thus not representative of the removal of solid tissue. More indicative, the transportation rates of clinically available morcellator vary between 6.2 to 40.4 $[\frac{g}{min}]$ during laparoscopic surgery [5]. Within the wasp-inspired transportation mechanism developed by Sakes et al., the highest transportation rate, 0.25 +- 0.04 $[\frac{g}{min}]$, is achieved for tissue with a young's modulus of approximately 55 kPa [27]. This value is selected as a minimum velocity for the development of the new mechanism, with a desire to reach the values of the clinically available morcellator.

- **R4, reliability:** this variable is of extreme importance within the medical industry due to the vital impact of such procedures. To ensure safety, the reliability of the device is expected to be exquisite. As the goal is to design a transportation mechanism, reliability is defined as the ability to transport tissue through the tubular body of the device, from the tip to the handle, with respect to the total amount of attempts. The value is ought to be 90 percent at a minimum within this research, to indicate the potency of the design.

- **R5, diameter:** outer diameters of aspiration catheters typically vary between three and six french gauge $[F]$ [18], representing a diameter of one to two millimetres respectively. However, dependent on the medical procedure, other dimensions apply. For example, the diameter of commonly used colonoscope is approximately thirteen millimetres [11]. Within this research, producibility is prioritised in order to deliver a proof of principle prototype. With this in mind, the tubular body is required to have the following maximum and minimum dimensions respectively; $\varnothing_{\text{outer}} = 10$ mm and $\varnothing_{\text{inner}} = 5$ mm.

- **R6, working length:** the commercially available catheters previously referred to enable a working length varying between 153 and 125 centimeters [18]. The working length of the three most commonly used thrombectomy aspiration catheters lies within this range, twice at a value of 140 and once with a length of 145 centimetres [21]. For the mechanism designed within this research, the lower bound is selected as the minimum value, whilst the upper bound is desirable.

- **W6, bendability:** contrary to the instruments used during laparoscopic surgery, catheters consist of a flexible shaft. This makes it possible for the tubular device to bend around obstacles within the body. According to Li et al., the smallest curvature a standard push-catheters can traverse is 90 degrees [16]. Within the study executed by de Kater et al., the performance of the flexible wasp-inspired tissue transport mechanism was tested at angles of 30 and 60 degrees, both over a length of eight centimetres, showing no statistical influence on the transportation rate of the tissue [15]. For the design within this research, bendability is formulated as a wish. More specifically, the upper bound of 90 degrees is formulated as desirable whilst the lower values, indicating a higher degree of bendability, are even more advantageous.

2.2 Design structuring

During the ideation phase, initially, the problem is encountered from a dynamic perspective. The forces illustrated in Figure 1 served as a foundation to identify design variables resulting in a similar dynamic situation. The most principal ones are systematically displayed within the table in Figure 2, note that gravity is neglected. By combining different elements of each row, ideas were developed. As an example, the characteristics of the previously discussed aspiration catheter and wasp-inspired friction-based tissue transportation device are indicated. Additionally, the corresponding combinations of the selected conceptual designs are included, which will be elaborated on in the following section. Several ideation sketches developed within this phase are shown within Subsection A.4.

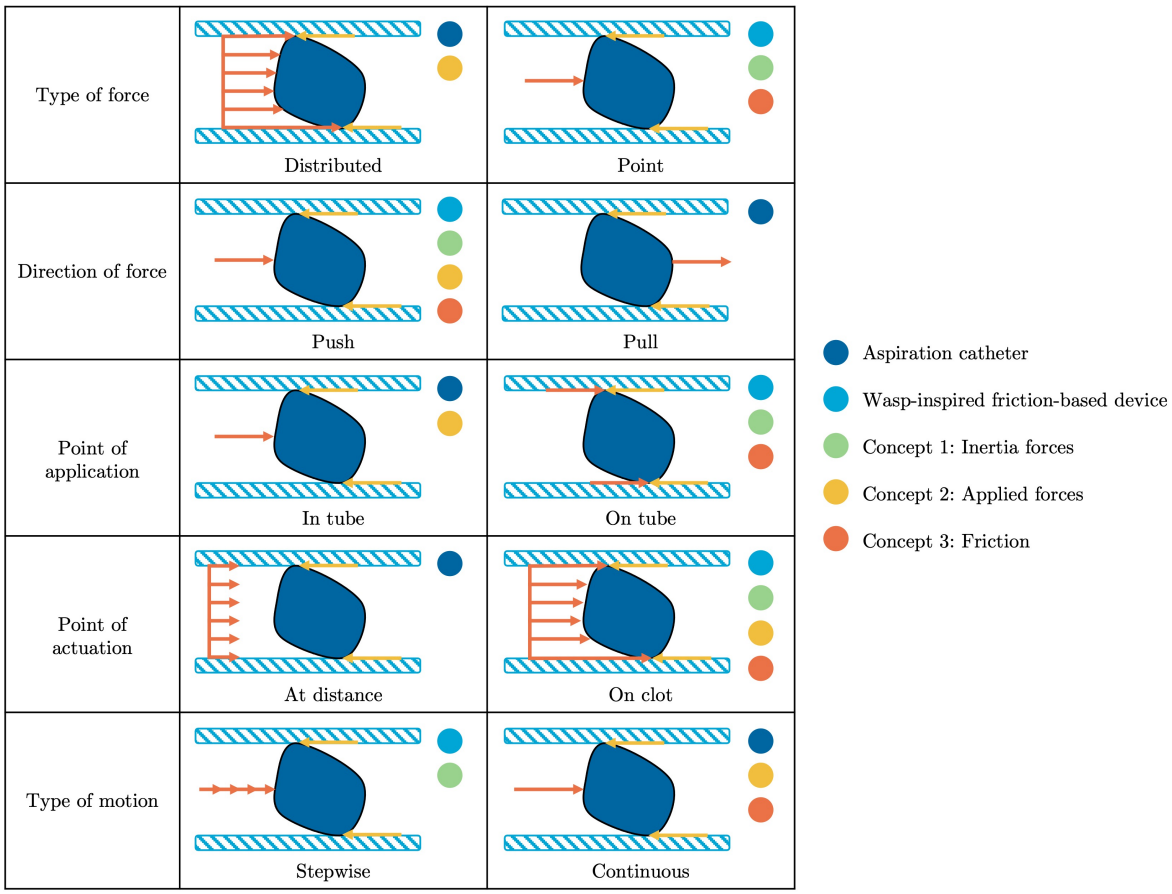

Figure 2: Dynamical perspective on tissue transportation. Each row represents a principle design variable. Orange lines resemble forces in the desired direction of transportation whilst the yellow lines resemble encountered friction forces. The coloured dots indicate specific combinations of the devices listed within the legend.

Besides this dynamic perspective, inspiration is gained from nature. Within the literature review by de Kater, an overview is given of transportation methods executed by animals [14]. According to this study, the transportation methods for solids as part of a single-phase system can be divided into three categories. Namely, transportation due to inertia forces, applied forces, or friction. The former describes the tendency of objects to remain unchanged in the magnitude and direction of their velocity. For example, whenever an object is accelerated and then released, the movement continues on the same trajectory. Applied forces relate to Newton's second law, in which an object moves in the direction of the net force. An example of this is a peristaltic movement, used to transport undigested food. Lastly, in the case of high friction between an object and a moving surface, the object is transported in the same direction. This phenomenon is implemented within the previously described wasp-inspired transportation device of Sakes et al. [27]. To ensure divergent ideas, three conceptual designs are selected, each implementing one of the three principles. Further, the requirement of a mechanism which enables continuous transportation of tissue appeared decisive (R1). In order words, the ability to transport multiple clots simultaneously, since time is critical within MIS.

2.3 Conceptual designs

2.3.1 Concept 1 - Transport due to inertia forces

The first idea makes use of **inertia forces** in order to transport the tissue through the shaft of the device. The working principle is visualised in Figure 3. The main body consists of both an inner and outer tube. Whenever the tissue is located within the device, the inner tube is accelerated and shifted in the distal direction. In the case that the acceleration is sufficiently high, the tissue remains in its position whilst the inner tube is shifted (1 and 3). Namely, the faster the inner tube is accelerated, the smaller the change in momentum of the tissue will be, increasing the chance of the tissue remaining in its position [9]. Due to inertia, also known as the resistance to change in motion, the tissue which is already at rest, stays at rest [32]. Subsequently, the inner tube is retracted at a low velocity, transporting the tissue accordingly (2 and 4). Both movements are repeated until the tissue is withdrawn from the body. The outer tube prevents contact between the moving tube and surrounding organs and vessels within the human body.

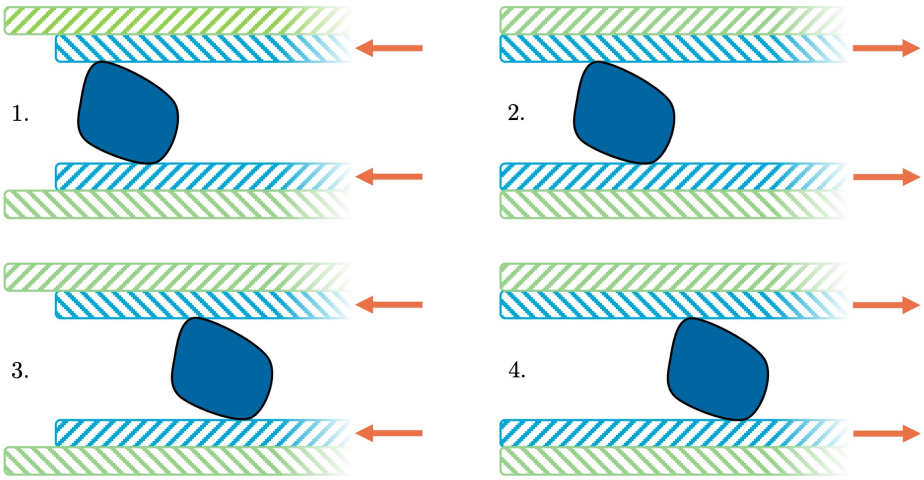

Figure 3: Visual representation of the first concept in which the green and blue striped parts resemble the outer and inner tube respectively and the blue shape the transported tissue. The orange lines indicate the direction in which the inner tube is shifted.

2.3.2 Concept 2 - Transport due to applied forces

The second idea makes use of **applied forces** actuated like a peristaltic movement in order to transport tissue along the shaft of the device. Two spirals are integrated in an identical manner along opposite sides of a tube. A silicone layer is stretched on the inside of the tube, accentuating the shape of the spirals. When taking the longitudinal cross-section of the tube in mind, both spirals create a wave-like line in which the peeks are aligned, narrowing the cross-sectional area of the tube within these sections. Tissue is positioned on the inside of the silicon layer, within one of the so-called valleys. When both spirals are rotated simultaneously, a continuous, peristaltic-like, movement is generated, pushing the tissue accordingly. The working principle is visualised in Figure 4 and Figure 5.

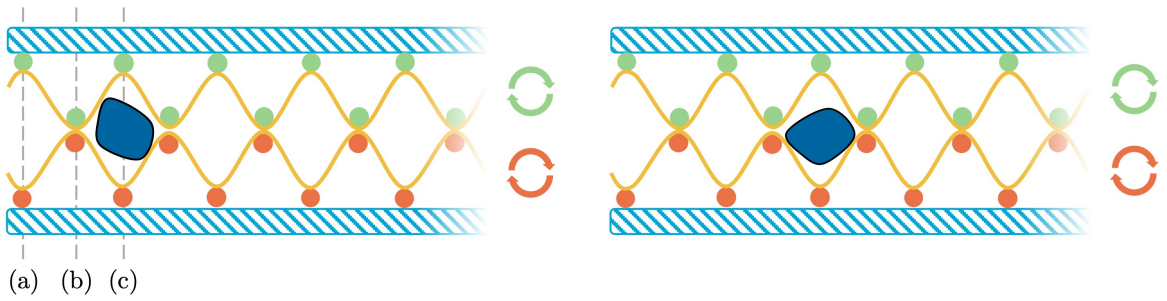

Figure 4: Longitudinal cross-sectional representation of the second concept. The green and orange dots represent the two rotating spirals which are both covered by a silicon layer, indicated by the yellow lines.

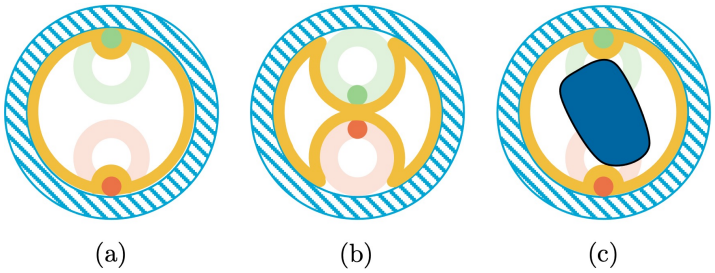

Figure 5: Radial cross-sectional representation of the second concept, at the indicated locations in Figure 4. The faded green and orange circles represent the path of the rotating spirals, in which the dot is the most proximal point, covered by the silicon layer shown in yellow.

2.3.3 Concept 3 - Friction based transport

Lastly, similar to the design of Sakes et al. [27], **friction** between the tissue and the body of the medical instrument is used as an advantage in order to create a transportation mechanism. Within this idea, a cylindrical conveyor belt is created, consistent with thread(s) wrapped along a tubular body. Due to friction between the thread(s) and tissue, the latter is transported whenever continuously rotating the thread(s) in the direction of removal. The working principle of this idea is visualised in Figure 6.

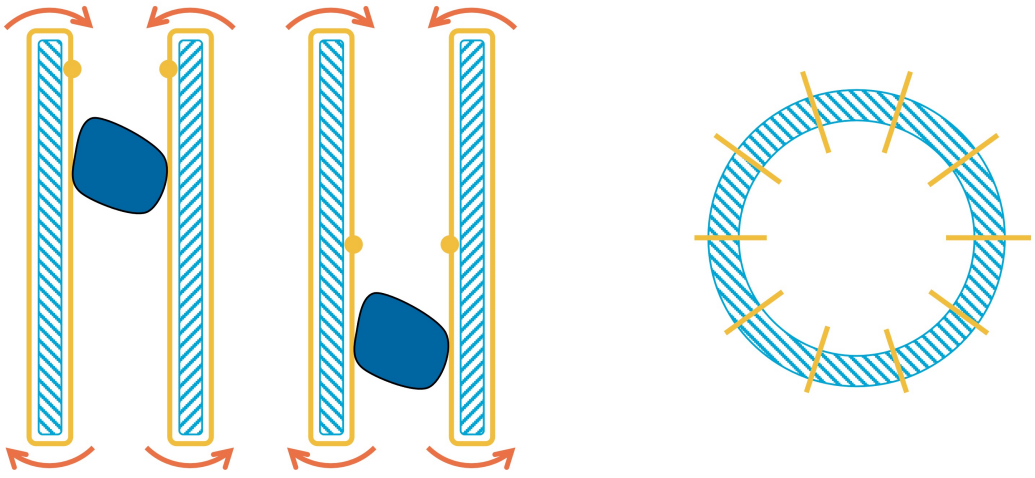

Figure 6: Longitudinal and radial cross-sectional visualisations of the tubular body of the third concept, in which the yellow lines represent the rotating thread(s). Within the left visual, the movement of the wire is shown by means of the yellow dot. The right image, resembling the top view of the tube, indicates the loops of thread(s), evenly distributed along the circular path of the tube.

2.4 Final conceptual design

In order to select the final conceptual design, all three ideas were tested by means of rapid prototyping. The goal is to get an estimation of the feasibility of each direction. Details concerning the created prototypes and executed experiments can be found within Subsection A.5.

Concerning the first concept, the feasibility is dependent on the required order of magnitude of the acceleration of the inner tube in order for the tissue to maintain its position. This is achieved whenever the net force is greater than the friction force in between the tissue and tube. The desired situation is mimicked by iteratively increasing the acceleration of a stainless steel tube consisting of a tissue phantom within a rail actuated by varying air pressures. However, since the tube did not maintain within the intended track at high velocities, the required acceleration is instead approached by measuring the pressure to blow the tissue phantom out of the tube, which resembles the maximum friction force between both. Based on these experiments, the required acceleration is estimated to be of the order of magnitude of $10^3 \frac{m}{s^2}$, see Subsection A.5 for additional elaboration and corresponding calculations. Subsequent deceleration should be executed slower to prevent the tissue from transporting in the opposite direction and ought to be realised within a limited distance. Even though this might be feasible from a dynamic and mechanical perspective, safety considerations make this idea less attractive since the instrument is employed within the human body. Note that the results of this experiment are case-specific and merely indicative.

The feasibility of the second idea is dependent on multiple aspects. Low friction between the silicons and tissue is required in order for the latter to move along the tube instead of getting damaged by the peristaltic movement. Also, the silicons on the inside of the tube require sufficient flexibility to accentuate the spiral and subsequently create a steep, wave-like, line. When the slope of the silicons is insufficient, scarce space is sacrificed and the surface area of the applied force on the tissue is reduced. However, both aspects appear to form a trade-off. The desired stretchability of the silicon layer is at the expense of a low friction coefficient between the silicons and tissue and creates a layer sensitive to disruptions. This is accessed by mimicking the situation within both a two- and three-dimensional setup, in which silicons and tissue phantoms with differing properties were utilized. Furthermore, since two spirals are required to generate the peristaltic motion, scalability is a challenge within this idea. Additionally, rotating a long thin spiral might be demanding from a mechanical perspective.

Concerning the third concept, rapid prototypes were made with stainless steel cables (two- dimensional) and PTFE-coated fishing threads (three-dimensional). It is concluded that sufficient friction between both threads and the tissue enables transportation of the latter. The required force for rotation is dependent on the friction between the threads and encapsulated tubular end. Increasing the number of loops of thread subsequently increases the experienced friction. The minimal bending radius of the applied threads is not approximated but is crucial to guarantee the scalability of the device in a cylindrical setup.

Based on these experiments, it is chosen to select the latter, friction-based, concept as the final conceptual design. Only the rapid prototypes of this concept seemed convincing concerning feasibility. Namely, for the first concept, the estimated required acceleration of the inner tube seems too high to safely employ within the human body repeatedly. Within the second concept, in addition to the challenge of scalability, the tissue phantom either adhered to the silicon layer or the layer insufficiently accentuated the spiral.

3 Final Design

3.1 Overview of design concept

A proof of principle prototype of the selected final conceptual design is developed in an iterative manner, completing multiple design cycles. Firstly, different functionalities of the concept were identified, resulting in smaller challenges. Subsequently, these challenges were addressed case-by-case, extending the functionality of the device step-wise. The exploded view of the final design and a selection of iterations are shown within Figure 7 and Figure 8 respectively. Within the former image, component names and corresponding functionalities are indicated. Additional drawings of the components can be found within Subsection A.12. Within the following sections, the design of the proof of principle prototype is elaborated based on the following functionalities.

- F1 - Enable tissue transportation through thread
- F2 - Enable thread connection
- F3 - Enable continuous thread rotation
- F4 - Enable smooth actuation
- F5 - Ensure thread positioning
- F6 - Ensure thread tension
- F7 - Enable manufacturability
- F8 - Ensure compatibility for Minimally Invasive Surgery

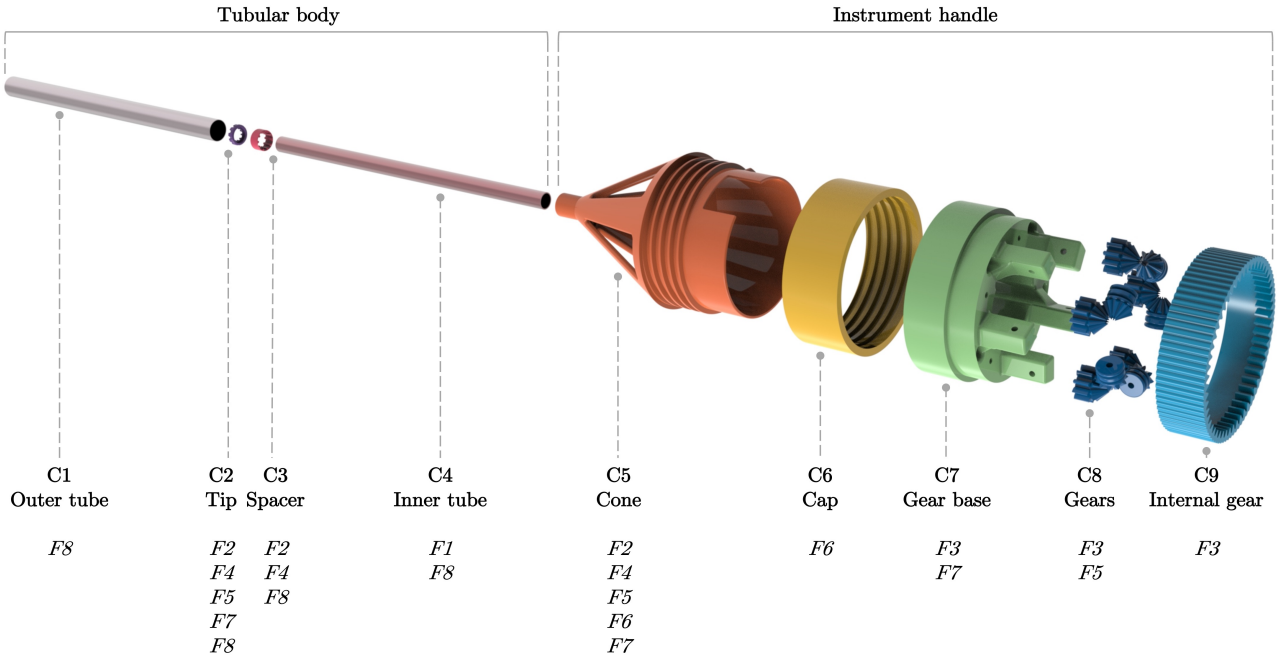

Figure 7: Exploded view of the proof of principle prototype components (C) and corresponding functionalities (F).

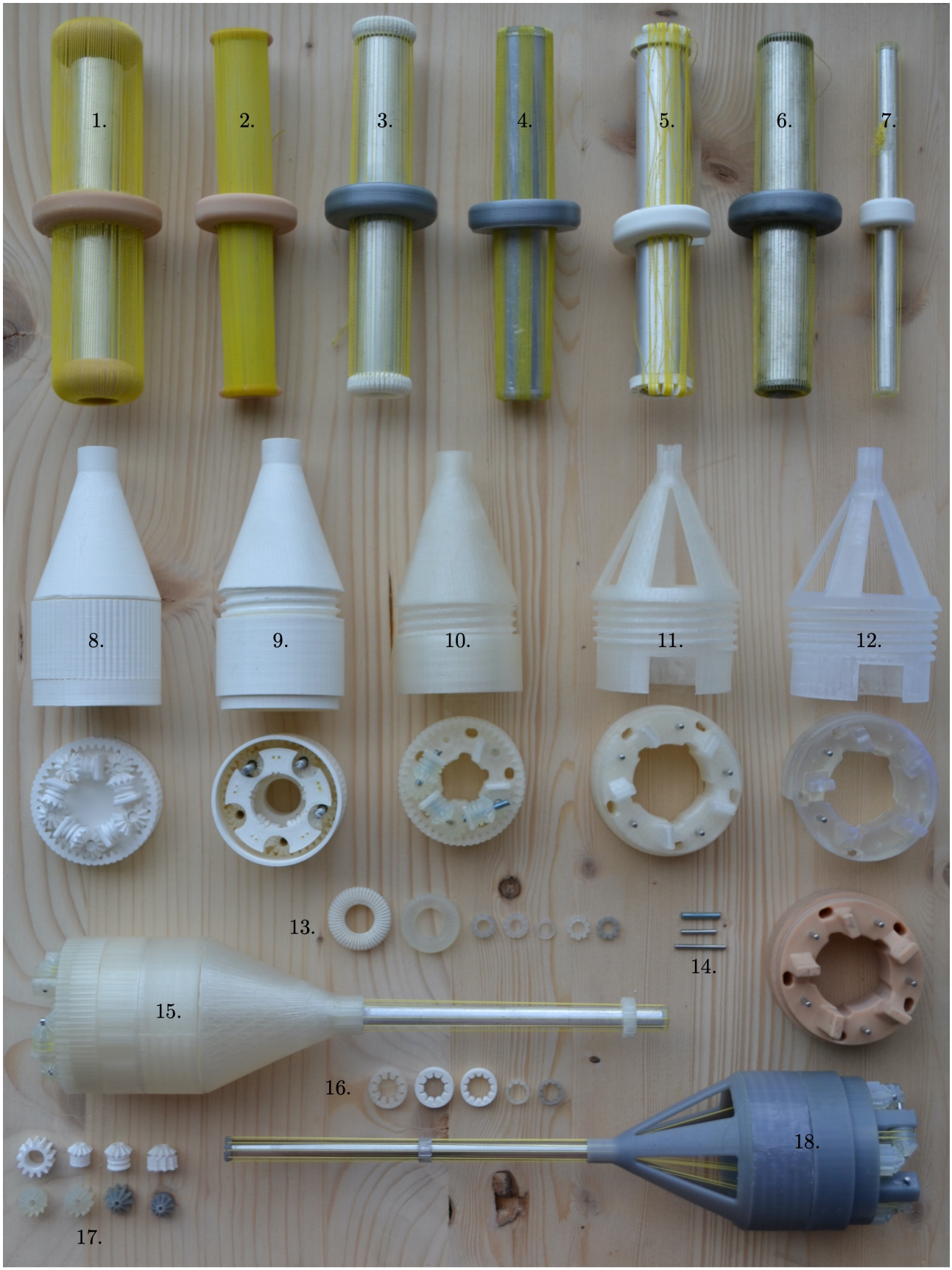

Figure 8: Selection of iterations (I) resulting in the final proof of principle prototype.

3.1.1 F1 - Enable tissue transport through thread

The designed mechanism enables tissue transportation by mimicking the working principle of a conveyor belt. Instead of a rotating planar surface, a thread is spanned along the inner tube (C4) of the instrument which is subsequently actuated to generate a comparable motion. Within the prior study exploring the feasibility of this design, this working principle is validated in a simplified manner. One thread is wrapped around a tube and is actuated through a repelling motion of an outer ring attached to the thread. By means of this setup, different thread compositions were validated for the suitability of tissue transportation (I1-I7). Here, the following trade-off occurs. Increasing the number of loops wrapped around the tube decreases gaps in between the concerning, further enclosing the transported tissue and maximising the potential points of contact between both, see Figure 9(a). The latter is beneficial since friction between the tissue and thread is desirable within the implemented working principle. However, increasing the number of loops of thread simultaneously increments the points of friction between the thread and instrument, requiring a larger force for actuation. As illustrated within Figure 9(b), within a device containing too few loops, the tissue is at risk of experiencing insufficient friction for transportation and of sticking to the tubular wall. Positioning several loops side by side in a group, of which multiple are distributed evenly along the circular path, did not appear to result in advantages whilst transporting tissue (I4). In this iterative manner, a suitable balance is approximated. The final design consists of one thread, wrapped around the tubular body a total of ten times as shown within Figure 9(c). The loops are evenly distributed resulting in a spacing of approximately 1.4 millimetres measured along the inner circular path of the tube. The advantage of implementing one thread is that fewer adhesion points are required when compared to multiple threads, and is enabled since both ends of the thread meet along the same trajectory. The thread within the final prototype is made from stainless steel and consists of nineteen intertwined smaller threads (1x19), resulting in a total diameter of point two millimetres. This dimension is selected in a trade-off between minimizing size whilst maintaining sufficient mechanical properties. The thread (Engelmann Vom Hofe Group [7]) has a minimum breaking load of 38 Newton. Throughout the rapid prototyping phase, point two millimetre diameter, pre-stretched, Dyneema braided, PTFE-coated fishing threads were additionally used (I1-I7, I15 and I18) [30].

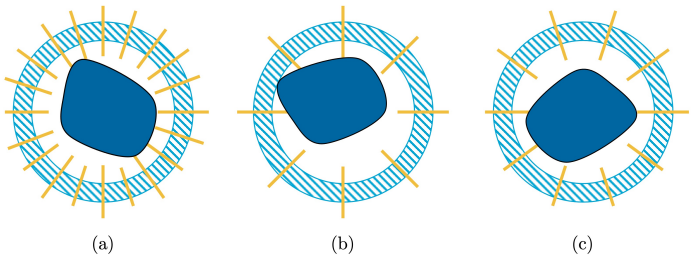

Figure 9: The cross-sectional area of the inner tube in which the yellow lines represent loops of thread and the middle blue shape the tissue.

3.1.2 F2 - Enable thread connection

After wrapping the thread, both ends ought to be attached to each other. It is desirable for the connection not to form a bulb since this would both prohibit the rotation of the thread through the device and block the inside of the inner tube. Suitable connection methods have been explored, such as glueing, soldering and knotting, and are dependent on the thread material. Due to the oxide layer on the stainless steel thread implemented within the final design, both glueing and soldering are challenging. This layer prevents both forms of fasteners from sticking to the surface. Sanding the exterior is at risk of disintegrating the thread composition, which would eventually result in snapping of the concerning. Subsequently, the option of knotting remained. Since it is desirable for the thread to be as thin as possible, a flat knot as shown in Figure 10 is implemented to connect both ends of the thread. Afterwards, the excess thread is trimmed, which should not be too short, to hinder the untying of the knot. For additional assurance, a small amount of superglue is added within the small gaps of the knot. Whilst the thread will rotate during operation, several components are adjusted to prevent interference with the knot (C2, C3 and C5) and will be further elaborated later on.

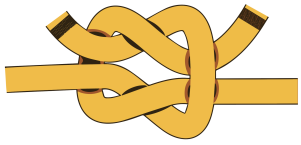

Figure 10: Flat knot implemented to tie both ends of thread.

3.1.3 F3 - Enable continuous thread rotation

Within the final design, the wrapped thread is rotated in order to mimic the motion of a conveyor belt. Within the exploitative phase, this movement was actuated by repelling an outer ring clamping the thread (I1-I7). However, as stated within R1, continuous rotation is required since tissue removal in an ongoing stream reduces operation duration. Next to this, since the mechanism is based on the working principle of friction, moving the thread in opposite direction would subsequently transport the tissue to its former position unless the magnitude of friction whilst repelling is sufficiently reduced. Actuation of the desired rotating motion is achieved by clamping each loop of thread along a revolving axis. This clamping will be addressed within the subsequent section. Due to the dimensional restrictions of the tubular body of the device (R5), the actuation containing the revolving axis is incorporated within the handle of the instrument.

As previously substantiated, the tubular body in which the tissue is transported contains a total of ten loops. Therefore, one single point of actuation is not feasible, since this prevents the tissue from leaving the device, see Figure 11(a). Subsequently, a minimum of two actuation points are necessary, resulting in two sets of five loops of thread actuated simultaneously. This setup constrains the loops to merge at two points, in an identical orientation, in order to facilitate the movement by rotation along one single axis, see Figure 11(b). However, this counters the original circular distributed positioning. Whilst it might be favourable to actuate all loops separately, this simultaneously demands more space to position all ten rotating mechanisms. Within the final design, a compromise is made between both elements. Namely, enabling the loops to remain in their circular positioning and limiting the required volume of the actuation mechanism. Two loops are rotated through the same gear. This results in a total of five points of actuation, distributed equally along a circular path as shown in Figure 11(c).

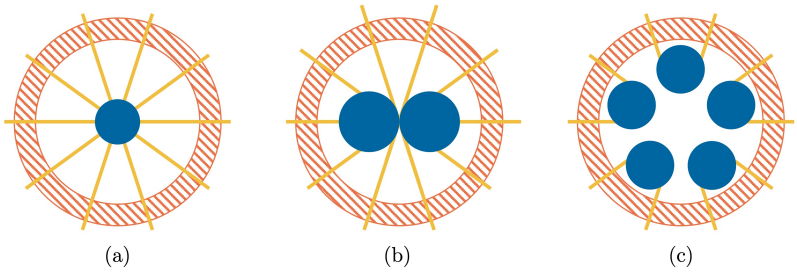

Figure 11: The cross-sectional area of the handle in which the yellow lines represent thread loops and the blue dots potential points of actuation.

R9 argues the importance of the ability to operate the medical instrument by one user only. Assuming that one hand is used to hold the device, the other hand remains for actuation. In other words, the five points of actuation ought to all rotate at once through one action. Additionally, since the actuation mechanism is incorporated within the handle of the device, it is desirable to work all mechanics away neatly and keep the dimensions manageable. With this in mind, the gearbox as shown in Figure 12 was designed. Since all five actuation points have a differently orientated axis of rotation, bevel gears (C8) are implemented. These gears transmit motion between perpendicular shafts, subsequently shifting all axis of rotation parallel to one another. One of each set of bevel gears is merged to the axis clamping the thread, whilst the other is joined to a spur gear. The latter enables satisfying the before-mentioned requirement of actuating the device within one movement. Namely, the rotation of the implemented internal gear (C9) results in the rotation of all other gears, subsequently rotating all loops of thread simultaneously. All gears are attached to and the internal gear is supported by the gear base (C7). The axes are secured whilst the gears rotate freely.

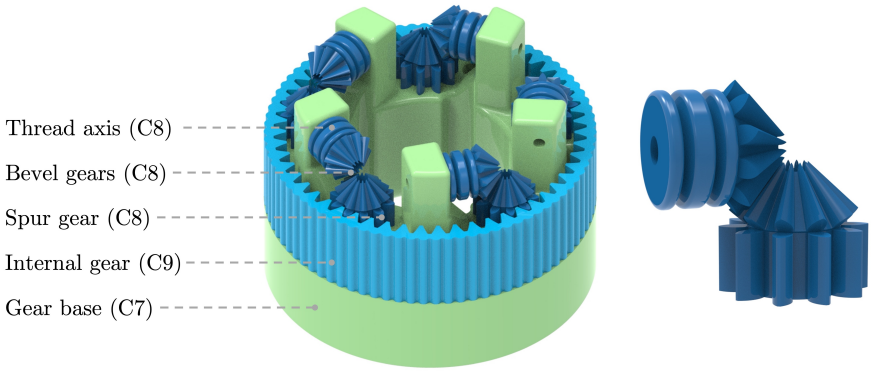

Figure 12: Gearbox with indicated components.

Several iterations were required to accomplish the design of the shown gearbox, with differing shapes, sizes, and materials. All elements, excluding the axes, were made through additive manufacturing, also known as 3D printing. Two types of printers were accessible during the design phase, the Ultimaker S3 and Formlabs 3+ SLA printer. More information regarding these printers can be found within Subsection A.10. The former printer was used in order to verify the working principle of the actuation mechanism (I8-I10). Screw threads served as axes for quick assembling. Even though feasibility was demonstrated, the gearbox seemed too fragile, resulting in breaking elements. The vertical holders of the gear base used to support the horizontal axes appeared to be critical. Enlarging the gear base from a diameter of five to six centimetres enabled adding body to these holders (I11). An even larger diameter is undesirable to keep the size of the handle of the device appropriately. In combination with fillets and by printing the element with the resin called 'Tough', the gear base meets the required strength requirements (I18). Other resins, for example, 'Clear' and 'Model', might satisfy this additionally but appeared to be too brittle, failing during assembly (I12). Namely, within the final design, two-millimetre axes are forced into the smaller pre-printed holes within the gear base after which superglue is added. Complete fastening is essential since due to the high forces during actuation, the axes are otherwise tended to shift out of position. I14 illustrates the evolution of the axes, in which the bottom axis with a diameter and length of two and fifteen millimetres respectively is implemented within the final design. Especially for the vertical axis, this additional length is advantageous. Lastly, the gears are printed from the resin 'Durable', experiencing the least friction between one another and enabling the thread to slightly cut into the material, enhancing the clamping of the concerning. I17 displays a selection of gear iterations, in which materials, dimensions and design are optimised. To ease the positioning of the internal gear, the number of teeth of the joined bevel and spur gear are identical and perfectly aligned.

Lastly, a redesign was made of the internal gear, enabling motorized actuation. This has the advantage of reducing the operational tasks of the user, results in a more stabilized rotational velocity and potentially enables higher rates when compared to manual actuation. As shown in Figure 13, the internal gear is extended in height and closed at the end. The hole in the middle contains a shape lock for the axis of the motor additionally shown. The implementation of this motor will be further elaborated within Subsection 4.3.

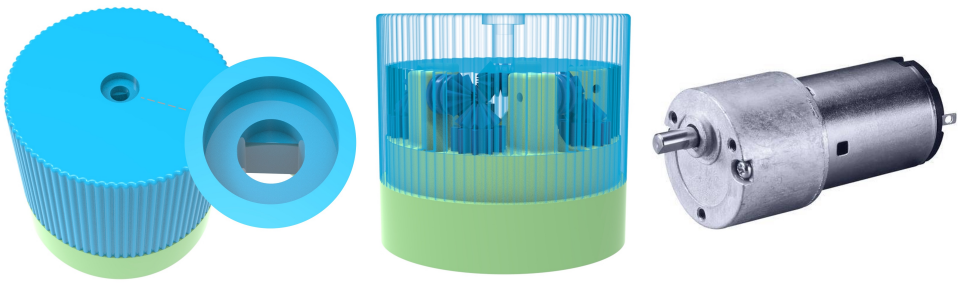

Figure 13: Gearbox with enclosed internal gear, containing a shape lock for the axis of the motor shown on the right [6], used for automated actuation.

3.1.4 F4 - Enable smooth actuation

Within the designed mechanism, the physical phenomenon of friction is used as an advantage in order to transport tissue. However, even though a high magnitude of friction is desired between the tissue and thread (point 5), there are also regions in which friction is experienced as an obstacle. Figure 14 indicates parts in which either one of the situations applies.

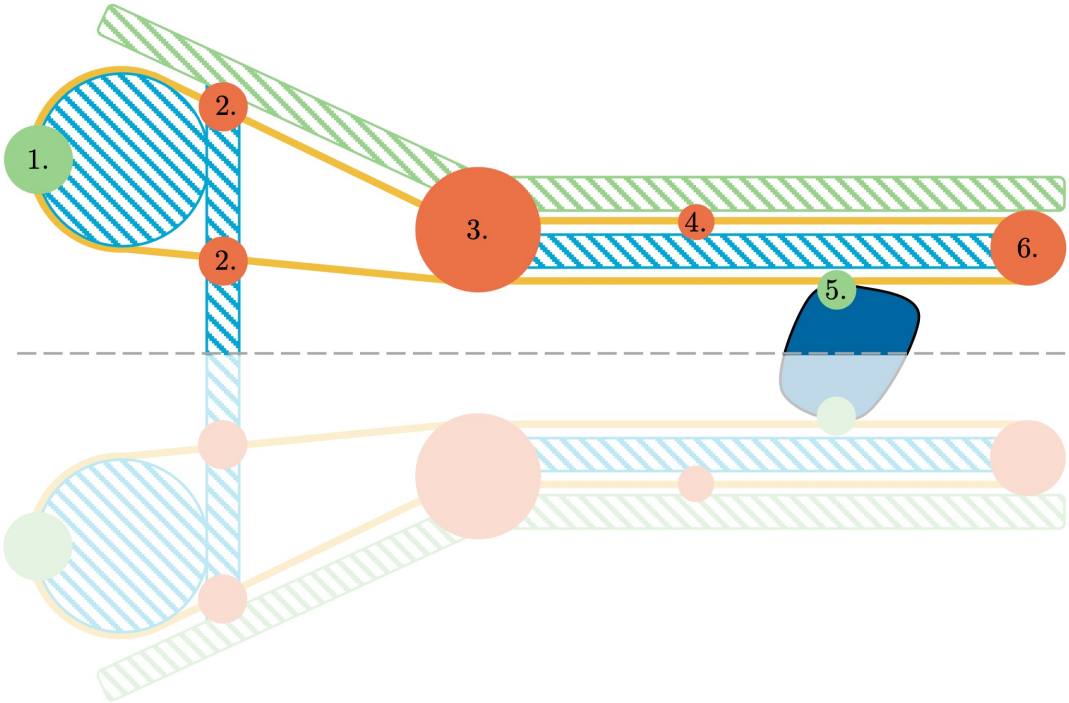

Figure 14: Schematic overview of the device in which green and orange dots resemble areas in which friction is either desired or not, respectively.

Firstly, high friction between the thread and the body of the device complicates the rotation of the former, resulting in a higher force that is required to actuate the mechanism (point 4). To minimise this hindrance, the thread is spanned with an offset of approximately point six millimetres on all sides of the tubular walls, as illustrated within Figure 21. However, at the tip of the device (point 6), the thread is required to be guided, automatically resulting in a point of contact. Since this is inevitable, the tip shown in Figure 15 is attached to the distal end of the device, minimizing the experienced drawback and simultaneously forming several advantages (C2). Firstly, due to the increased outer and decreased inner diameter of the tip with respect to the inner tube, the previously mentioned offset between the thread and tubular walls is facilitated. Next to this, the curvature along which the thread is spanned is increased to a radius of approximately one millimetre due to this add-on, preventing additional friction due to kinking of the thread. Lastly, this tip guides the different loops of the thread within grooves, ensuring the positioning of the concerning throughout usage. This will be further elaborated within Section 3.1.5. Besides the design of this add-on, the material influences the experienced friction additionally, which is tested thoroughly (I13). Even though the resin 'Durable' reduces the amount of friction the most, other mechanical properties enforce the implementation of the resin 'Tough'. Namely, through the rotation of the thread, a cutting motion arises, which the tip should be able to withstand. Within I4 and I6 the implementation of lubricating spray and graphite powder with the aim to reduce friction is tested. The latter seemed most efficient. However, the inability to only experience the influence of the powder locally disapproves utilisation. The tip is snapped on the inner tube due to the raised edge, as shown in Figure 15.

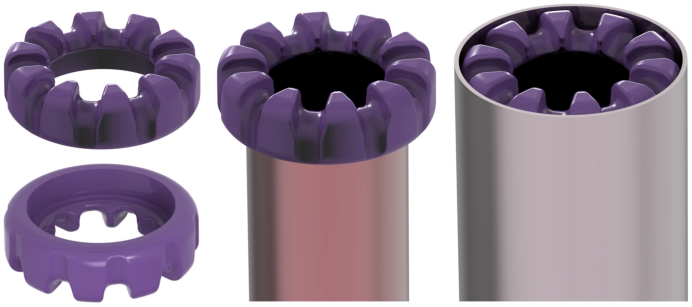

Figure 15: Design of the tip component.

The previously mentioned areas are all based within the tubular section of the device, inserted within the human body. Within the handle attached to it, the circular area of the thread is enlarged, both in order for the tissue to be removed from the device and to generate space for the actuation mechanism. Again, the thread is spanned with an offset with respect to the handle body, to avoid undesired friction. The same applies to point 2, in which the thread both enters and exits the gear base. However, within point 3, all loops are redirected, resulting in a contact point between the thread and cone (C5). Since this is inevitable, hindrance is minimised by introducing a gentle slope ($\mp$ 150°) on which the thread is guided. Lastly, within section 1, resembling the axis rotating the thread, friction is used as an advantage once more. As already mentioned, five axes are distributed along a circular path each guiding two loops of thread. As shown within Figure 16, the rotating axis is merged into one of the bevel gears. The axis contains two slots, both narrowing towards the centre of the axis, also referred to as V-grooves. Due to this decline in width, the thread is clamped within. Whenever the axis rotates, the thread is pulled in the same direction. Note that it is not suitable to completely fasten the thread to the axis since a continuous rotation of the former is demanded. The thread is passed through whilst the axis rotates. In order for the designed approach to succeed, sufficient friction is required to prevent slipping, which would result in a stationary thread whilst the gears rotate. Therefore, lube along the thread should be avoided, even though it might be beneficial for other regions, such as between the gears, within the cone and on the tip. Contamination of the thread is of too high risk. As mentioned in the previous section, the chosen material of the gears enables the thread to slightly cut into the material, enhancing the clamping of the latter.

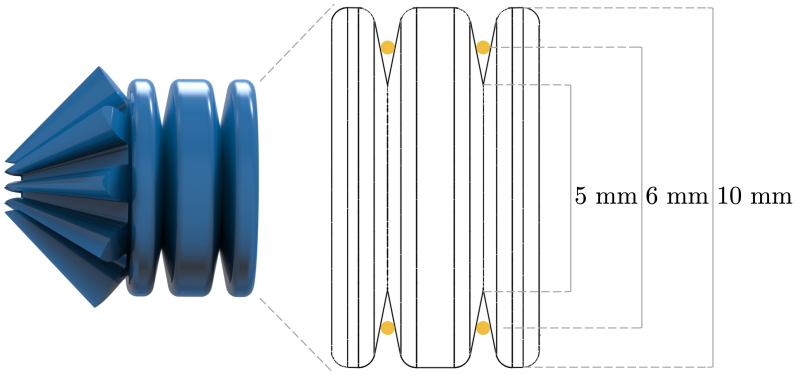

Figure 16: Rotating axis clamping two loops of thread, as indicated by means of the yellow dots.

Lastly, it should be mentioned that specific regions of friction within the device are dependent on the amount of tension of the thread. Namely, whenever the thread is completely stretched, the contact area between the thread and both the tip and rotating axes is increased. Since it is not beneficial for the former but is desired for the latter, a trade-off remains.

3.1.5 F5 - Ensure thread positioning

As clarified previously, the loops of wrapped thread are distributed evenly along a circular path in order to span a tubular body. To maintain its functionality, the positioning of these loops should be secured throughout the operation. As elaborated within Section 3.1.4, contact between the thread and device is mostly undesirable. Therefore, positioning of the thread is ensured at the previously discussed inevitable points of contact, C2, C5 and C8. Firstly, the tip shown in Figure 15 contains ten sheave grooves. An optimum exists in the amount of clearance between the thread and sheave. Whenever the groove diameter is too small or too large, either pinching or flattening of the thread will occur, increasing undesired friction [17]. However, since both ends of the thread are connected by means of a flat knot, sufficient clearance is required to enable this fastener to pass. Therefore, the sheave diameter is maximised. It is assumed that the flattening of the thread has negligible influence on the experienced friction due to the small diameter of point two millimetres of the concerning.

Secondly, the cone, in which the thread loops are redirected, forms an inevitable point of contact. This drawback is subsequently used as an advantage by making use of the opportunity to ensure the proper positioning of each loop. Figure 17 shows this area in more detail. As visualised, each loop of thread has its own aperture at its disposal. Not only individual loops but also in- and outgoing loops are separated. This simultaneously makes assembling easier as the thread is less likely to intertwine. Again, the size of the holes is sufficient to enable the knot to translate through the cone. As additionally shown within Figure 17, the inner tube perfectly fits within the distal end of the cone and is supported on the region separating the in- and out-going loops. Subsequently, the outer tube (C1) is slid over the distal end. Further translation downwards is prohibited due to the increase in diameter of the cone. Within among other iterations I9-I12, these functionalities are optimised. The capacities of additive manufacturing are utilised, by integrating this guidance within the handle and by pushing the boundaries of minimum wall thickness and detailing. This simultaneously contributes to the desire of minimising the number of components (W12). Lastly, each loop is separated once more within the V-grooves of the rotating axes as previously shown within Figure 16.

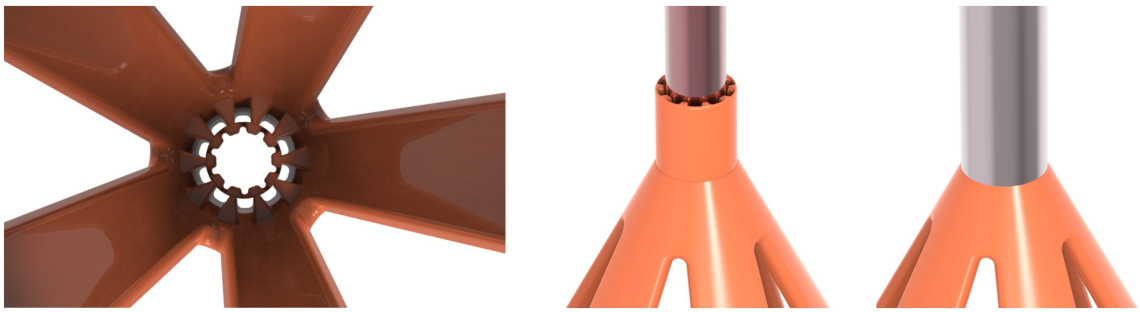

Figure 17: The distal end of the cone, viewed from the in- and outside, with and without the outer tube.

3.1.6 F6 - Ensure thread tension

Within the designed mechanism, sufficient tension of the thread is required for multiple reasons, concerning the working principle of the device, maintaining the position of the loops of thread, and ensuring long-term functioning. First of all, the tissue ought to contact the thread in order for the transport mechanism based on the principle of friction to work. Besides that, contact between the tissue and the tubular wall is undesirable since this would result in friction forces enhancing the tissue to remain in a static position. By tensioning the wrapped thread, a tubular body is spanned with an offset with respect to both the inner and outer tube, through which the desired and undesired friction forces are optimised. Secondly, for the thread to form the before-mentioned tubular body, sufficient tension is required to constrain all loops within a specific position, evenly distributed along a circular path. Slack within the thread would result in overlapping, potentially tangled, loops and complicates guaranteeing the intended distribution. Lastly, introducing the ability to tension the thread contributes to the wish to ensure the long-term operability of the device (W10). Namely, it is likely for the stainless steel wire to deform gradually due to creep, a consequence of strain and temperature fluctuations. This results in a decrease in tension over time, potentially making the instrument dysfunctional. The designed mechanism anticipates this occurrence, facilitating the manually straining of the thread.

The implemented thread is wrapped around a tube, resulting in ten loops consistent of one thread. Since all loops are interconnected, tensioning one of the concerning, simultaneously affects the other. To ensure an even force distribution, preventing failure due to local peak forces, it is chosen to tension all loops at once. Within the cone, a screw thread is implemented. C6 resembles the accompanying cap. During assembly, this component is screwed on the handle body in its extremity. Afterwards, it can be twisted in the reverse direction, increasing the distance between the tubular body and gears, and subsequently straining the thread. The screw thread enables a tension distance of twenty millimetres. The concerning components and configurations are shown within Figure 18. Additionally, five holes within the cone can be seen which are extruded in order to enable the removal of the transported tissue from the handle. The exact operation of tissue extraction falls outside the scope of this research.

Figure 18: Tensioning mechanism consisting of a screw thread within the cone and accompanying cap. Two configurations are included.

The described design is firstly implemented within iteration 9 and optimised in a step-wise manner. Several advantages were decisive in favour of the implemented mechanism. Firstly, since the mechanism is already present within the handle in an inactive state during the assembly of the thread, it is possible to manually tension the concerning whilst wrapping. This is beneficial for multiple reasons and will be further elaborated within Section 3.1.7. An additional advantage is the hollow shape of the mechanism, which enables the thread to rotate freely on the inside and maintains an unobstructed path for the transported tissue. Further, as mentioned previously, a trade-off remains concerning the optimal thread tension. Increasing this tension enhances the clamping of the thread and improves the spanned tubular body. However, this additionally increases the experienced friction at the tip of the device, necessitating a higher actuation force. Since the implemented screw affects this variable gradually, this optimum can be approached. Note that the minimum breaking load of the thread, 38 Newton, should not be exceeded.

3.1.7 F7 - Ensure manufacturability

Within Subsection A.6, a few snapshots of the assembly process of the device are displayed. In order to enable manually assembling the designed device, several aspects have been taken into consideration. Firstly, even though the implemented screw tread enables tensioning the thread afterwards, it is beneficial to already tension the thread manually whilst wrapping. This prevents the thread to slip out of the associated grooves and makes it less likely for the thread to get tangled up. In order to achieve this, all parts of the device should be fixed with respect to each other during assembly, prohibiting a design in which parts are attached to each other after insertion of the thread. This requirement was among other things decisive in the design of the tensioning mechanism, in which the cap is present during assembly in an untwisted state. Also, due to the design of the cone, the inner tube can be clamped within the concerning (Figure 17).

Intuitively, it might feel logical to position the gearbox towards the inside of the handle, as is the case within I8 and I9. This simultaneously protects the gears and does not require a hole in the middle of the gear base, subsequently sealing the device. However, from a manufacturability point of view, this complicates assembling the device. Namely, access to the gears is limited whilst this is desired during the wrapping of the thread and in case of troubleshooting. Therefore, it is chosen to flip the direction of the gearbox, resulting in the gears facing outwards (I10). Sealing of the gearbox can still be achieved by external housing, enclosing the design of the internal gear. Simultaneously, this has the advantage that it is easier to connect the gear base to the cone of the device. The bottom of the gear base consists of more free space for anchoring as the opposite side contains the rotating gears.

Further, rotation of parts with respect to each other should be prevented, both during and after assembly. Namely, this would result in the twisting of the thread, prohibiting its functionality. In order to ensure this, a shape lock is implemented in between the gearbox base and cone (I11), see Figure 19. The bottom of the cone is extended with a partial cutout. An identically shaped slot is made within the gearbox base, enabling both parts to align. Vertical displacement with respect to each other is still possible, which is required in order to tension the thread after assembling. Within the final instrument, these parts are thus only connected by means of the thread.

Figure 19: Shape lock between the cone and gear base.

As almost all components are manufactured through additive manufacturing, the opportunity emerges of combining different elements, reducing the number of components, as desired within W12. This is clearly the case for the cone, gear base and gears. The cone includes the tensioning mechanism, form lock, gaps for tissue extrusion, and guiding apertures for all loops of thread. The latter simultaneously make assembling easier as the path of each loop is predetermined and obliged. The design of the gear base is optimised to enable the passing of the thread, provide sufficient stiffness for the forces on the connected gears, and attachment to the cone, resulting in a unique element. Lastly, both bevel gears are merged with either a spur gear or the revolving axis.

3.1.8 F8 - Ensure compatibility for Minimally Invasive Surgery

Compatibility for MIS relates to multiple aspects of the device such as dimensions, material selection, and design decisions considering safety. All elements can be decisive in whether the instrument can be utilized for tissue removal within the human body and inserted through a small incision.

The designed mechanism consists of a continuously rotating thread, serving as a tubular conveyor belt. Even though this rotation is necessary on the inside of the device, it is undesirable for the same motion to capture surrounding, healthy, tissue on the outside of the device (R7). Therefore, a protective tube is positioned around the mechanism, referred to as the outer tube (C1). This simultaneously protects the mechanism and reduces experienced friction between the thread and surroundings, since the outer tube is positioned with an offset around the concerning. C3, the spacer, separates both the inner and outer tube. Holes within this component enable the thread and the corresponding knot to translate freely, see Figure 20. Besides the spacer, the outer tube is additionally aligned through the cone, as previously shown within Figure 17. Further, the tip add-on, previously shown in Figure 15, seals the clearance between both tubes. Additionally, the loops of thread are slightly countersunk within the tip, securing surrounding tissue.

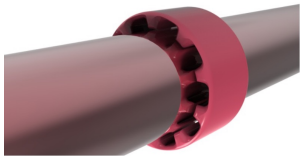

Figure 20: Spacer, aligning the outer tube around the inner tube, without obstructing the thread.

Secondly, implemented materials should not endanger the patient's health (R8), are required to be resistant to fluids encountered within the body, and ought to fulfil mechanical demands. The designed device consists of two stainless steel tubes, a stainless steel wire, and multiple printed components through additive manufacturing made from different types of bio-compatible resins [1], satisfying this requirement. All components are resistant to chemical agents, potentially used for sterilization of the device (W11).

Lastly, the dimensions of the device are decisive in order to guarantee suitability for MIS. The devices illustrated by I15 and I18, show the iteration considering this design improvement. As stated within R5, the instrument should have a maximum outer and minimum inner diameter of ten and five millimetres respectively. Even though even smaller outer dimensions are desirable to reduce the required incision size even more, it is chosen to prioritise the ease of manufacturing, precisely satisfying the stated requirement. The distal end of the tubular body is schematically visualised in Figure 21, in which corresponding components and dimensions are annotated. The wall thickness of the outer tube is minimized based on the availability of Salomon's metals [28]. Subsequently, since the tread should not come in contact with both tubes to reduce friction, the dimensions of the inner tube are determined in order to fairly distribute the available space whilst ensuring an inner diameter of the spanned thread of five millimetres. Also, the wall thickness of the inner tube is doubled when compared to the outer tube to facilitate the attachment of the tip component. To conclude, the device requires a minimal incision length of ten millimetres for insertion and enables the removal of tissue with a maximum diameter of five millimetres.

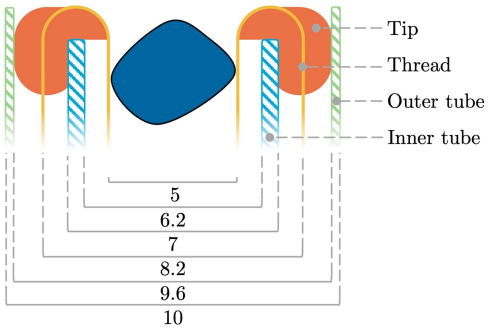

Figure 21: Schematic representation of the distal end of the tubular body including dimensions.

3.2 Final prototype

Multiple photographs of the final proof of principle prototype, implementing all previously described elements, are shown in Figure 22. Additionally, a selection of usage steps is visualised within Figure 23. Furthermore, an operative video of the medical instrument can be seen here.

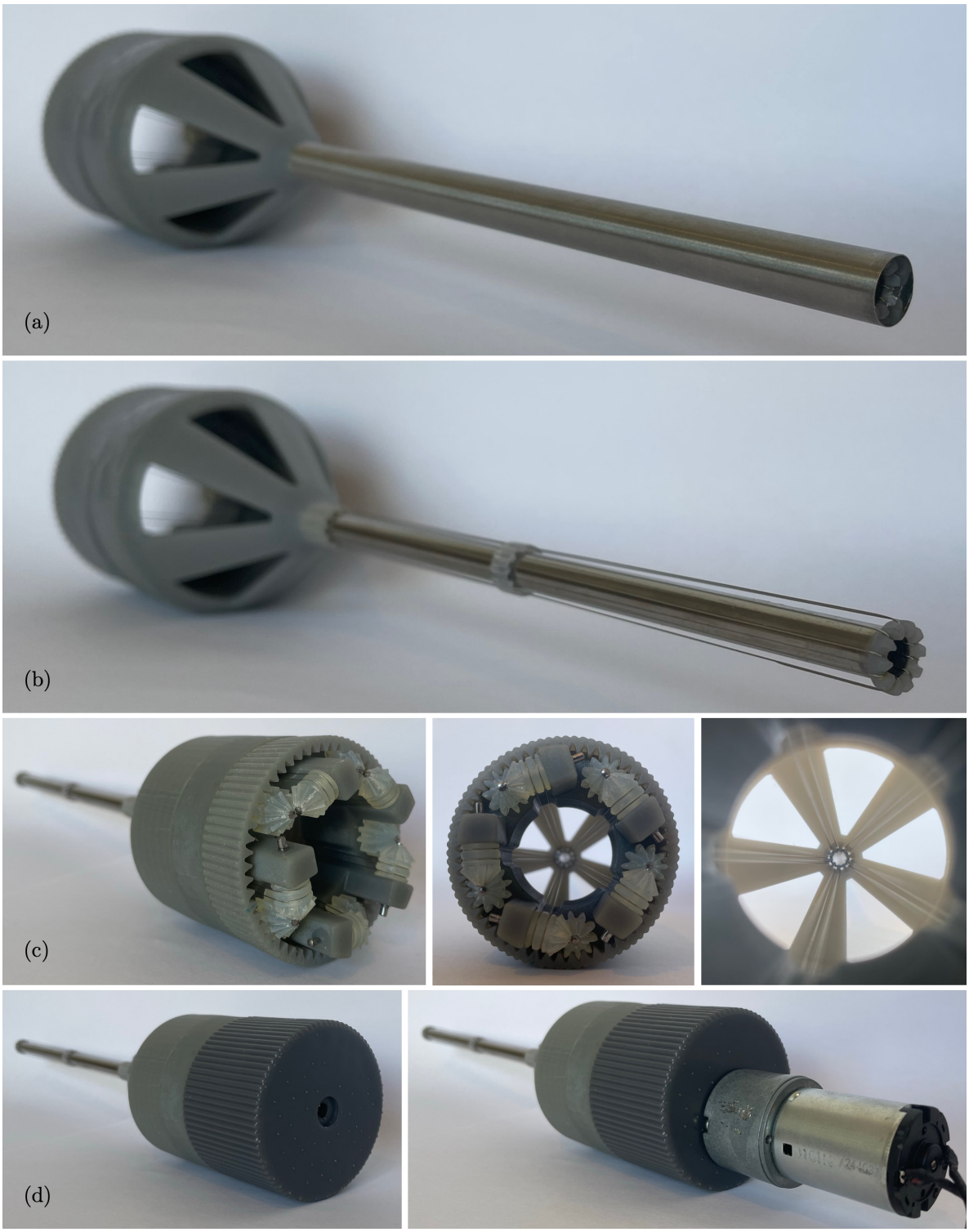

Figure 22: Photographs of the final proof of principle prototype. (a) Complete device, (b) Device excluding the outer tube, (c) Device configuration for manual actuation, and (d) Device configuration for motorized actuation.

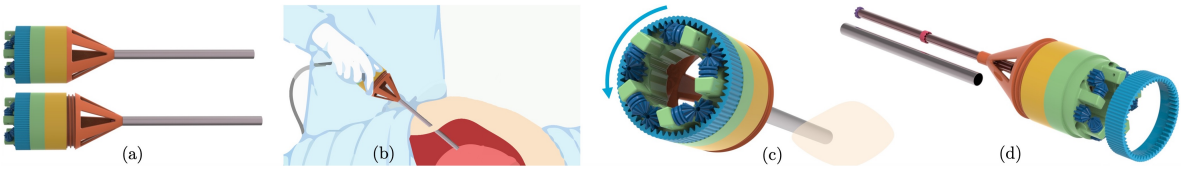

Figure 23: Selection of usage steps: (a) Tensioning of thread, (b) Instrument insertion in human body through 10 mm diameter incision, (c) Tissue removal through manual or motorized rotation of the internal gear, and (d) Potential device disassembly for complete or partial re-usage.

4 Experimental validation

4.1 Goal

The main goal of this research is stated as follows; design a continuous tissue transportation mechanism compatible for MIS in which the transportation velocity is independent of tissue elasticity within the young's modulus range of 1-110 kPa. The last element of the objective relates to the performance of the device and is tested through experimental validation of the proof of principle prototype. Three experimental goals were tested, indicating the influence of the rotational velocity of the internal gear, the angle in which the device is operated, and the sample shape on the transportation velocity of tissue within the stated elasticity span.

4.2 Experiment variables

4.2.1 Independent variables

Tissue elasticity
The transportation mechanism ought to be suitable for tissues within the elasticity range of 1-110 kPa. This represents a large range of tissues and organs which can be encountered during MIS. To mimic the mechanical characteristics of this span, tissue phantoms were made consistent with gelatine and water. The implemented samples have a gelatine weight percentage (wt%) of 3, 9, and 12, representing a tissue elasticity of approximately 1-10, 55, and 100-110 kPa respectively [13]. Since the referenced study does not explicitly include data concerning the two extremities, the corresponding young's moduli are an estimation. More information regarding these tissue phantoms can be found within Subsection A.7.

Rotation velocity
The developed mechanism is actuated by rotation of the internal gear. Increasing the velocity of this motion subsequently increments the translation rate of the thread and therefore the tissue transportation velocity. However, it might be hypothesised that excessive rotation velocities of the thread potentially result in slipping between the concerning and tissue. Therefore, this aspect is varied within the experiments to indicate its influence. To guarantee consistent rotation of the proof of principle prototype, actuation is facilitated through an electromotor. Experiments are executed with three different actuation velocities, based on the capabilities of the before-mentioned motor, resulting in a voltage of 8.5, 11, and 13.5. The lower extremity is the minimum required voltage in order to set the internal gear in motion. The subsequent rotational velocity is expressed in rotations per minute (RPM).

Instrument orientation
Within MIS, the tubular body of the device is advanced through the human body until correctly positioned for removal. In order to access these target locations, the orientation of the instrument is varied gradually, which impacts the effect of gravity. For example, in a more upright position of the tubular body with the tip pointed downwards, gravity results in a force on the tissue opposite to the direction of removal. Whenever this force is higher than the friction between the thread and tissue, removal is obstructed. Within the experimental setup, the operation of the proof of principle prototype is tested horizontally and by pointing the tip of the instrument downwards at an angle of twenty degrees.

Tissue phantom shape

Transportation within the designed mechanism is enabled through friction between the thread and tissue. These loops of thread are evenly distributed along a circular path, subsequently spanning a tubular body. Whenever this body is completely filled with tissue, all threads contribute to the translation of the latter, maximising the positively experienced friction between both. Whenever this is not the case, fewer threads affect this motion. To map this influence, tests are executed with both cylindrical and half-cylindrical tissue phantoms. The diameter and height of each sample are five and fifteen millimetres respectively.

4.2.2 Dependent variables

Transportation velocity

All previously mentioned independent variables potentially influence the transportation velocity of the tissue phantoms. Minimising the required time for removal is desired within MIS, reducing anaesthesia time and operational costs [27]. Therefore, it is desired to maximise this variable, matching or exceeding flow rates of currently used devices. The transportation velocity is expressed in $[\frac{mm}{s}]$, calculated by dividing the travelled distance of the tissue phantom within the tubular body by the required time. Additionally, to enable comparison to commercially available devices, an estimation is made of the corresponding transportation rate in $[\frac{g}{min}]$, calculated by dividing the average tissue phantom weight by the average time required for the concerning to travel through the tubular body. Within both calculations, the process of the tissue both entering and exiting the device is not included.

Transportation efficiency

Transportation efficiency comprises whether the travelled distance of the threads corresponds with the translation of the tissue. Within an ideal scenario, these values are identical. However, whenever friction between the thread and tissue is insufficient, slip occurs, decreasing the translation of the latter with respect to the former. This can for example be caused by inadequate contact points between both, due to larger experienced friction between the tissue and tubular wall of the device, or due to gravity forces adverse to the direction of removal. Since time $[s]$ is measured within the experiments, the transportation efficiency is calculated as indicated within Equation 2. Within this equation, $\eta_{transportation}$ represents the transportation efficiency in $[\%]$ and $t_{theoretical}$ and $t_{measured}$ the theoretical and actual translation time respectively in $[s]$. The theoretical translation time is calculated with the use of Equation 3. The rotational velocity of the motor, RPM_{motor}, is converted to the corresponding rotational velocity of the spur- and therefore bevel gears, by multiplying this variable with the teeth ratio of the internal and spur gear, $teeth_{internal}$ and $teeth_{spur}$ respectively. The fraction of the travelled tissue distance, Δx_{tissue}, divided by the circumference of the pulley directly attached to the bevel gear, c_{pulley}, determines the theoretically required amount of rotations for this translation. Dividing the second element by the first and multiplying with a factor of sixty results in the theoretical translation time. Note that a perfect transmission between gears and between the clamping axes and thread is assumed.

$$\eta_{transportation} = \frac{t_{theoretical}}{t_{measured}} * 100 \tag{2}$$

$$t_{theoretical} = \frac{\Delta x_{tissue}}{c_{pulley}} / (RPM_{motor} * \frac{teeth_{internal}}{teeth_{spur}}) * 60 \tag{3}$$

Transportation reliability

Lastly, the variable transportation reliability indicates whether all tissue phantoms are successfully transported within the executed experiments. Phenomena such as clogging or malfunctioning of the device are unacceptable within medical procedures. The transportation reliability, r, expressed as a percentage $[\%]$ is calculated as indicated within Equation 4. $n_{successful}$ represents the number of times in which the tissue phantom is successfully transported through the tubular body of the device and n_{total} is the total amount of experiments executed. This variable is aimed to be as high as possible.

$$r = \frac{n_{successful}}{n_{total}} * 100 \tag{4}$$

4.3 Experimental setup

The setup shown in Figure 24 is used throughout the experiments. The medical instrument is mounted in a PMMA standard and supported in two fixed locations without contacting the thread. One of the five holes within the cone is orientated perfectly towards the point of vision, making the detection of the transported tissue phantoms easier. Four screws enable tightening of the device within the setup, preventing both translation and rotation of the concerning. Inserted helicoils permit executing this operation repeatedly. Behind the gearbox, a motor (Igarashi 33GN2738-132-GV-5 50:1, 12V [6]) is introduced and used to actuate to rotational movement of the internal gear. This is facilitated by attaching the axis of the motor by means of a shape lock to the internal gear, as previously shown in Figure 13. Equivalently, the motor is mounted in the PMMA standard and clamped with four screws. A power supply is attached to the motor for customizable actuation.

Furthermore, a black line drawn on the outside of the internal gear enables the determination of the rotational velocity, which is expressed in RPM. Also, the knot used to tie both ends of the thread to one another is marked black and is used as a reference for the rotational speed of the thread. No exact velocity is calculated in this manner. However, it appeared of use whilst making an estimation of slip occurs between the clamping gears and thread. To maintain as much visual information as possible, the outer tube is excluded throughout the experiments. Tests have been executed with the instrument both containing the stainless steel and PTFE-coated thread. However, since the latter seemed more robust and resulted in more smooth translation, this thread is used throughout the final experimental validation.

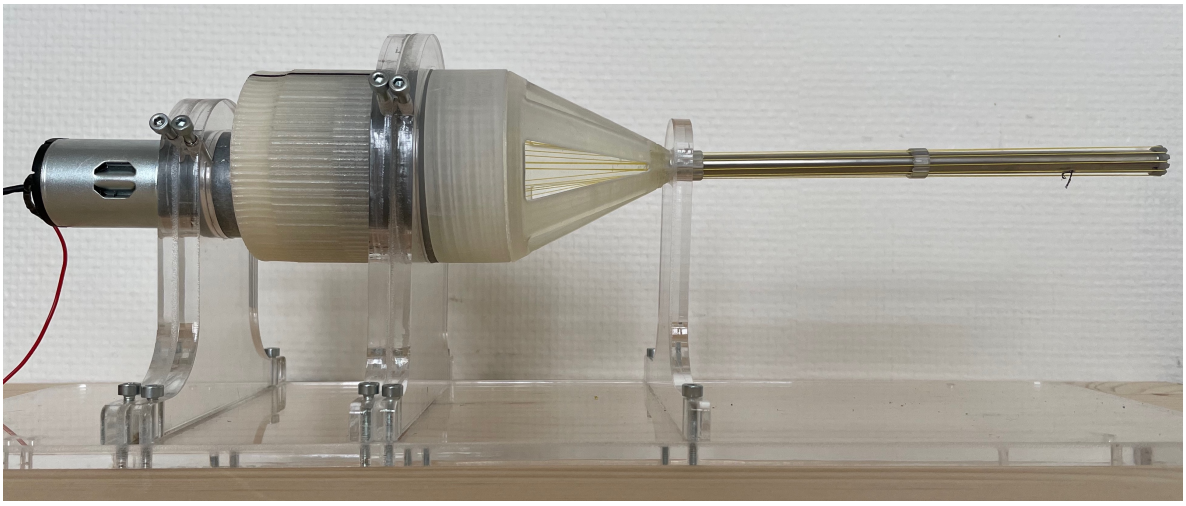

Figure 24: Proof of principle prototype mounted in a PMMA standard.

Tissue phantoms with a weight percentage of 3, 9 and 12, were made as described within Subsection A.7. Red food colouring is added to enhance visibility. To ensure identical sample sizes, the different gelatine mixtures are poured into moulds, containing cylindrical cutouts with a diameter and height of five and fifteen millimetres respectively. Subsequent to the solidifying of the contents, including a minimum and maximum of 12 and 24 hours of refrigerator time respectively, each cylinder is extruded for a one-time use within the experiments. The half-cylindrical tissue phantoms are cut manually by splitting the aforementioned cylindrical shapes.

4.4 Experimental protocol

Experiments were executed with the proof of principle prototype in order to get insights into the dependency of different tissue elasticities on three different variables; rotational velocity, instrument orientation, and tissue phantom shape. This resulted in thirteen experiments, each with varying conditions, as summarized in Table 1. Each individual experiment was performed with a total of ten tissue phantoms.

Table 1: Setup of executed experiments using the proof of principle prototype. Each experiment is executed with ten tissue phantoms, resulting in a total of 130 transported tissue phantoms.

Experiment	1	2	3	4	5	6	7	8	9	10	11	12	13
Power supply (V)	8.5	8.5	8.5	11	11	11	13.5	13.5	13.5	11	11	11	11
Tissue phantom (wt%)	12	9	3	12	9	3	12	9	3	12	9	3	9
Device orientation (°)	0	0	0	0	0	0	0	0	0	-20	-20	-20	0
Tissue phantom shape	○	○	○	○	○	○	○	○	○	○	○	○	$\frac{1}{2}$○

All experiments are executed as follows. After mounting the device in the PMMA setup, the electromotor is powered by a specific battery voltage, 8.5, 11, or 13.5, dependent on the executed experiment. Once the rotational velocity has reached its steady state, the tissue phantom is inserted manually at the tip of the device, after which the rotating thread pulls the concerning inside and transports the phantom through the instrument. Once the tissue phantom travelled the entire distance through the tubular body and is visible within the handle, the measurement is terminated and the last part of the tissue phantom is pushed out of the tube by means of a slender rod. After this, the process is repeated with a new tissue phantom, a total of ten times for all individual experiment combinations. Note that each tissue phantom is thus only used once to prevent potential damage of the concerning influencing the results. Each experiment is filmed within one tape for all ten measurements.

4.5 Data analysis

The experimental data is analysed as follows. Firstly, all footage is evaluated manually to extract the RPM of the internal gear and the required time for each tissue phantom to travel through the tubular body of the device. This time is approximated at millisecond accuracy, by systematically freezing the video frames. Within Figure 25, several snapshots are displayed of a tissue phantom entering and exiting the tubular body. Corresponding configurations in which the start and end time are determined, used to calculate the transportation rate, are indicated additionally. Insertion and exertion times are thus not included in the data analysis. As the lengths of the tissue phantom and inner tube are fifteen millimetres and centimetres respectively, the accounted transported distance is determined to be 135 millimetres. Further, the rotational velocity is approximated by counting the number of times the black line passes by throughout all ten measurements, divided by the total experiment time. The retrieved information is processed within Matlab, whereby Box-plots and statistical analysis are utilised to gain insights. Concerning the latter, both one-way ANOVA and independent two-sample t-tests are performed.

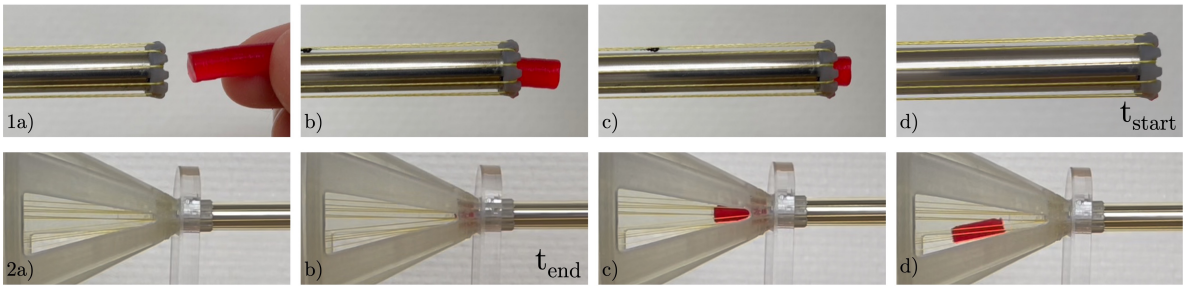

Figure 25: Snapshots of a tissue phantom entering (1) and exiting (2) the tubular body of the device, indicating the configuration in which the start and end times are determined, used to calculate the transportation velocity.

4.6 Results

The experimental outcomes and corresponding data analysis within Matlab can be found within Subsection A.9.

4.6.1 Transportation velocity

Influence rotational velocity
The data extracted from experiment one to nine is graphically displayed within Figure 26. Within these experiments, the goal was to gain insights into the dependency of transportation velocities of tissue phantoms with differing elasticity properties on the rotational velocity of actuation. Note that identical power supply voltages do not directly imply equivalent rotational velocities. This is due to different friction forces between the thread and instrument between the experiments as a result of varying thread tension. Therefore, no absolute values can be retrieved from the comparison between tissue elasticity groups, the relative outcomes are merely indicative. However, it can be seen that an increase in rotational velocity subsequently increases the transportation rates for all three categories. Statistically significant difference in the transportation velocity caused by deviating power supply is established through one-way ANOVA analysis, $[F(2,27) = 33.13, p = 5.40e-08]$, $[F(2,27) = 53.55, p = 4.01e-10]$, $[F(2,27) = 316.82, p = 1.80e{-}19]$ for the 3, 9 and 12 wt% gelatine tissue phantom categories respectively. It is not demonstrated that the maximum transportation velocity as a result of an increase in rotational velocity is achieved. Namely, no stagnation and corresponding equilibrium are retrieved. Currently, the highest transportation rates are attained through a 13.5 voltage power supply for all three groups, resulting in a mean velocity of 58.16 ∓ 3.59, 63.23 ∓ 11.24, and 66.75 ∓ 4.19 $\frac{mm}{s}$ for the 3, 9, and 12 wt% gelatine tissue phantoms respectively. This resembles a mean mass rate of 7.75 ∓ 0.48, 8.43 ∓ 1.50, and 8.90 ∓ 0.56 $\frac{g}{min}$ accordingly, assuming a sample mass of 0.3 gram. The highest variance is measured whilst transporting 3 wt% gelatine tissue phantoms with a power supply of 8.5 V, resulting in a mean velocity of 25.80 ∓ 13.88 $\frac{mm}{s}$.

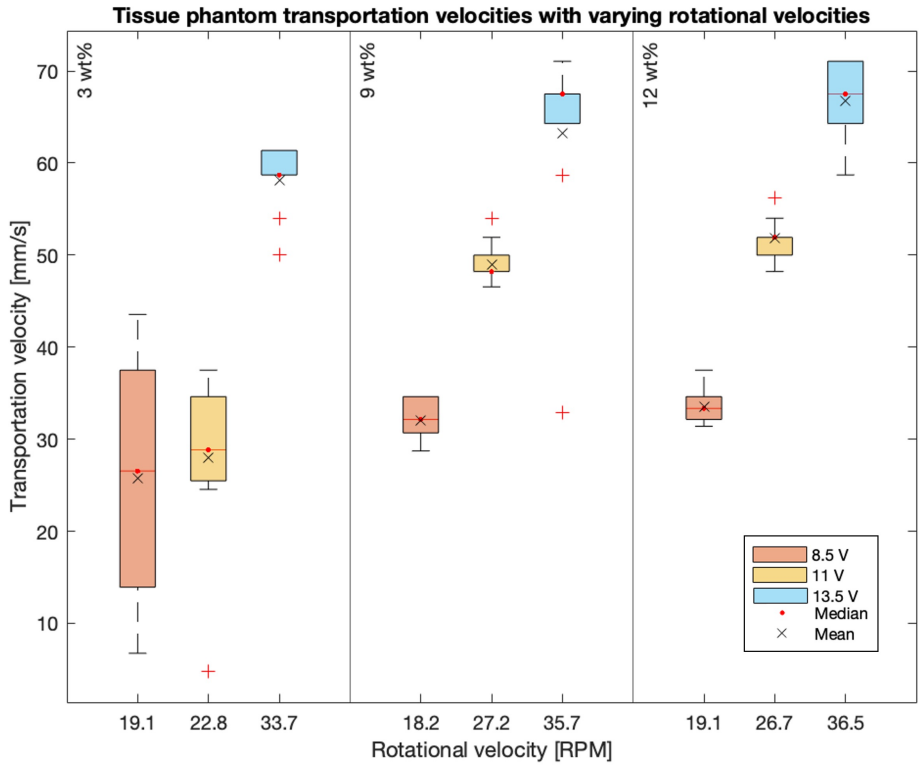

Figure 26: Boxplot graph displaying transportation velocities of all three weight percentage gelatine tissue phantom categories as a result of varying rotational velocities. Outliers are plotted individually using the red '+' marker symbol.

Influence instrument orientation

Within Figure 27, data extracted from experiments four to six and ten to twelve are graphically displayed. This time, the transportation velocity is measured with varying instrument orientations for all three weight percentage gelatine tissue phantom categories. However, the constant power supply of 11 V did not result in identical rotational velocities throughout the experiments, again as a result of varying friction forces between the thread and instrument. For the 9 and 12 wt% gelatine tissue phantom categories, higher velocities were attained whenever the device is oriented horizontally when compared to the tip pointing downwards at an angle of twenty degrees. This is confirmed by the results of the performed independent two-sample t-tests, indicating significant different transportation velocities, $[h = 1, p = 5.38e-04]$ and $[h = 1, p = 3.47e-07]$ for the 9 and 12 wt% gelatine tissue phantoms respectively. However, the attained rotational velocities are additionally greater within these cases, making it unjustified to distinguish the decisive factor. The rotational velocities within the 3 wt% gelatine phantom category are more in line. Within this category, no significant difference is statistically defined between the transportation velocities within varying instrument orientation, $[h = 0, p = 0.3511]$.

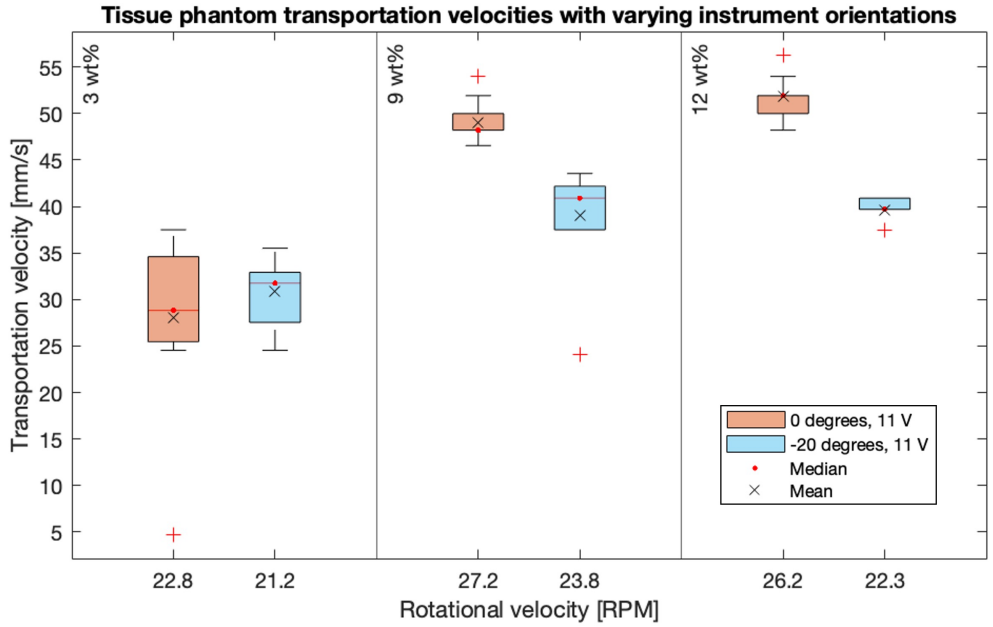

Figure 27: Boxplot graph displaying transportation velocities of all three weight percentage gelatine tissue phantom categories as a result of varying instrument orientations, all actuated with a power supply of 11 V. Outliers are plotted individually using the red '+' marker symbol.

Influence tissue phantom shape

Lastly, different shapes of tissue phantoms were transported within the proof of principle prototype. This experiment is only executed for 9 wt% gelatine tissue phantoms with a corresponding power supply of 11 V. The results are graphically summarized in Figure 28. The executed independent two-sample t-test indicates significant difference in transportation velocities of cylindrical and half-cylindrical gelatine tissue phantoms, $[h = 1, p = 1.4582e-07]$. However, this outcome is unjustified due to the high deviation in rotational velocity.

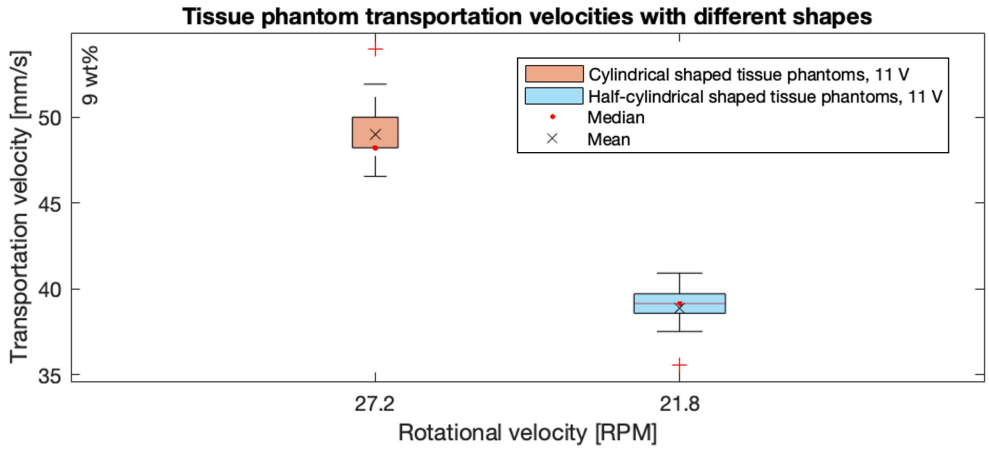

Figure 28: Boxplot graph displaying transportation velocities of all three weight percentage gelatine tissue phantom categories as a result of varying tissue phantom shapes, all actuated with a power supply of 11 V. Outliers are plotted individually using the red '+' marker symbol.

4.6.2 Transportation efficiency and reliability

The transportation efficiency of the device is determined as indicated within Equation 2 and Equation 3. The results, based on the mean tissue transportation time and rotational velocity of the internal gear of each experiment, are displayed within Table 2. As the calculated efficiency occasionally exceeds the limit of one hundred percent, the scaled efficiency, by adjusting the value of the bending radius of the thread around the pulley within Equation 3, is added. This will be further elaborated within Section 5.2.2.

Table 2: (Scaled) transportation efficiency based on the measured mean tissue transportation time and rotational velocity.

Experiment	1	2	3	4	5	6	7	8	9	10	11	12	13
Power supply (V)	8.5	8.5	8.5	11	11	11	13.5	13.5	13.5	11	11	11	11
Tissue phantom (wt%)	12	9	3	12	9	3	12	9	3	12	9	3	9
Device orientation (°)	0	0	0	0	0	0	0	0	0	-20	-20	-20	0
Tissue phantom shape	○	○	○	○	○	○	○	○	○	○	○	○	$\frac{1}{2}$○
Efficiency (%)	103	103	53	114	104	50	108	100	102	104	95	85	103
Scaled efficiency (%)	91	91	47	100	91	44	95	89	90	92	84	75	91

On average, the scaled mean transportation efficiency is 60, 90 and 95 percent for 3, 9 and 12 wt% circular gelatine tissue phantoms respectively within a horizontally oriented device. Efficiency decreases whenever the tip is pointed downwards at an angle of 20 degrees with 8 and 7 percentage points (scaled) within the 9 and 12 wt% gelatine tissue phantom categories respectively. Efficiency remains identical in the case where the tissue phantoms are halved, and thus adjusted in shape. Within the table, two outliers can be detected. Within experiments three and six, transporting 3 wt% gelatine tissue phantoms with a power supply of 8.5 and 11 V, efficiency is significantly lower, resulting in a scaled efficiency of 47 and 44 percent respectively. Remarkably, this is not the case within experiment nine, transporting 3 wt% gelatine tissue phantom with a power supply of 13.5 V. Another striking observation is the enhanced transportation efficiency of the 3 wt% gelatine phantoms in the case where the tip is pointed downwards in an angle of twenty degrees. In this experiment, the scaled efficiency is increased by 31 percent point.

Lastly, all tissue phantoms were transported successfully through the tubular body of the device, resulting in a reliability of 100%. However, it should be noted that repair of the device in between experiments is deemed necessary. Within Subsection A.8, photographs of these occurrences are displayed.

5 Discussion

5.1 Summary of main findings

Within the ideation phase of this research, an overview of requirements and wishes that the device should satisfy was drawn up. With the created proof of principle prototype in mind, this list is displayed once more within Table 3. The corresponding status of each element is indicated.

Table 3: List of requirements and wishes including the status based on the proof of principle prototype. The symbols represent the following; ✓: satisfied, –: unknown, and χ: not satisfied.

Functional requirements

	Requirement	**Status**
1	The mechanism enables continuous transportation of tissue	✓
2	The mechanism enables transportation of tissue with a young's modulus range of 1-110 kPa [4] [2]	✓
3	The mechanism enables a minimum mean transportation rate of 0.25 ∓ 0.04 g/min [27]	✓
4	The reliability of the device is 90% at minimum	✓

Procedural requirements

	Requirement	**Status**
5	The device has a maximum outer and minimum inner diameter of ten and five millimetres respectively	✓
6	The mechanism enables a minimal work length of 125 cm [18]	–
7	The device does not damage surrounding tissue	✓
8	The device is biocompatible for in-vivo surroundings	✓
9	The device is operatable by one user	✓

Functional wishes

	Wish	**Status**
1	The transportation rate does not statistically vary between different tissues within the elasticity range of 1-110 kPa	–
2	The mean transportation rate is maximised with a minimum of 6.2 g/min [5]	✓
3	The reliability of the device is 100%	✓
4	The operability of the device is independent of the shaft orientation	χ
5	The operability of the device is independent of tissue heterogeneity	–
6	The device enables tissue transportation within a curvature of 90° [16]	χ
7	The device does not damage transported tissue	χ

Procedural wishes

	Wish	**Status**
8	The mechanism is suitable for a working length of 153 cm [18]	–
9	The device is flexible	χ
10	The device is reusable	✓
11	The device is cleanable	–
12	The number of components are minimised	✓

The proof of principle prototype enables continuous transportation of tissue within a young's modulus range of 1-110 kPa, mimicked by means of 3, 9, and 12 wt% gelatine tissue phantoms. The maximum mean mass transportation rate of these categories is measured to be 7.75 ∓ 0.48, 8.43 ∓ 1.50, and 8.90 ∓ 0.56 $\frac{g}{min}$ respectively, laying within the range of transportation rates of clinically available morcellator operated during laparoscopic surgery [5]. Higher rotational velocities significantly increase transportation rates for all three categories, as this increments the translation rate of the thread. It is not demonstrated that the maximum transportation velocity as a result of an increase in rotational velocity is achieved as no stagnation and corresponding equilibrium are retrieved. Whether statistically, variance in transportation rates between the different wt% gelatine tissue phantoms appears is not determined, as equivalent power supply voltages did not result in identical rotational velocities. This implies varying friction forces between the thread and instrument between the experiments as a result of differing thread tension.

Transportation efficiency increases for tissue phantoms with higher elasticity properties. It is hypothesized that soft tissues are more likely to deform or shear near the thread surface, being more sensitive to slip. At the other extreme, stiffer tissues clamp within the thread loops and therefore experience high friction between both, beneficial for the developed transportation mechanism. However, based on the current measurements, it can not be said with certainty whether a decrease in efficiency is due to the mentioned slipping between the tissue and thread, due to imperfect transmission between the gears and thread, or both. Concerning shaft orientation, a (scaled) efficiency loss of 8 and 7 percentage points was measured in the case of pointing the tip of the device downwards at an angle of twenty degrees when compared to horizontal operation, for transportation of the 9 and 12 wt% gelatine tissue phantoms respectively as gravity results in a force on the tissue opposite to the direction of removal. Concerning the 3 wt% gelatine tissue phantoms, the scaled efficiency is increased from 44% to 75% when pointing the tip downwards. As this contradicts the previous statement, it is hypothesized that fluctuation of the rotational velocity of the internal gear, substantiated by the high variance seen in Figure 26, and slipping between the gear and thread influences the results of the former experiment. This is additionally the case for the comparable experiment executed with a power supply of 8.5 V. Since the scaled transportation efficiency of these phantoms is almost doubled within the experiment powered by means of 13.5 Volt, the belief that the tissue phantom weight percentage is not the only contributing factor is strengthened. Besides, a higher rotational velocity is at higher risk of resulting in slipping between the tissue and thread, again in favour of the described hypothesis. Furthermore, efficiency remains identical in the case where the tissue phantoms are halved, and thus adjusted in shape. It is expected that the decrease in tissue phantom volume and weight measures up to the decrease in contact points between the concerning and thread. Alternatively, it can be hypothesized that not all contact points are required in the first place for friction-based transport of the tissue.

Damage to transported tissue is not excluded, since remains of tissue phantom were detected on the thread, especially when transporting the 3 wt% gelatine tissue phantoms. These phantoms are expected to be more sensitive due to the lower young's modulus, indicating a reduced stiffness. Experiments determining the operability dependency on tissue heterogeneity have not been executed. Throughout the experiments, all tissue phantoms were transported successfully through the tubular body of the device, resulting in reliability of 100%. However, it should be noted that repair of the device in between experiments is deemed necessary.

Regarding the procedural requirements and wishes, the rigid tubular body of the device has an outer and inner diameter of ten and five millimetres respectively and a working length of fifteen millimetres. The influence of enlarging the latter has not been tested. The rotation of the thread is shielded through an outer tube and the distal ends of the loops are slightly countersunk within the tip, to secure surrounding tissue. Since all components within the device consist of stainless steel and bio-compatible resins, suitability for in-vivo surroundings is ensured. The device is actuated through the rotation of an internal gear. Assuming that one hand is utilised to hold the device whilst the other excites the rotating motion, the device is operatable by one user. In the case of motorized actuation, the required actions are even reduced. All experiments have been executed using the same device, demonstrating reusability. However, cleanability, specifically concerning the thread, has not been established. Lastly, the number of components within the device is minimised by making use of additive manufacturing.

5.2 Limitations

5.2.1 Device limitations

The proof of principle prototype showcases the working principle of the designed mechanism. However, after excessive usage, several design limitations came to light. Different situations encountered during the experiments are shown in Subsection A.8. As expected, undesired friction occurs between the spanned thread and the tip of the instrument. Due to rotation of the former, a cutting motion arises, slowly destroying the tip. Subsequently, the bending radius of the thread decreases, whereby the thread eventually scrapes along the distal end of the inner tube. Due to this significant increase in friction, the device loses its functionality. This phenomenon appeared to apply to both implemented threads, made out of stainless steel and PTFE-coated, in which the wearing process is expedited for the former. Besides this, occasionally, axes, originally clamped within the gear base, loosened throughout usage. Whenever this results in relocation of gears, functionality is obstructed. The hypothesised cause of this occurrence and the potential solution will be addressed later on in this chapter. Further, during assembly, careful handling of the thread is of importance. Especially applicable for the stainless steel wire, whenever slightly damaged, the thread starts to unravel, subsequently obstructing its translation.

As stated within the goal of this research, the designed proof of principle prototype merely focuses on the transportation of tissue. However, it should be noted that the operations of tissue extraction and tissue retrieval are of equal importance for an all-encompassing medical device. Concerning the former, interesting to mention is the ability of the designed device to pull the tissue phantom inwards. Only a small area of contact resulted in the device pulling the tissue within individually. Subsequently, regarding tissue extraction, whenever the tissue reaches the proximal end of the tubular body, the translation velocity of the tissue rapidly decreases due to the gradual loss in contact area with the thread. Namely, within the handle, the loops of thread are redirected for actuation, resulting in an increase in diameter and distribution between the concerning. Due to this occurrence, the tissue remains partially trapped within the tubular body. Within the experiments, the tissue is pushed utilizing a slender rod to bridge this last part. Subsequently, the tissue either tumbles outside of the handle through the gaps, remains trapped within the handle body or sticks on one of the loops of thread and is subsequently translated into the gearbox. The latter is highly undesirable since this potentially clogs the actuation mechanism and damages the tissue sample. Within the experiments, this occasionally occurred, after which the device maintained its functionality but crushed the tissue phantom between the gears. This phenomenon is more common for the 3 wt% tissue phantom due to a higher degree of stickiness.

5.2.2 Experiment limitations

The executed experiments give insights into the operability of the designed prototype. However, several limitations should be noted. Firstly, the rotational velocity of the actuation is varied between experiments by altering the power supply of the electromotor, expressed in voltage. Dependent on the at that time experienced resistance, this results in a specific rotational velocity of the internal gear, which is thus not necessarily identical within each experiment powered with the same voltage. This again relates to thread tension's influence, in which both desired and undesired friction should be perfectly balanced. Even though the average rotational velocity of each experiment is computed, the resulting tissue transportation velocities are not scaled accordingly, an aspect that should be carefully reckoned with within data analysis.

Secondly, even though the voltage input increases the speed of revolution of the internal gear, it does not directly imply that this motion is perfectly transmitted to the rotation of the thread. Namely, slip can occur between the clamping axes and thread. The knot, used to tie both ends of the thread, provides visual information regarding this manner. Before each experiment, it was aimed to align both rotational velocities as much as possible. However, this remains an educated guess and throughout the experiments, the prior optimum is occasionally no longer satisfied, due to for example disturbances or wear, altering the conditions. In general, the rate of thread rotation was more likely to decrease over time. This occurrence is not taken into account in the calculations concerning efficiency. In other words, it is unknown whether a decrease in efficiency is the result of imperfect transmission between the revolving axes and thread, or due to slip between the thread and tissue phantom. For future experiments, it is advised to measure the RPM of the thread additionally.

Furthermore, multiple efficiency percentages exceeded the limit of a hundred percent, calculated with the use of Equation 2 and Equation 3. Two contributing factors are hypothesized for this implausible occurrence. Firstly, manual data extraction of the tissue transportation time and corresponding RPM can lead to inaccuracies, justifying minor offsets. Secondly, only one variable remains, since the other elements are factual. This concerns the radius of the thread wrapped around the rotational axis, used to calculate the circumference of the pulley. This radius is determined as shown in Figure 29, from the centre of the pulley to the heart of the thread. Namely, this determines the rotational velocity of the thread. The outsides of the thread either exhibit a smaller or larger transportation rate whenever travelling along the curvature of the pulley. The radius is measured to be 3.025 millimetres. However, this is based on the computational model. When making use of additive manufacturing, clearances often come out smaller in reality than designed. Additionally, in the case of the utilised Formlabs printer, it can occur that undesired resin cures prior to washing the component. This would result in a more narrow and less deep V-groove, subsequently increasing the indicated radius. Within the adjusted efficiency outcomes, this variable is scaled until all values meet the boundaries. This resulted in a radius of 3.43 millimetres. However, absolute values should still not be taken too literally since this is an educated guess. Additionally, this solution potentially contradicts the suspicion of the thread slightly cutting into the pulley due to the material properties of the chosen resin, therefore enhancing the clamping functionality.

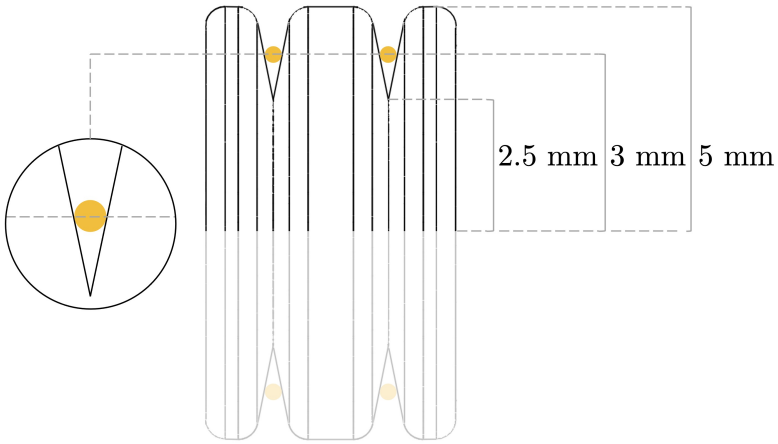

Figure 29: Image indicating the determination of the thread radius used to calculate the device efficiency.

Besides this, due to excessive usage, play occurred within the shape lock between the axis of the motor and internal gear. This eventually resulted in an uncoupled movement but might have prohibited a perfect transmission prior to this failure. The same applies to the utilised PMMA standard. Even though it fulfilled its functionality, movement within the setup might have slightly influenced experimental output. Also, it should be emphasized that experimental validation is executed with the proof of principle prototype containing the PTFE-coated thread. This decision is made since the wear of the tip appeared slower when rotating this thread and slightly less force is required for actuation when compared to the instrument containing the stainless steel thread. However, the final design does include the latter thread, due to other advantages such as improved mechanical properties, bio-compatibility, and limited creep. Additional experiments are required to gain insights into how this variable influences operational capacities. Also, including the outer tube throughout these measurements is required to exclude potential effects as currently hypothesized.

5.3 Recommendations

5.3.1 Redesigns enhancing force distribution

Failure between experiments within the actuation mechanism of the device can to a large extent be explained from a dynamical perspective, analysing the distribution of forces. The applied forces are transmitted in the following hierarchical order. The rotation of the internal gear puts all spur gears in motion which are joined to the bevel gears, translating the angle of rotation in the appropriate direction for the clamped loops of thread. The concerning components are indicated within Figure 12.

Within the current design, whenever play occurs within the vertically secured axes, the direction in which the internal gear rotates influences performance. Namely, in the case of rotation away from the vertical supports, the axis of the spur gear tends to tilt in the same trajectory, due to a resulting horizontal force in the unfavourable direction, increasing clearance between both bevel gears. This is schematically displayed within Figure 30(a) and can be explained through the phenomenon of 'the path of the least resistance'. Namely, within this occurrence, tilting of the axis results in less friction when compared to transmitting the rotation to perfectly aligned bevel gears, due to the spanned thread. This is undesirable since this prohibits perfect transmission between the gears. Within a redesign, this phenomenon can be prevented by ensuring perfectly fastened vertical axes. Elements through which this can be achieved are for example optimising tolerances, exploring different methods of fastening, extending the length of the axis within the gear base, or physically blocking the motion in the other direction. Fortunately, within the current design, the desired direction of rotation, translating tissue outside the human body, is a result of rotation directed towards the vertical supports which can resist the resulting horizontal force Figure 30(b).

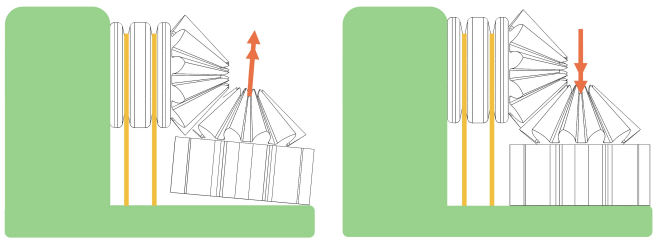

Figure 30: Schematic representation of the influence in which direction the internal gear is rotated whenever play occurs within the vertical axis. (a) resembles the internal gear rotating away from the vertical support whilst (b) resembles the opposite direction.

Within Subsection A.11, a figure is shown indicating the forces between rotating bevel gears. Within the designed mechanism, rotation of the spur gear actuates rotation of the vertically oriented bevel gear. The torque is transmitted in a tangential force. Further, as stated by [10], the axial and radial forces acting on the bevel gear joined to the spur gear equal the radial and axial forces acting on the bevel gear joined to the axis clamping the loops of thread respectively. This is the case since both bevel gears are identical, meeting at an angle of forty-five degrees. However, an uneven distribution might be desirable as the vertical supports provide less mechanical performance when compared to the gear base. This is due to the fact that the former are separate elements with limited volume as a result of dimensional restrictions. Within a redesign, the angle between both bevel gears can potentially be adjusted, subsequently optimising force distribution.

Lastly, the pulling force of the tensioned thread highly impacts the running gears. This load results in a downwards force, subsequently absorbed by both the vertical support and other bevel gear. In an ideal situation, this force is evenly distributed over both elements and deformation is identical. Namely, in this case, the axis consisting of the loops of thread remains perfectly horizontal, schematically indicated within Figure 31(a). However, it is suspected that this is not the case within the current design. It appears that either due to clearance between gears or due to the elasticity of the bevel gear, the axis is tilted downwards. Whenever this results in plastic deformation of the hole within the vertical holder containing the horizontal axis, play arises, see Figure 31(b). Subsequently, resonance throughout the operation is no longer perfectly absorbed, resulting in the axis gradually vibrating out of the holder.

Within a redesign, this phenomenon can be prevented through several approaches. Ideally, unevenly distribution of the thread pulling force should be prevented. However, as deviating properties of both the gear base and gears might be desired and manufacturing inaccuracies are inevitable, another approach might be more effective. For example, by extending the horizontal axis and subsequently supporting both ends as shown within Figure 32(c). Subsequently, tilting of the concerning is less likely to occur. However, within the current design, it is not achieved to implement this due to multiple reasons. When extending the horizontal axis in the current setup, bridging the other bevel gear, the opposite side of the axis ends at the height of the internal gear. Implementing a similar vertical support would therefore interfere with the rotation of this internal gear. Enlarging the size of the handle does not prevent this occurrence, since the spur gear should always remain in contact with the internal gear and the orientation of the horizontal axis is fixed to perfectly align the loops of thread towards the centre of the device. However, when making use of additive manufacturing to its extremity, it might be possible to work around this obstacle.

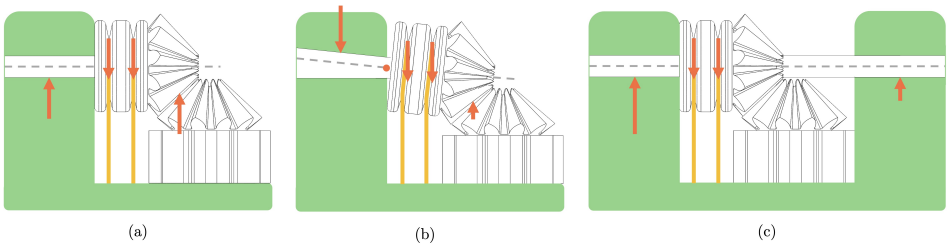

Figure 31: Schematic representation of the reaction forces caused by the spanned thread, (a) resembles the ideal, evenly distributed, situation, (b) resembles an unevenly distributed situation, in which play occurs within the hole containing the horizontal axis and (c) resembles the proposed redesign.

5.3.2 Redesigns enhancing material implementation

As discussed multiple times, friction is both desirable and undesirable within the designed device. It is experienced that lubricating the gears significantly improved the ease of rotation. However, contamination of the thread is difficult to avoid due to the proximity of these elements. Within Figure 32(b) a redesign possibility is displayed, working around this obstacle. Namely, within this design, the axis clamping the thread and the bevel and spur gears are split and shielded by means of the vertical holder, containing the horizontal axis. The gears are fixed along the rotating axis, contrary to the current design in which the static and dynamic components are reversed. This setup simultaneously facilitates implementing different materials for the divided segments. More rubber-like materials might be advantageous to enhance the clamping functionality, whilst the trustworthy transmission is the principal factor for the material selection of the bevel gears.

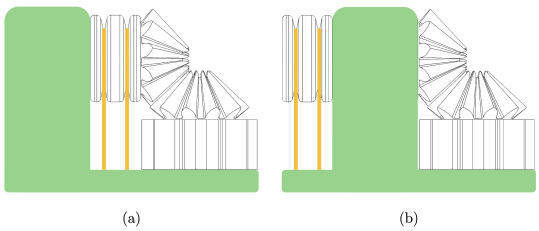

Figure 32: Schematic representation of an implementation of gears within the gear base, (a) resembles the current design and (b) resembles the proposed redesign in which material implementation is enhanced.

As mentioned in the previous section, failure of the tip is disastrous for the operability of the device. Therefore, it is recommended to make use of an alternative material for this component. Besides resistance against the cutting motion of the thread, low friction between the thread and tip is of importance. Additionally, the material should be biocompatible with in-vivo surroundings. A potential material selection might be copper. However, the manufacturability of the high level of detail of the tip might eliminate potential candidates and should therefore be considered carefully.

5.3.3 Redesign tensioning mechanism

As stated within W6 and W9, a bendable device is desirable. Laparoscopic instruments enable tissue removal through a rigid shaft whilst catheters consist of a flexible tubular body. The latter is advantageous due to the ability to navigate through the human body, minimising damage to surrounding tissue and expanding reach. When positioning the device within a curvature, a length difference occurs between paths along the tube. For example, the inner curvature will be shorter when compared to the outer curvature. To maintain tension along all loops of thread, the corresponding tensioning mechanism and thread implementation ought to be adjusted. Namely, currently, one thread consists of all loops which can be spanned jointly by rotation of the cap, gradually extending both outer ends. However, to differentiate between lengths, it is more logical to increase the number of threads and subsequently decrease the number of loops per thread and tension these separately.

Within Figure 33, the first idea of such a system is displayed. The gear base consists of five separate islands, each containing one point of actuation. By rotating the screw on which these are mounted, the element can either be lowered or highered, spanning or releasing the concerning thread. Namely, turning of these islands is prohibited since they are guided along both the mentioned screw and an additional axis, forcing rotation of the screw to be transmitted into a translation of the island. Due to thread inserts within the printed islands, this motion can be actuated repeatedly. Within this design, each point of actuation would contain one thread consistent with two loops. However, it should be tested how the diagonal, arising when both ends of the thread are connected, affects operability. Besides individual tensioning, ensuring loop positioning is a bigger challenge within a flexible device. Namely, without active prevention, it can be anticipated that the spanned tubular body within the inner tube will not maintain its hollow configuration when bent. Additionally, whenever the thread contacts either the inner or outer tube, additional friction arises.

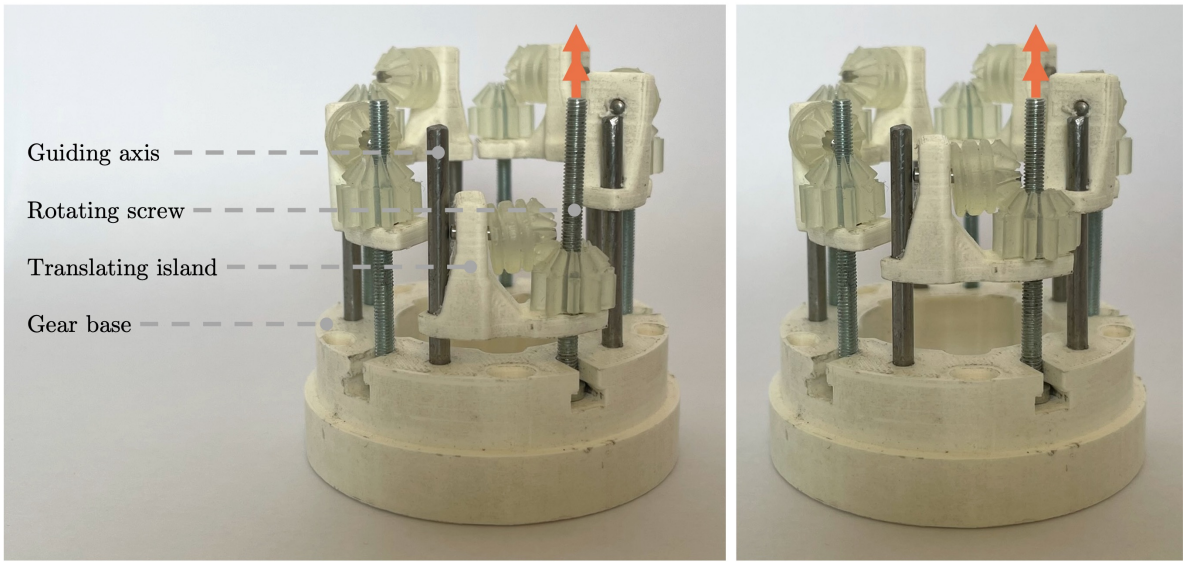

Figure 33: Redesign proposal of the gear base in which individual tensioning of threads is enabled. The separate islands can be translated by rotation of the corresponding screw, as indicated by the orange arrows.

6 Conclusion

The goal of this report was to design a continuous tissue transportation mechanism compatible for MIS in which the transportation velocity is independent of tissue elasticity within the young's modulus range of 1-110 kPa. The designed instrument enables tissue removal based on the working principle of friction. Loops of thread are wrapped around an inner tube and rotated continuously, resulting in a cylindrical conveyor belt. The proof of principle prototype demonstrates the feasibility of the mechanism. Tissue consistent with the specified elasticity properties mimicked utilizing 3, 9, and 12 wt% gelatine tissue phantoms, are all transported successfully, resulting in the reliability of the instrument of 100%. The maximum mean mass transportation rate of these categories is measured to be 7.75 ∓ 0.48, 8.43 ∓ 1.50, and 8.90 ∓ 0.56 $\frac{g}{min}$ respectively. No conclusion is drawn concerning the dependency of these transportation velocities on the corresponding young's modulus of the tissue phantoms. Namely, equivalent power supply voltages used to actuate the mechanism did not result in identical rotational velocities of the gears and therefore thread due to varying tension, prohibiting statistic analysis on this matter. A trade-off considering thread tension occurs, as it is beneficial for the clamping of the thread and spanning of the tubular body whilst it is at the expense of friction experienced at the tip, increasing the required actuation force.

For future iterations, several improvements are advised, concerning the design of the device and the experimental setup. The former include material optimization, enhancing mechanical properties of the gearbox, including tissue extraction and retrieval functionalities for an all-encompassing device, introducing a flexible tubular shaft, and additional research concerning reusability and cleanability. For the experimental setup, it is advised to maintain a stable rotational velocity of the internal gear through a varying power supply and to include the subsequent rotation of the thread within the measurements. Further recommendations concern the material of the implemented thread, including the outer tube throughout the experiments, mapping potential damage to transported tissue, experiments varying tissue heterogeneity, digitising manual data extraction and improving calculations of the device efficiency.

To conclude, the proof of principle prototype introduced within this research enables the removal of a large range of tissue that can all be encountered during MIS. The achieved transportation velocities lay within the rates of clinically available morcellator operated during laparoscopic surgery. Potential barriers of the currently golden standard aspiration catheter are overcome, such as the risk of clogging, damage hazard to surrounding tissue, and the dependency of the force of removal on the diameter of the tubular body. All these elements contribute to the potency of the designed mechanism, which provides a base for future research.

References

[1] *3D Printing Materials For Healthcare*. Formlabs. URL: https://formlabs.com/materials/medical/ (visited on 09/27/2022).

[2] Kemal Arda et al. "Quantitative Assessment of Normal Soft-Tissue Elasticity Using Shear-Wave Ultrasound Elastography". In: *American Journal of Roentgenology* 197.3 (Sept. 2011). Publisher: American Roentgen Ray Society, pp. 532–536. ISSN: 0361-803X. DOI: 10.2214/AJR.10.5449. URL: https://www.ajronline.org/doi/10.2214/AJR.10.5449 (visited on 04/25/2022).

[3] Sarah Cohen and James A. Greenberg. "Hysteroscopic morcellation for treating intrauterine pathology". In: *Reviews in Obstetrics & Gynecology* 4.2 (2011), pp. 73–80. ISSN: 2153-8166.

[4] Kerstyn Comley and Norman A. Fleck. "A micromechanical model for the Young's modulus of adipose tissue". In: *International Journal of Solids and Structures* 47.21 (Oct. 15, 2010), pp. 2982–2990. ISSN: 0020-7683. DOI: 10.1016/j.ijsolstr.2010.07.001. URL: https://www.sciencedirect.com/science/article/pii/S0020768310002465 (visited on 04/25/2022).

[5] Sara R. C. Driessen et al. "Electromechanical Morcellators in Minimally Invasive Gynecologic Surgery: An Update". In: *Journal of Minimally Invasive Gynecology* 21.3 (May 1, 2014), pp. 377–383. ISSN: 1553-4650. DOI: 10.1016/j.jmig.2013.12.121. URL: https://www.sciencedirect.com/science/article/pii/S1553465014000260 (visited on 04/25/2022).

[6] (C) 2020 Conrad Electronic. *Igarashi 33GN2738-132-GV-5 50:1 Gearmotor 12 V — Conrad.com*. URL: https://www.conrad.com/p/igarashi-33gn2738-132-gv-5-501-gearmotor-12-v-244023 (visited on 09/16/2022).

[7] *ENGELMANN Drahtseilfabrik GmbH — Vom Hofe Group*. URL: https://engelmann-online.de/en/ (visited on 07/11/2022).

[8] K. H. Fuchs. "Minimally Invasive Surgery". In: *Endoscopy* 34.2 (Mar. 2002). Publisher: © Georg Thieme Verlag Stuttgart · New York, pp. 154–159. ISSN: 0013-726X, 1438-8812. DOI: 10.1055/s-2002-19857. URL: http://www.thieme-connect.de/DOI/DOI?10.1055/s-2002-19857 (visited on 09/15/2022).

[9] FuseSchool - Global Education. *Inertia — Forces and Motion — Physics — FuseSchool*. Apr. 5, 2020. URL: https://www.youtube.com/watch?v=qBjmO8w-QqU (visited on 05/12/2022).

[10] *Gear Forces — KHK Gear Manufacturer*. URL: https://khkgears.net/new/gear_knowledge/gear_technical_reference/gear_forces.html (visited on 08/23/2022).

[11] Ying Han, Yoshiharu Uno, and Akihiro Munakata. "Does flexible small-diameter colonoscope reduce insertion pain during colonoscopy?" In: *World Journal of Gastroenterology* 6.5 (Oct. 15, 2000), pp. 659–663. ISSN: 1007-9327. DOI: 10.3748/wjg.v6.i5.659. URL: https://www.ncbi.nlm.nih.gov/pmc/articles/PMC4688839/ (visited on 09/16/2022).

[12] Thomas Jaschinski et al. "Laparoscopic versus open appendectomy in patients with suspected appendicitis: a systematic review of meta-analyses of randomised controlled trials". In: *BMC Gastroenterology* 15.1 (Apr. 15, 2015), p. 48. ISSN: 1471-230X. DOI: 10.1186/s12876-015-0277-3. URL: https://doi.org/10.1186/s12876-015-0277-3 (visited on 06/09/2022).

[13] Alireza Karimi and Mahdi Navidbakhsh. "Material properties in unconfined compression of gelatin hydrogel for skin tissue engineering applications". In: *Biomedizinische Technik. Biomedical Engineering* 59.6 (Dec. 2014), pp. 479–486. ISSN: 1862-278X. DOI: 10.1515/bmt-2014-0028.

[14] Esther P. de Kater. "Methods for the Transportation of Substances Executed by Animals". In: (2019), pp. 1–59.

[15] Esther P. de Kater et al. "Design of a Flexible Wasp-Inspired Tissue Transport Mechanism". In: *Frontiers in Bioengineering and Biotechnology* 9 (2021). ISSN: 2296-4185. URL: https://www.frontiersin.org/article/10.3389/fbioe.2021.782037 (visited on 04/25/2022).

[16] Mingyuan Li et al. "VINE Catheter for Endovascular Surgery". In: *IEEE Transactions on Medical Robotics and Bionics* 3.2 (May 2021). Conference Name: IEEE Transactions on Medical Robotics and Bionics, pp. 384–391. ISSN: 2576-3202. DOI: 10.1109/TMRB.2021.3069984.

[17] *liftech*. URL: http://liftechniques.com/pulley_sheaves_effects_wire_ropes.html (visited on 08/22/2022).

[18] Troy D. Long et al. “Novel aspiration catheter design for acute stroke thrombectomy”. In: *Journal of NeuroInterventional Surgery* 11.2 (Feb. 1, 2019). Publisher: British Medical Journal Publishing Group Section: New Devices, pp. 190–195. ISSN: 1759-8478, 1759-8486. DOI: 10.1136/neurintsurg-2017-013702. URL: https://jnis.bmj.com/content/11/2/190 (visited on 04/25/2022).

[19] Jawid Madjidyar et al. “Influence of Thrombus Composition on Thrombectomy: ADAPT vs. Balloon Guide Catheter and Stent Retriever in a Flow Model”. In: *RöFo - Fortschritte auf dem Gebiet der Röntgenstrahlen und der bildgebenden Verfahren* 192.3 (Mar. 2020). Company: © Georg Thieme Verlag KG Distributor: © Georg Thieme Verlag KG Institution: © Georg Thieme Verlag KG Label: © Georg Thieme Verlag KG Publisher: © Georg Thieme Verlag KG, pp. 257–263. ISSN: 1438-9029, 1438-9010. DOI: 10.1055/a-0998-4246. URL: http://www.thieme-connect.de/DOI/DOI?10.1055/a-0998-4246 (visited on 09/15/2022).

[20] Medtronic. *Coronary Aspiration Catheters - Export AP*. URL: https://europe.medtronic.com/xd-en/healthcare-professionals/products/cardiovascular/catheters/export-ap.html (visited on 08/29/2022).

[21] Keval K. Patel, Rahil Rafeedheen, and Tarek Helmy. “5 - Adjunctive Devices for Non-Balloon Coronary Interventional Techniques and Devices: Rotational Atherectomy, Thrombectomy, Cutting Balloons, and Embolic Protection”. In: *The Interventional Cardiac Catheterization Handbook (Fourth Edition)*. Ed. by Morton J. Kern, Paul Sorajja, and Michael J. Lim. Elsevier, Jan. 1, 2018, pp. 159–178. ISBN: 978-0-323-47671-3. DOI: 10.1016/B978-0-323-47671-3.00005-3. URL: https://www.sciencedirect.com/science/article/pii/B9780323476713000053 (visited on 04/29/2022).

[22] Giuliano Perigli et al. “Clinical Benefits of Minimally Invasive Techniques in Thyroid Surgery”. In: *World Journal of Surgery* 32.1 (Jan. 1, 2008), pp. 45–50. ISSN: 1432-2323. DOI: 10.1007/s00268-007-9259-0. URL: https://doi.org/10.1007/s00268-007-9259-0 (visited on 09/15/2022).

[23] Suwatchai Pornratanarangsi et al. “Extraction of challenging intracoronary thrombi: multi-device strategies using guide catheters, distal vascular protection devices and aspiration catheters”. In: *The Journal of Invasive Cardiology* 20.9 (Sept. 2008), pp. 455–462. ISSN: 1557-2501.

[24] *Pronto® Extraction Catheters — US — Teleflex*. URL: https://teleflex.com/usa/en/product-areas/interventional/peripheral-interventions/pronto-extraction-catheters/index.html (visited on 08/29/2022).

[25] *QuickCat Extraction catheter — Philips Healthcare*. Philips. URL: https://www.usa.philips.com/healthcare/product/HCIGTDQKCTEXCT/quickcat-extraction-catheter (visited on 08/29/2022).

[26] T. N. Robinson and G. V. Stiegmann. “Minimally Invasive Surgery”. In: *Endoscopy* 36.1 (Jan. 2004). Publisher: © Georg Thieme Verlag Stuttgart · New York, pp. 48–51. ISSN: 0013-726X, 1438-8812. DOI: 10.1055/s-2004-814113. URL: http://www.thieme-connect.de/DOI/DOI?10.1055/s-2004-814113 (visited on 09/15/2022).

[27] Aimée Sakes et al. “Development of a Novel Wasp-Inspired Friction-Based Tissue Transportation Device”. In: *Frontiers in Bioengineering and Biotechnology* 8 (2020). ISSN: 2296-4185. URL: https://www.frontiersin.org/article/10.3389/fbioe.2020.575007 (visited on 04/25/2022).

[28] *Salomon's Metalen - Product - Salomon's Metalen*. URL: https://salomons-metalen.nl/producten/rvs/capillair (visited on 07/11/2022).

[29] Yubing Shi et al. “Suction force-suction distance relation during aspiration thrombectomy for ischemic stroke: A computational fluid dynamics study”. In: *Physics in Medicine* 3 (June 1, 2017), pp. 1–8. ISSN: 2352-4510. DOI: 10.1016/j.phmed.2016.11.001. URL: https://www.sciencedirect.com/science/article/pii/S2352451016300191 (visited on 09/15/2022).

[30] *Spro Snyper Braid Yellow 0.10 mm*. Fishing Direct Hengelsport. URL: https://www.fishingdirect.nl/product/spro-snyper-braid-yellow-0-10-mm/ (visited on 09/16/2022).

[31] William W. Spurbeck et al. “Minimally Invasive Surgery in Pediatric Cancer Patients”. In: *Annals of Surgical Oncology* 11.3 (Mar. 1, 2004), pp. 340–343. ISSN: 1534-4681. DOI: 10.1245/ASO.2004.04.021. URL: https://doi.org/10.1245/ASO.2004.04.021 (visited on 06/09/2022).

[32] UNSW Physics. *Forces 2b - the Tablecloth trick explanation*. Jan. 28, 2018. URL: https://www.youtube.com/watch?v=Y9NfiaIM6e4 (visited on 05/12/2022).

[33] Jerome D. Waye. "Colonoscopy". In: *Surgical Clinics of North America*. Diseases of the Colon and Anorectum 52.4 (Aug. 1, 1972), pp. 1013–1024. ISSN: 0039-6109. DOI: 10.1016/S0039-6109(16)39799-7. URL: https://www.sciencedirect.com/science/article/pii/S0039610916397997 (visited on 07/21/2022).

[34] Albert J. Yoo and Tommy Andersson. "Thrombectomy in Acute Ischemic Stroke: Challenges to Procedural Success". In: *Journal of Stroke* 19.2 (May 31, 2017). Publisher: Korean Stroke Society, pp. 121–130. ISSN: 2287-6391, 2287-6405. DOI: 10.5853/jos.2017.00752. URL: http://www.j-stroke.org/journal/view.php?doi=10.5853/jos.2017.00752 (visited on 07/25/2022).

[35] Xinge Yu et al. "Needle-shaped ultrathin piezoelectric microsystem for guided tissue targeting via mechanical sensing". In: *Nature Biomedical Engineering* 2.3 (Mar. 2018). Number: 3 Publisher: Nature Publishing Group, pp. 165–172. ISSN: 2157-846X. DOI: 10.1038/s41551-018-0201-6. URL: https://www.nature.com/articles/s41551-018-0201-6 (visited on 04/25/2022).

A Appendices

A.1 Aspiration catheters

Aspiration catheters, also known as suction catheters, are medical instruments used to remove a foreign object, thrombus, or liquid from the human body. As shown in Figure 34, the device consists of a main tube with a proximal and distal end. A suction lumen exists within the main tube with an aspiration port at the distal end. Due to the small diameter of the device, aspiration catheters enable Minimally Invasive Surgery (MIS). By executing a mechanical force on the proximal end of the catheter, which is transmitted through the main shaft, the tip is positioned at the target location. Within some designs, a guidewire connected to the main shaft is advanced to the target location first, after which the rest of the catheter body follows, potentially making the positioning easier. The guidewire is located within a guidewire lumen attached to the main shaft. Subsequent to the positioning, a negative pressure is applied by the suction tool attached to the proximal end of the catheter, transferring the tissue in front of the tip through the lumen outside of the human body.

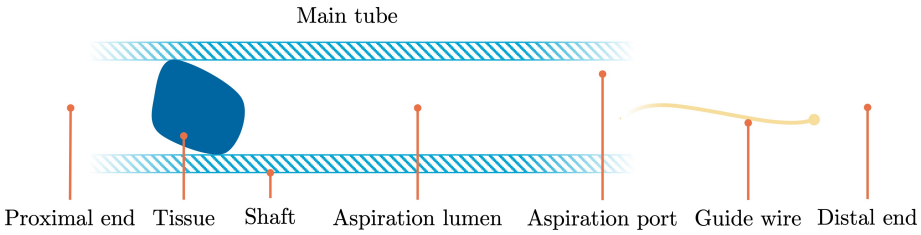

Figure 34: Aspiration catheter

According to [21], in 2018 the three most commonly used thrombectomy aspiration catheters are the Export XT from Medtronic, Pronto V3 from Vascular Solutions, and the QuickCat from Volcano Therapeutics (currently Philips). These catheters, according to their present-day configurations, are shown in Figure 35. Corresponding specifications of these catheters are summarized in Table 4.

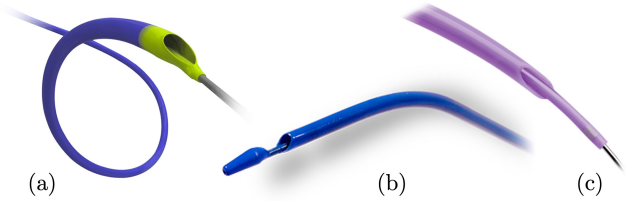

Figure 35: The most commonly used thrombectomy aspiration catheters in 2018, (a) Export XT Aspiration Catheter from Medtronic [20], (b) Pronto V3 Extraction Catheter from Vascular Solutions [24], (c) QuickCat Extract Catheter from Volcano Therapeutics [25]

Table 4: Specifications most commonly used thrombectomy aspiration catheters in 2018 [20] [24] [25]

	Extraction lumen area [mm²]	**Work length [cm]**	**Unique selling points**
Export XT	0.937	140	Deliverability Kink resistance Aspiration power
Pronto V3	0.929	140	Deliverability Vessel wall adhesion prevention
QuickCat	0.858	145	Deliverability Extraction performance

A.2 Prior work

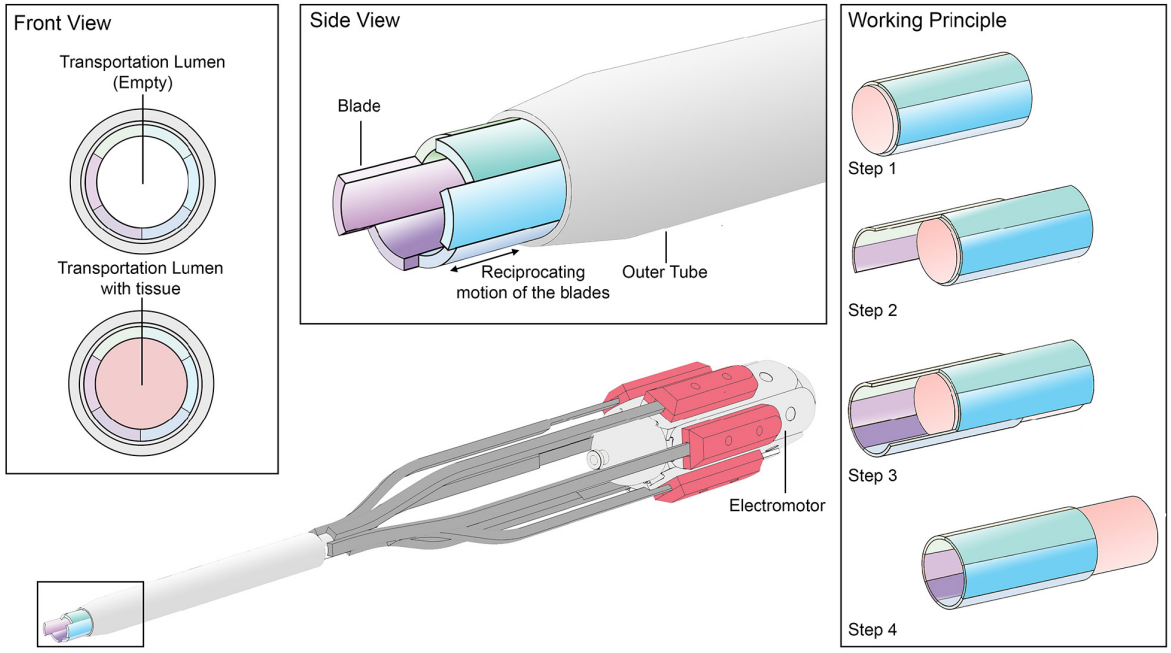

Figure 36: Schematic representation of the wasp-inspired friction-based transportation device developed by Sakes et al. [27]

A.3 Design requirements

Table 5: Design requirements.

Functional requirements

	Requirement	Variable
1	The mechanism enables continuous transportation of tissue	Type of transportation
2	The mechanism enables transportation of tissue with a young's modulus range of 1-110 kPa [4] [2]	Tissue elasticity
3	The mechanism enables a minimum mean transportation rate of 0.25 ∓ 0.04 g/min [27]	Transportation rate
4	The reliability of the device is 90% at minimum	Reliability

Procedural requirements

	Requirement	Variable
5	The device has a maximum outer and minimum inner diameter of ten and five millimetres respectively	Diameter
6	The mechanism enables a minimal work length of 125 cm [18]	Working length
7	The device does not damage surrounding tissue	Damage risk
8	The device is biocompatible for in-vivo surroundings	Bio-compatibility
9	The device is operatable by one user	Handling

Functional wishes

	Wish	Variable
1	The transportation rate does not statistically vary between different tissues within the elasticity range of 1-110 kPa	Transportation rate
2	The mean transportation rate is maximised with a minimum of 6.2 g/min [5]	Transportation rate
3	The reliability of the device is 100%	Reliability
4	The operability of the device is independent of the shaft orientation	Shaft orientation
5	The operability of the device is independent of tissue heterogeneity	Tissue heterogeneity
6	The device enables tissue transportation within a curvature of 90° [16]	Bendability
7	The device does not damage transported tissue	Damage risk

Procedural wishes

	Wish	Variable
8	The mechanism is suitable for a working length of 153 cm [18]	Working length
9	The device is flexible	Bendability
10	The device is reusable	Durability
11	The device is cleanable	Clean-ability
12	The number of components is minimised	Manufacturability

A.4 Ideation sketches

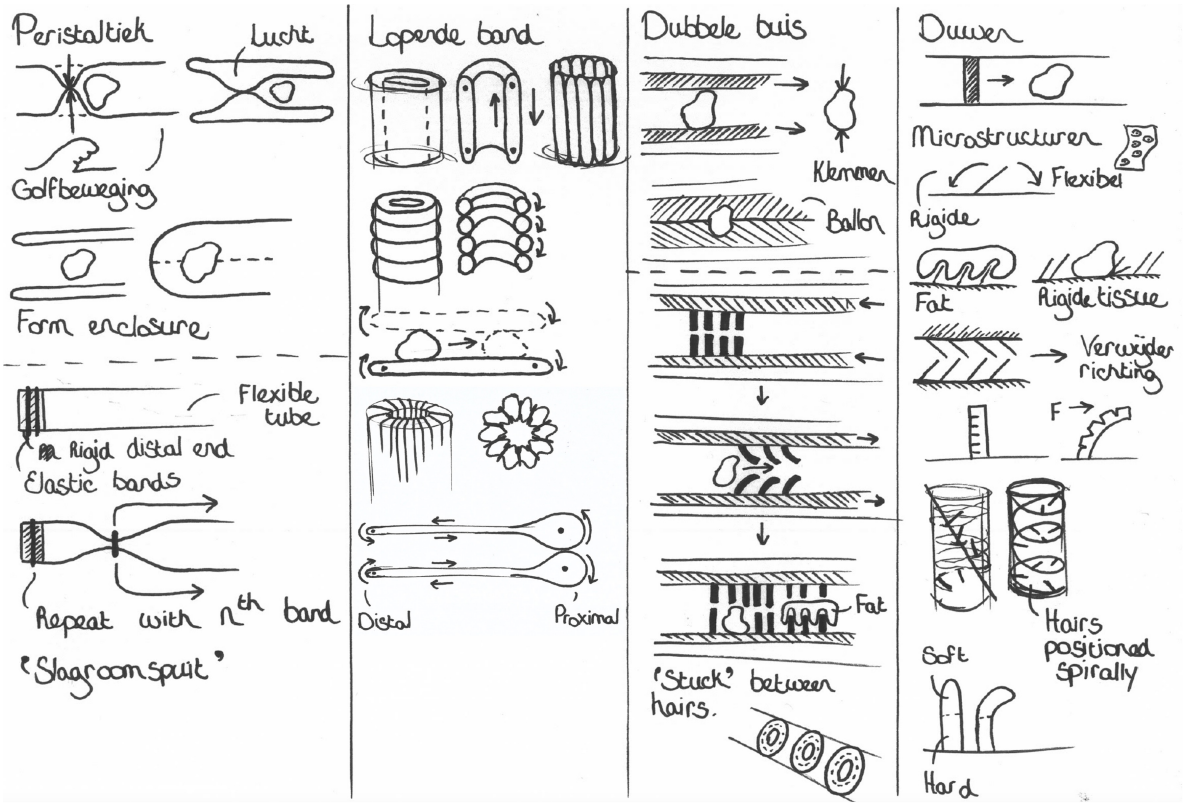

Figure 37: Selection of ideation sketches (1)

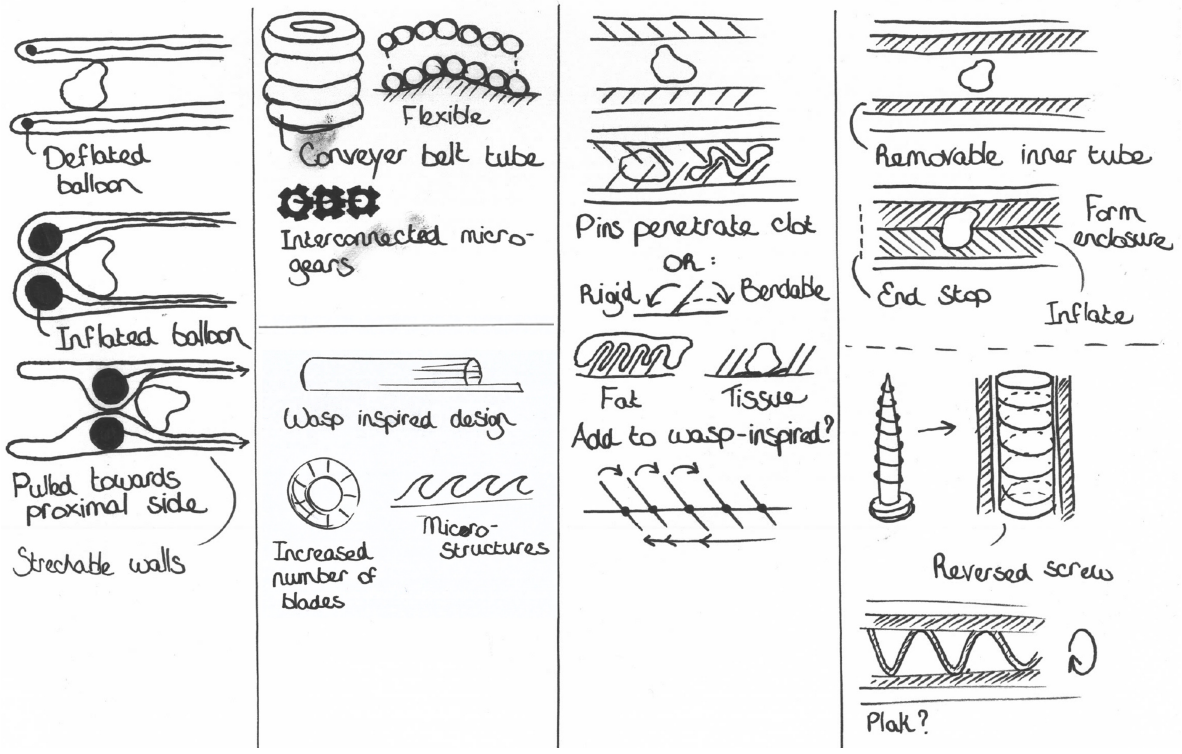

Figure 38: Selection of ideation sketches (2)

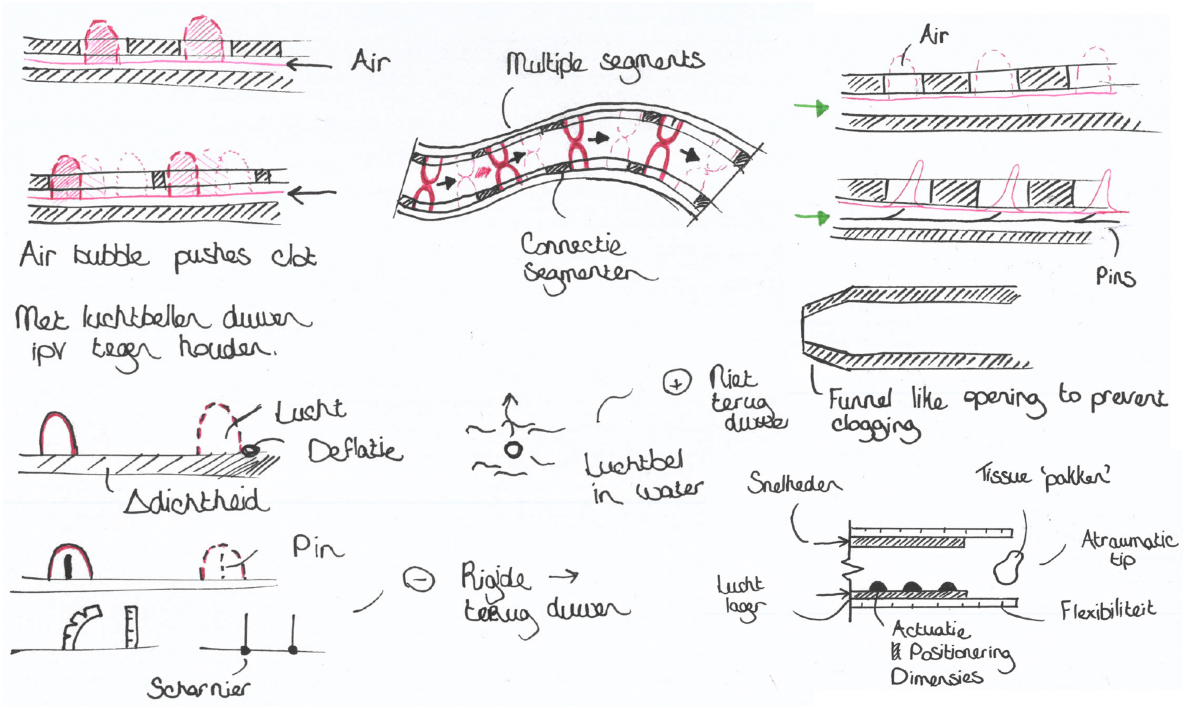

Figure 39: Selection of ideation sketches (3)

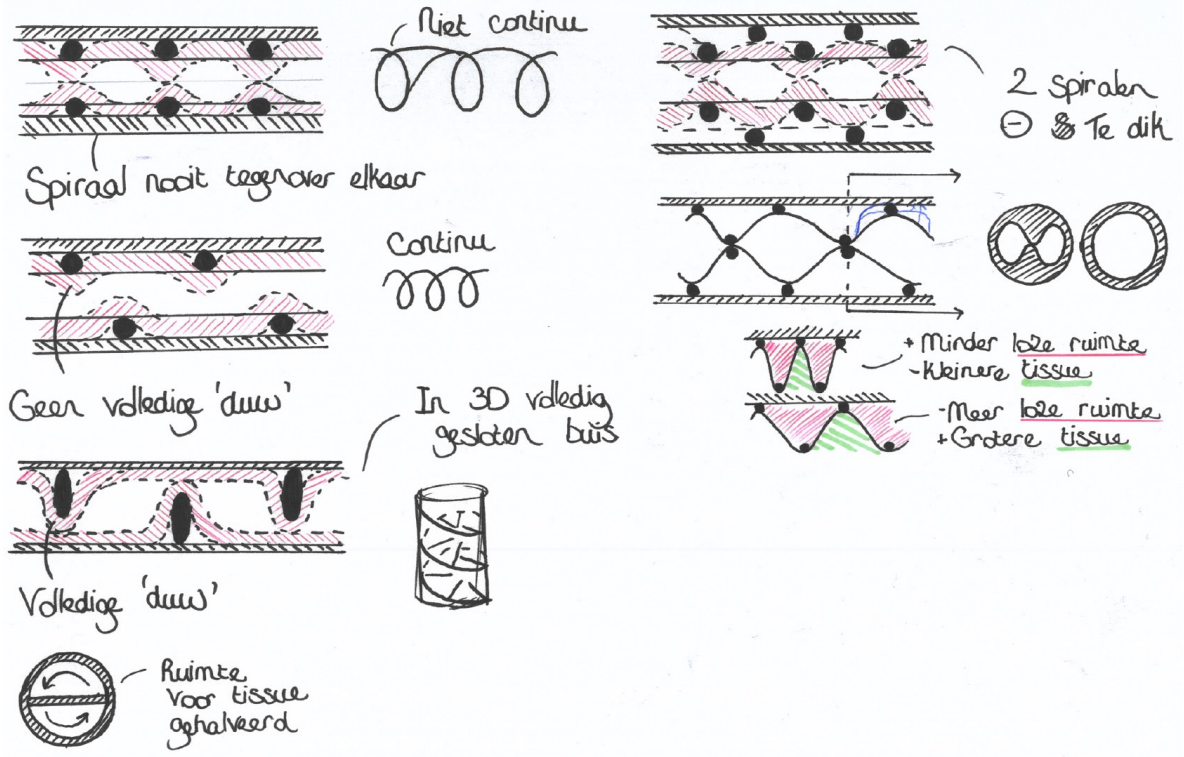

Figure 40: Selection of ideation sketches (4)

A.5 Conceptual design validation

Transportation methods for solids as part of a single-phase system executed by animals can be divided into categories. Namely, transportation due to applied forces, friction, or inertia forces [14]. Three promising ideas were tested by means of rapid prototyping, each implementing one of the strategies seen in nature. The goal is to get a better estimation of the feasibility of each direction. The functionality of each mechanism was tested by transporting gelatine tissue phantoms, for more information see Subsection A.7.

A.5.1 Concept 1 - Transport due to inertia forces

Experiment setup

Within this idea, the feasibility is dependent on the required order of magnitude of the acceleration of the inner tube in order for the tissue to maintain its position. This is achieved whenever the net force is greater than the friction force in between the tissue and tube. Subsequently, the required acceleration of the tube can be calculated through Equation 5. The friction force is approximated through three different setups, shown in Figure 41.

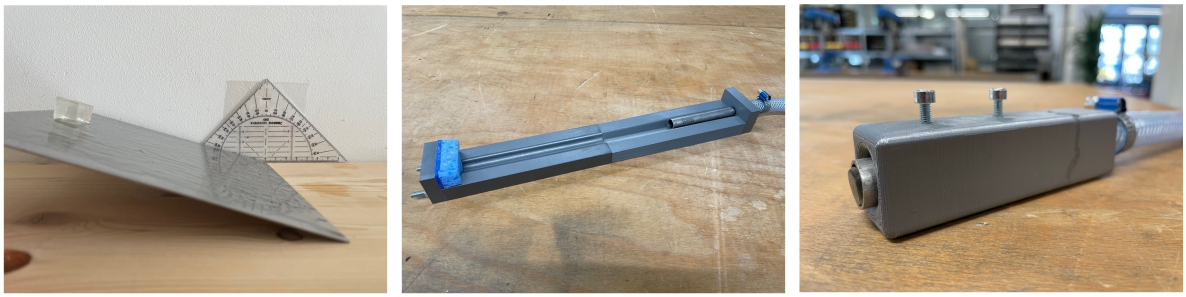

Setup 1 Setup 2 Setup 3

Figure 41: Rapid prototyping conceptual design 1.

$$F = m * a \tag{5}$$

Setup 1

Within the first setup, cubical tissue phantoms of 1 cm^3 are positioned on a sheet of stainless steel. Subsequently, the sheet is tilted gradually until the phantom starts sliding. The experiment is repeated several times, both with and without a lubricating layer (oil) on the sheet. The angle at the moment of movement is used to calculate the friction force.

Setup 2

The second setup mimics the situation in which the velocity of the tube is increased rapidly. Through air pressure, a tube consisting of a tissue phantom is fired within rails. Afterwards, it is checked whether the tissue moved along with the tube or not. In the case of the former, the experiment is repeated with increased air pressure. The corresponding acceleration due to this pressure is calculated with the help of Equation 1 and Equation 5. A hole in the sidewall of the tube prevents pressure buildup on the inside. The tissue phantoms are cylindrically shaped with a length of thirty millimetres and a diameter of thirteen millimetres, subsequently filling up the tube and representing the extreme case with the highest friction between both. The tube is made out of stainless steel.

Setup 3

Lastly, the required force in order to push the tissue phantom outside of the tube is measured. Again, this is done by making use of air pressure. Specific pressure is actuated instantly, after which it is visually detected whether the tissue is shot out of the tube within one second. Whenever this is not the case, the air pressure is increased and the experiment is repeated. The limited time is of importance to prevent air pressure accumulation within the tube. The tissue phantoms were equally shaped as within the previous setup and again a stainless steel tube is used. The corresponding forces within this experiment are visualised within Figure 42(a). It is assumed that at the moment where the tissue phantom is shot out of the tube, the force due to the air pressure is equal to the maximum friction force between the tissue phantom and tube. In order to keep the change in momentum of the tissue sufficiently low, the net force applied to the tube should be higher than the previously calculated friction force. This situation is visualised within Figure 42(b). Corresponding calculations are indicated.

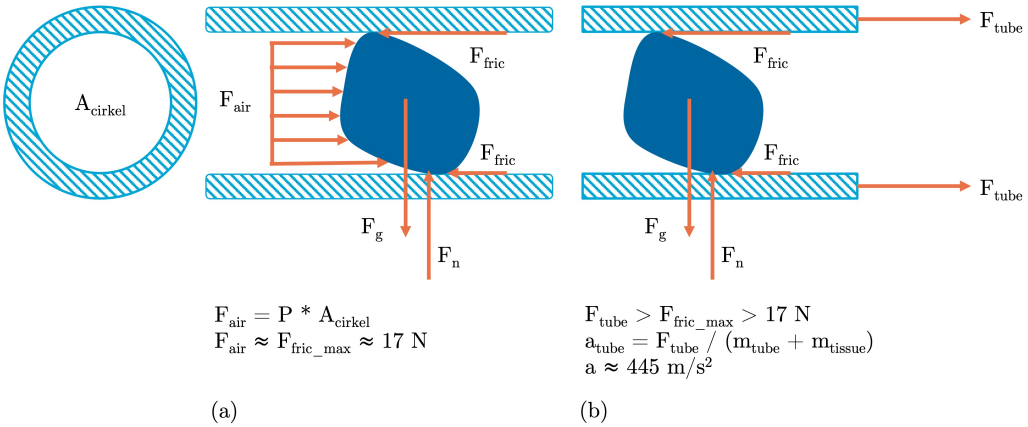

Figure 42: Forces associated with setup 3, conceptual design 2.

Experiment results

Within the former setup, the tissue phantom did not slide on the piece of stainless steel. Instead, the tissue phantom stuck to the sheet, even when the angle was increased to a value over ninety degrees. Whenever movement was detected, the phantom tumbled instead of performing a sliding motion. In the case where oil was used as a lubricating layer, a motion was detected more often. However, the accumulation of oil subsequently decelerated the motion. Within the second setup, no motion of the tissue phantom was detected within the range of air pressure actuation in which the tube stayed within the track. Also, the backfire of the tube during deceleration influenced the position of the phantom. The results of the last experiment are shown in Table 6. The corresponding pressure in order the push the tissue phantom outside of the tube is the delta with respect to the standard atmospheric pressure.

Table 6: Experiment results, setup 3, conceptual design 2.

Tissue phantom w%	21	9	3
Youngst modulus (kPa)	5-10	55	90-100
Tissue phantom weight (g)	3.2	2.5	2.8
Trial number	**Pressure (bar)**		
1	0.284	0.182	0.178
2	0.284	0.178	0.190
3	0.280	0.186	0.176
4	0.270	0.176	0.180
5	0.272	0.176	0.178
Average	0.28	0.18	0.18
Average acceleration of tube ($\frac{m}{s^2}$)	445	418	414

A.5.2 Concept 2 - Transport due to applied forces

Experiment setup

The feasibility of the second idea is dependent on multiple aspects. Low friction between the silicons and tissue is required in order for the latter to move along the tube instead of getting damaged by the peristaltic movement. Also, the silicons on the inside of the tube require sufficient flexibility to accentuate the spiral and subsequently create a steep, wave-like, line. When the slope of the silicons is insufficient, scarce space is sacrificed and the surface area of the applied force on the tissue is reduced. The working principle of this idea is tested by means of the two setups shown in Figure 43, implementing Ecoflex silicons.

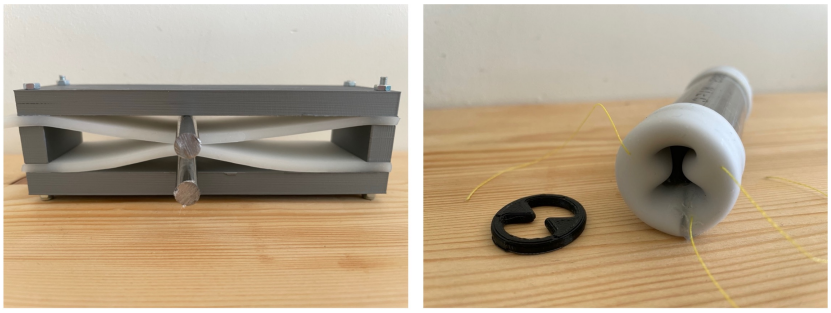

Setup 1 Setup 2

Figure 43: Rapid prototyping conceptual design 2.

Setup 1

Within the first setup, the movement is imitated in a planar situation. Two layers of silicons are clamped and offset within a framework. Subsequently, two axes are positioned between both layers and the framework, lifting the silicons and creating a peek. By displacing both axes, it is attempted to push the tissue phantom in front of it aside. Different types and thicknesses of silicons were tested within this setup.

Setup 2

Secondly, the peristaltic movement is simulated within a tube in a simplified manner. A disc with an open centre, containing two peaks, is inserted within the tube. Subsequently, the silicon layer is stretched within both the disc and tube. By displacing the disc attached to two cords, the peristaltic movement is imitated without requiring a rotating movement from the spirals.

Experiment results

The thin layer of Ecoflex lubricant silicons appeared sticky and stretchable. Due to the former characteristic, it is required to rotate the axis in the direction of translation in order to generate displacement. The rotating movement creates a shallow slope on the side of the tissue phantom whilst almost a ninety-degree angle on the other side. This phenomenon causes the tissue phantom to maintain its position on the silicon and travel over the axis instead of being pushed forward. The stretchiness of the silicons is beneficial in order to accentuate the shape of the axis but simultaneously folds the layer and creates unevennesses.

Within the framework clamping a thicker layer of Ecoflex lubricant silicons, no rotation is required to translate the axis underneath the layer. However, the increased thickness is at the expense of the slope created by the axis underneath the silicon layer. In order to translate the phantom, is required to restrict the tissue phantom to travel over the axis and thus clamp it between two layers of silicons.

Within the second setup, the stretch within the silicon layer is experienced as a disadvantage whilst translating the inner disc. Occasionally, this creates an accumulation of material, subsequently hindering the working principle. Also, the silicon layer does not wrap tightly around the disc.

A.5.3 Concept 3 - Friction based transport

Experiment setup

The feasibility of this idea is dependent on sufficient friction between the tissue and threads. Also, the minimum bending radius of the threads is crucial to guarantee the scalability of the device in a cylindrical setup. Two setups shown in Figure 44, were created to test the working principle.

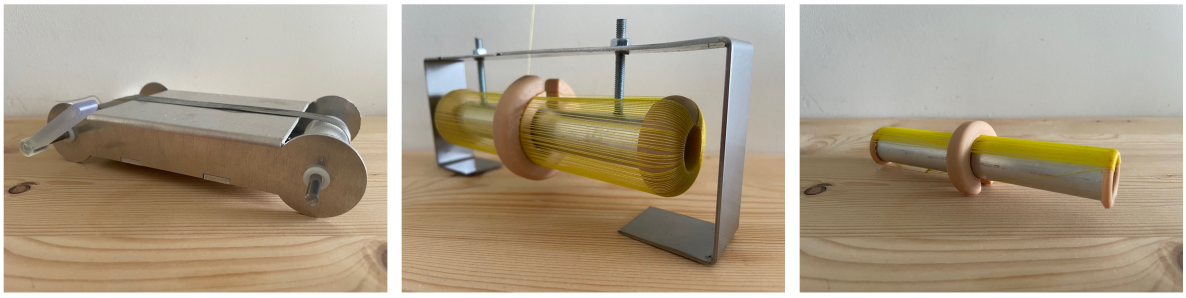

Setup 1 Setup 2(a) Setup 2(b)

Figure 44: Rapid prototyping conceptual design 3.

Setup 1

Again, initially, this idea is tested in a planar situation. A conveyor belt is generated with galvanised stainless steel cables, wrapped around a sheet metal base. Different tissue phantoms are positioned on the belt and subsequently transported to the other side. The minimum bending radius of the wires is not approximated within this setup, this variable is made sufficiently large to ensure rotation.

Setup 2

The second setup mimics the transportation mechanism within the tubular configuration. A PTFE-coated and pre-stretched, polyethene fishing thread is wrapped around an aluminium tube with an inner and outer diameter of 16 and 20 millimetres respectively. The outer sides of the tube are encapsulated with a doughnut-shaped ring containing grooves for alignment of the treads. Subsequently, the threads are attached to an outer ring, enabling actuating the rotation of the threads in a repelling motion. Since the threads rotate via the outside of the tube, the device is hung up within a framework. This gives the opportunity to have a grip on the tubular mechanism and actuate the motion. Again, the transportation of the three tissue phantoms is tested within this setup.

Experiment results

The tissue phantoms are transported along the galvanised stainless steel cables within the first setup. Occasionally, the phantoms fell off the belt, which is automatically prevented within the tubular version. During production, tensioning the cables and subsequently attaching the ends to each other was found challenging. Also, it is noted that kinking of the stainless steel wire should be prevented. The initial design of the second setup did not enable the rotation of the wires. This is due to the threads experiencing too much friction. Therefore, it is decided to make a second version, in which the amount of thread is reduced. This time, actuation of the threads by translating the outer ring is enabled, even though a significant amount of force is required. The tissue phantoms are transported without slipping within the tube.

A.6 Assembly

Within Figure 45, snapshots of the assembling procedure are shown. Firstly, the cap is screwed onto the cone in its extremity, after which the gearbox is positioned and temporarily fastened with tape (1-4). Next, a sufficient amount of thread is trimmed of which one end is attached to the inner tube (5). Subsequently, the thread is weaved through the device; underneath the spacer (6), into the cone (7), through the gear base (8), aligned within the designated V-groove (9), positioned on the inside of the cone (10), pulled through the inner tube (11) and aligned within the tip (12). This process is repeated a total of ten times, connecting all loops in a continuous manner. The thread is tensioned manually frequently throughout the process to ensure proper positioning. It is recommended to fasten the loops of thread throughout assembly with small pieces of tape to prevent the concerning from loosening and exiting its associated grooves. Whenever completed, both ends of the thread are tied to one another by means of a flat knot (13-14). Excessive ends are trimmed after which super glue is added to fill the remaining gaps (15-16). Subsequently, the remaining tape can be removed, the outer tube and internal gear can be added, the device can be tensioned, and the device is ready for usage.

Figure 45: Snapshots made throughout the assembly of the device.

A.7 Tissue phantoms

In order to enable experimental validation of the created prototypes, gelatine tissue phantoms were created, mimicking the physical properties of tissue encountered during MIS. The study of Karimi et al. relates different weight percentages of gelatine to corresponding compressive young's moduli, as shown in Figure 46.

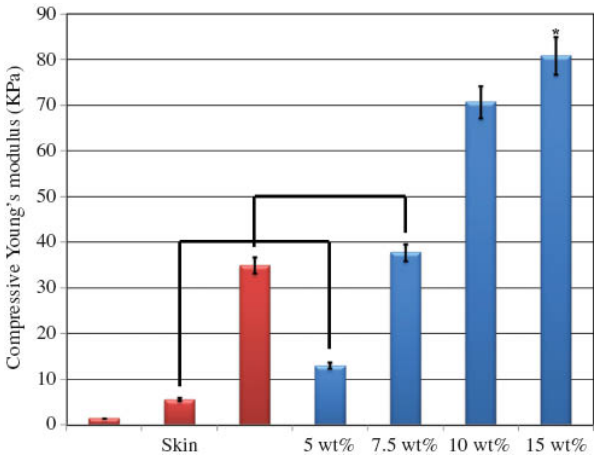

Figure 46: Weight percentages of gelatine phantoms and corresponding compressive Young's moduli [13].

Based on these outcomes, the relations displayed in Table 7 are assumed within this research. The corresponding tissue elasticity of the two extremities is specified within a range since these values are not literally included within the before-mentioned resource and are thus based on estimation.

Table 7: Assumed tissue elasticity properties of created gelatine tissue phantoms.

Gelatine weight percentage (wt%)	Tissue elasticity (kPa)
3	1-10
9	55
12	100-110

Solid sheets of 'Dr. Oetker' gelatine was used to create the desired gelatine tissue phantoms. Firstly, 3, 9, or 12 grams of gelatine is added within a pot positioned on a weighing scale. Subsequently, ten drops of red food colouring are added, whilst maintaining to monitor the corresponding weight. Next, water is added, until the weight of each batch results in one hundred grams. Approximately, 97, 91, and 88 grams of water are thus added for the different categories respectively. It is assumed that the food colouring has no influence on the resulting properties and is comparable to water. After all elements are added, the gelatine sheets are left to rest within the liquid for five minutes, after which the mixture is slowly heated (below the boiling point) until the gelatine is completely resolved. Afterwards, the liquid is poured within the created moulds and positioned within the refrigerator for a minimum and maximum of 12 and 24 hours respectively. The resulting gelatine tissue phantoms as shown in Figure 47, are extruded shortly prior to the execution of the experiments, to prevent deviating properties. The cylinders have a diameter and height of five and fifteen millimetres respectively.

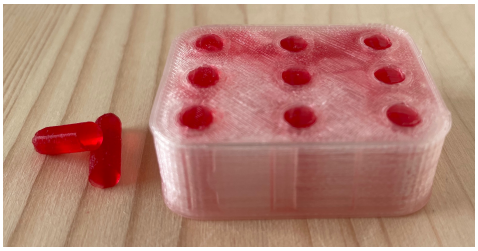

Figure 47: Gelatine tissue phantoms and corresponding mould.

A.8 Instrument failure

Within Figure 48, snapshots of instrument failure experienced in between experiments are shown. Within the first two images, the horizontal axis of the bevel gear joined to the axis clamping the thread is loosened from the gear base. Subsequently, due to the thread tension, the corresponding gear is dislocated. This occurred twice throughout the executed experiments. Within the third image, the stainless steel wire is partially damaged. Due to the continuous rotation, the concerning thread string accumulates at the tip, eventually prohibiting the operability of the device. Within the last two images, it can be seen that the tip add-on is damaged due to the cutting motion of the rotating thread.

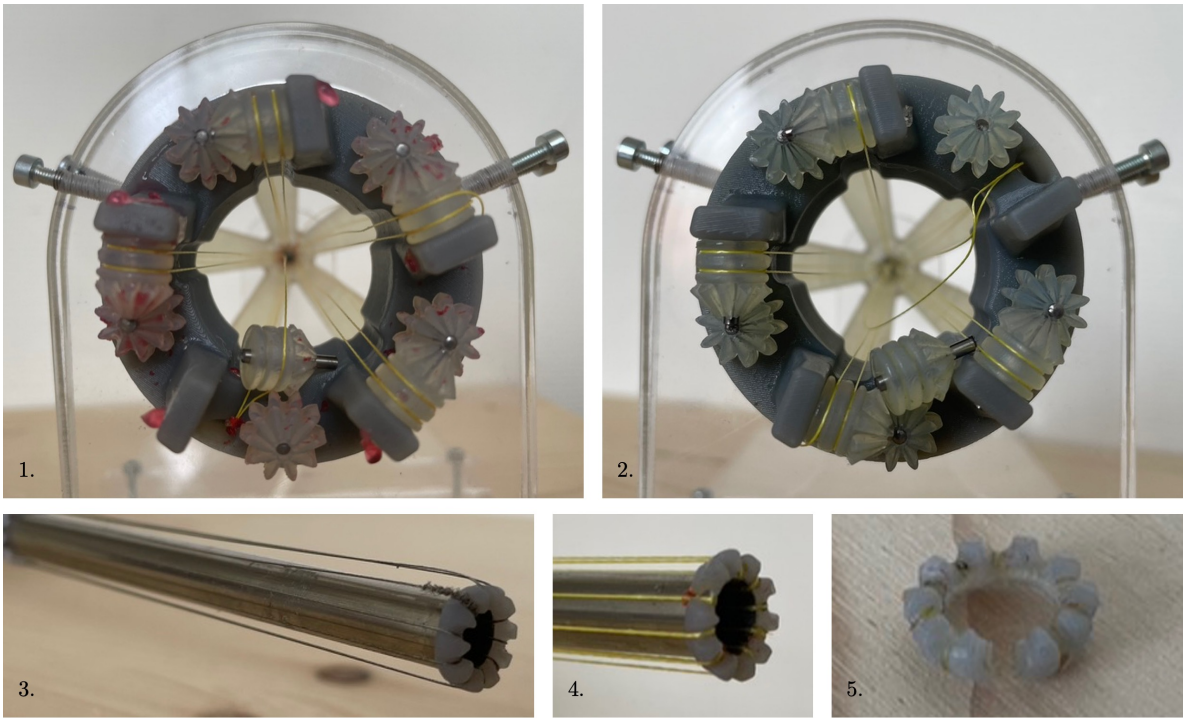

Figure 48: Snapshots of troubleshooting in between experiments.

A.9 Experiment data

The measured transportation times of all experiments are shown within Figure 49. The corresponding data analysis within Matlab is shown in the subsequent pages.

Setup	Voltage	Weight percentage	Angle	Moon shaped	RPM	Testresult 1	Testresult 2	Testresult 3	Testresult 4	Testresult 5	Testresult 6	Testresult 7	Testresult 8	Testresult 9	Testresult 10	Average
Setup 1	8,5	12	0	NO	19,1	00:04,3	00:04,1	00:04,3	00:04,2	00:03,8	00:04,0	00:04,0	00:03,6	00:03,9	00:04,2	00:04,0
Setup 2	8,5	9	0	NO	18,2	00:04,6	00:04,2	00:03,9	00:03,9	00:04,1	00:03,9	00:04,2	00:04,4	00:04,4	00:04,7	00:04,2
Setup 3	8,5	3	0	NO	19,1	00:03,1	00:03,4	00:04,1	00:07,8	00:03,6	00:06,7	00:03,6	00:09,7	00:15,5	00:20,0	00:07,8
Setup 4	11	12	0	NO	26,7	00:02,5	00:02,7	00:02,6	00:02,4	00:02,6	00:02,7	00:02,8	00:02,6	00:02,6	00:02,6	00:02,6
Setup 5	11	9	0	NO	27,2	00:02,5	00:02,8	00:02,8	00:02,7	00:02,8	00:02,6	00:02,8	00:02,8	00:02,9	00:02,9	00:02,8
Setup 6	11	3	0	NO	22,8	00:03,6	00:28,5	00:05,0	00:04,2	00:03,9	00:03,6	00:05,3	00:04,4	00:05,2	00:05,5	00:06,9
Setup 7	13,5	12	0	NO	36,5	00:02,3	00:02,0	00:01,9	00:02,1	00:01,9	00:01,9	00:02,0	00:02,2	00:02,0	00:02,0	00:02,0
Setup 8	13,5	9	0	NO	35,7	00:01,9	00:04,1	00:02,3	00:02,0	00:02,0	00:02,1	00:01,9	00:02,0	00:02,1	00:02,0	00:02,2
Setup 9	13,5	3	0	NO	33,7	00:02,7	00:02,2	00:02,5	00:02,3	00:02,3	00:02,2	00:02,2	00:02,3	00:02,3	00:02,3	00:02,3
Setup 10	11	12	20	NO	22,3	00:03,3	00:03,3	00:03,4	00:03,6	00:03,4	00:03,4	00:03,4	00:03,3	00:03,4	00:03,6	00:03,4
Setup 11	11	9	20	NO	23,8	00:03,2	00:03,6	00:03,4	00:05,6	00:03,3	00:03,1	00:03,2	00:03,3	00:03,6	00:03,2	00:03,5
Setup 12	11	3	20	NO	21,2	00:05,5	00:04,9	00:05,2	00:04,3	00:03,8	00:04,1	00:04,4	00:03,8	00:04,1	00:04,2	00:04,4
Setup 13	11	9	0	YES	21,8	00:03,5	00:03,4	00:03,4	00:03,3	00:03,4	00:03,4	00:03,5	00:03,5	00:03,6	00:03,8	00:03,5

Figure 49: Extracted experimental data.

```
%% Variables
l = 135;                %Transported distance tissue phantom in mm
Theeth_g1 = 54;         %Number of theeth internal gear
Theeth_g2 = 10;         %Number of theeth spur and bevel gears
r_katrol = 3.025;       %mm
r_katrol_scaled = 3.43; %mm

%% Experiment data
T_8V_3 = [3.1; 3.4; 4.1; 7.8; 3.6; 6.7; 3.6; 9.7; 15.5; 20.0];
T_8V_9 = [4.6; 4.2; 3.9; 3.9; 4.1; 3.9; 4.2; 4.4; 4.4; 4.7];
T_8V_12 = [4.3; 4.1; 4.3; 4.2; 3.8; 4.0; 4.0; 3.6; 3.9; 4.2];

T_11V_3 = [3.6; 28.5; 5.0; 4.2; 3.9; 3.6; 5.3; 4.4; 5.2; 5.5];
T_11V_9 = [2.5; 2.8; 2.8; 2.7; 2.8; 2.6; 2.8; 2.8; 2.9; 2.9];
T_11V_12 = [2.5; 2.7; 2.6; 2.4; 2.6; 2.7; 2.8; 2.6; 2.6; 2.6];

T_13V_3 = [2.7; 2.2; 2.5; 2.3; 2.3; 2.2; 2.2; 2.3; 2.3; 2.3];
T_13V_9 = [1.9; 4.1; 2.3; 2.0; 2.0; 2.1; 1.9; 2.0; 2.1; 2.0];
T_13V_12 = [2.3; 2.0; 1.9; 2.1; 1.9; 1.9; 2.0; 2.2; 2.0; 2.0];

T_20deg_3 = [5.5; 4.9; 5.2; 4.3; 3.8; 4.1; 4.4; 3.8; 4.1; 4.2];
T_20deg_9 = [3.2; 3.6; 3.4; 5.6; 3.3; 3.1; 3.2; 3.3; 3.6; 3.2];
T_20deg_12 = [3.3;  3.3; 3.4; 3.6; 3.4; 3.4; 3.4; 3.3; 3.4; 3.6];

T_half_9 = [3.5; 3.4; 3.4; 3.3; 3.4; 3.4; 3.5; 3.5; 3.6; 3.8];

RPM = [19.1; 18.2; 19.1; 26.7; 27.2; 22.8; 36.5; 35.7; 33.7; 22.3; 23.8; 21.2; 21.8];
t_avg = [4.0; 4.2; 7.8; 2.6; 2.8; 6.9; 2.0; 2.2; 2.3; 3.4; 3.5; 4.4; 3.5];

%% Data categorisation
T_8V = [T_8V_3 T_8V_9 T_8V_12];
T_11V = [T_11V_3 T_11V_9 T_11V_12];
T_13V = [T_13V_3 T_13V_9 T_13V_12];
T_20deg = [T_20deg_3 T_20deg_9 T_20deg_12];

T_3wt = [T_8V_3 T_11V_3 T_13V_3];
T_9wt = [T_8V_9 T_11V_9 T_13V_9];
T_12wt = [T_8V_12 T_11V_12 T_13V_12];

%% Conversion from time to velocity
V_8V = l./T_8V;
V_11V = l./T_11V;
V_13V = l./T_13V;

V_20deg = l./T_20deg;
V_11V_9 = l./T_11V_9;
V_11V_9half = l./T_half_9;

V_3wt = l./T_3wt;
V_9wt = l./T_9wt;
V_12wt = l./T_12wt;

%% Boxplot - Influence rotational velocity
figure(1)

medianV = [median(V_3wt), median(V_9wt), median(V_12wt)];
meanV = [mean(V_3wt), mean(V_9wt), mean(V_12wt)];
stdV = [std(V_3wt), std(V_9wt), std(V_12wt)];
V = {V_8V V_11V V_13V};
y = [1,2,3,5,6,7,9,10,11];

boxplotGroup(V, 'PrimaryLabels', {'19.1' '22.8' '33.7' '18.2' '27.2' '35.7' '19.1' '26.7'↙
'36.5'}, ...
```

```
  'SecondaryLabels',{'3 wt%', '9 wt%','12 wt%'},'GroupLabelType', 'Vertical')

title('Tissue phantom transportation velocities with varying rotational velocities')
xlabel('Rotational velocity [RPM]')
ylabel('Transportation velocity [mm/s]')

color1 = [0.3010 0.7450 0.9330; 0.3010 0.7450 0.9330; 0.3010 0.7450 0.9330;
    0.9290 0.6940 0.1250; 0.9290 0.6940 0.1250; 0.9290 0.6940 0.1250;
    0.8500 0.3250 0.0980; 0.8500 0.3250 0.0980; 0.8500 0.3250 0.0980];

h = findobj(gca,'Tag','Box');

for j=1:length(h)
    patch(get(h(j),'XData'),get(h(j),'YData'),color1(j,:),'FaceAlpha',.5);
end

hold on
scatter (y,medianV,'.','red')
hold on
scatter (y,meanV,'x','black')
hold off

%% Boxplot - Influence instrument orientation
figure(2)

medianV = [median(V_11V(:,1)), median(V_20deg(:,1)), median(V_11V(:,2)), median(V_20deg(:,2))↙
median(V_11V(:,3)), median(V_20deg(:,3))];
meanV = [mean(V_11V(:,1)), mean(V_20deg(:,1)), mean(V_11V(:,2)), mean(V_20deg(:,2)) mean↙
(V_11V(:,3)), mean(V_20deg(:,3))];
y = [1,2,4,5,7,8];

V_20 = {V_11V V_20deg};
boxplotGroup(V_20, 'PrimaryLabels', {'22.8' '21.2' '27.2' '23.8' '26.2' '22.3'}, ...
  'SecondaryLabels',{'3 wt%', '9 wt%','12 wt%'},'GroupLabelType', 'Vertical')

title('Tissue phantom transportation velocities with varying instrument orientations')
xlabel('Rotational velocity [RPM]')
ylabel('Transportation velocity [mm/s]')

color2 = [0.3010 0.7450 0.9330; 0.3010 0.7450 0.9330; 0.3010 0.7450 0.9330;
    0.8500 0.3250 0.0980; 0.8500 0.3250 0.0980; 0.8500 0.3250 0.0980];

h = findobj(gca,'Tag','Box');

for j=1:length(h)
    patch(get(h(j),'XData'),get(h(j),'YData'),color2(j,:),'FaceAlpha',.5);
end

hold on
scatter (y,medianV,'.','red')
hold on
scatter (y,meanV,'x','black')
hold off

%% Boxplot - Influence tissue phantom shape
figure(3)

V_half = {V_11V_9 V_11V_9half};
medianV = [median(V_11V(:,2)), median(V_11V_9half)];
meanV = [mean(V_11V(:,2)), mean(V_11V_9half)];
y = [1,2];

boxplotGroup(V_half, 'PrimaryLabels', {'27.2' '21.8'}, ...
```

```
  'SecondaryLabels',{'9 wt%'},'GroupLabelType', 'Vertical')

title('Tissue phantom transportation velocities with different shapes')
xlabel('Rotational velocity [RPM]')
ylabel('Transportation velocity [mm/s]')

color3 = [0.3010 0.7450 0.9330; 0.8500 0.3250 0.0980; 0.3010 0.7450 0.9330;
    0.8500 0.3250 0.0980; 0.8500 0.3250 0.0980; 0.8500 0.3250 0.0980];

h = findobj(gca,'Tag','Box');

for j=1:length(h)
    patch(get(h(j),'XData'),get(h(j),'YData'),color3(j,:),'FaceAlpha',.5);
end

hold on
scatter (y,medianV,'.','red')
hold on
scatter (y,meanV,'x','black')
hold off

%% Statistical analysis
%Rotational velocities within groups - oneway annova
wt3 = [V_8V(:,1),V_11V(:,1),V_13V(:,1)];
wt9 = [V_8V(:,2), V_11V(:,2),V_13V(:,2)];
wt12 = [V_8V(:,3), V_11V(:,3),V_13V(:,3)];

wt3results = anova1(wt3); %3wt
wt9results = anova1(wt9); %9wt
wt12results = anova1(wt12); %12wt

%Instrument orientation - independent t-test
[h1,p1] = ttest(V_20deg(:,1),V_11V(:,1)); %3wt
[h2,p2] = ttest(V_20deg(:,2),V_11V(:,2)); %9wt
[h3,p3] = ttest(V_20deg(:,3),V_11V(:,3)); %12wt

%Phantom shape
[h4,p4] = ttest(V_11V_9half,V_11V(:,2)); %12wt

%% Transportation velocities in [g/min]
m_3wt = 0.3;    %g
m_9wt = 0.3;    %g
m_12wt = 0.3;   %g

V_m_3wt = m_3wt./T_3wt(:,3)*60;
V_m_9wt = m_9wt./T_9wt(:,3)*60;
V_m_12wt = m_12wt./T_12wt(:,3)*60;

mean(V_m_3wt);
mean(V_m_9wt);
mean(V_m_12wt);

std(V_m_3wt);
std(V_m_9wt);
std(V_m_12wt);

%% Efficiency
%Efficiency according computational model
rpm_g2 = (Theeth_g1/Theeth_g2).*RPM;
c_katrol = 2*pi*r_katrol;
rotations = l/c_katrol;
t_theoretical = rotations./rpm_g2*60;
```

```
efficiency = (t_theoretical./t_avg)*100;

%Scaled efficiency
c_katrol_scaled = 2*pi*r_katrol_scaled;
rotations_scaled = l/c_katrol_scaled;
t_theoretical_scaled = rotations_scaled./rpm_g2*60;

efficiency_scaled = (t_theoretical_scaled./t_avg)*100;
```

A.10 Additive manufacturing

Throughout this research, two different types of additive manufacturing devices were used, the Ultimaker S3 and Formlabs 3+ SLA printer. The former is mainly used for rapid prototyping, whilst the latter printer is used for more detailed parts and for iterating materials. Contrary to the Ultimaker, in which layers of melted filament are deposited onto the building plate through the nozzle, the resin is cured by means of a laser within the SLA printer. After the component is fully printed, the element is post-treated by rising off uncured resin within a bath of alcohol and curing the component at elevated temperatures for a specific amount of time. Within Table 8, the resins used in this research with corresponding specifications and beneficial features decisive within this process are listed. The implemented resins within the final design, 'Durable' and 'Tough 1500', are both bio-compatible [1].

Table 8: Resins

Resin	Tensile strength (MPa)	Tensile modulus (GPa)	Flexural) modulus (GPa)	Highlighted feature
Durable	28	1.0	0.66	Low friction
Clear	65	2.8	2.2	Transparency
Model	61	2.7	2.5	± 35 µm precision
Tough 1500	33	1.5	1.4	Stiff and pliable

A.11 Forces bevel gears

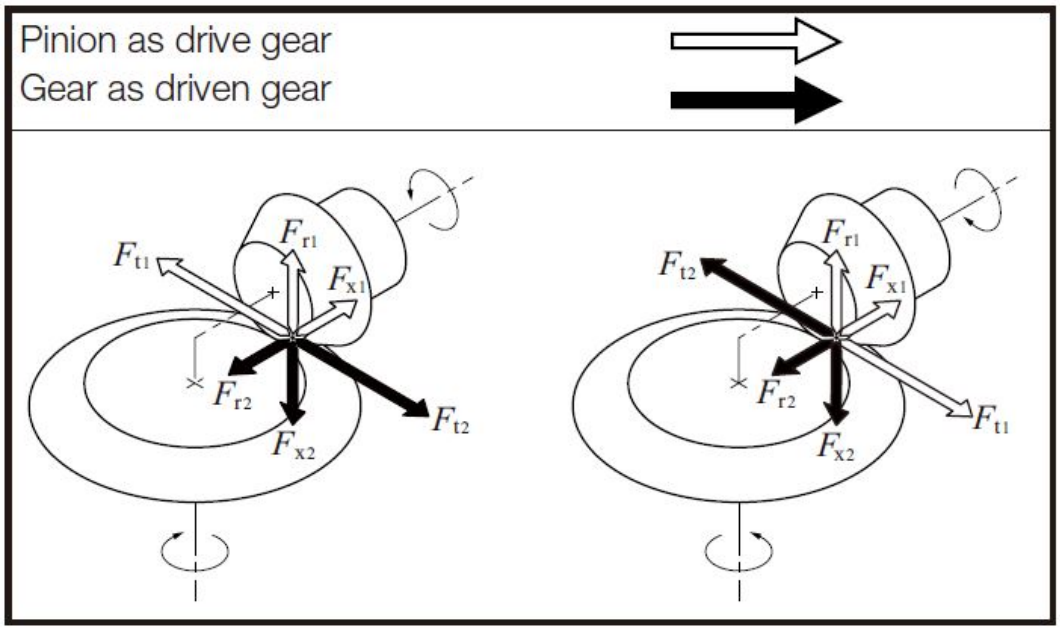

Figure 50: Forces bevel gears [10].

A.12 Components

Within this section, a selection of drawings of the components manufactured through additive manufacturing is shown. Relevant dimensions are indicated in millimetres and images are scaled according to page space. Note that the requirements of official technical drawings are not satisfied.

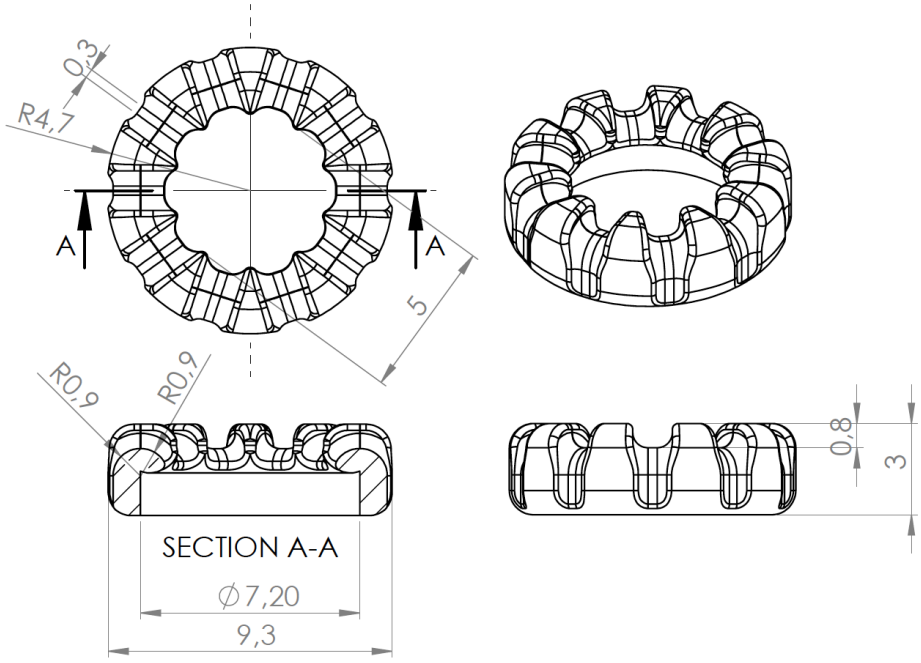

Figure 51: Selection of component views and dimensions (mm), C2 - Tip

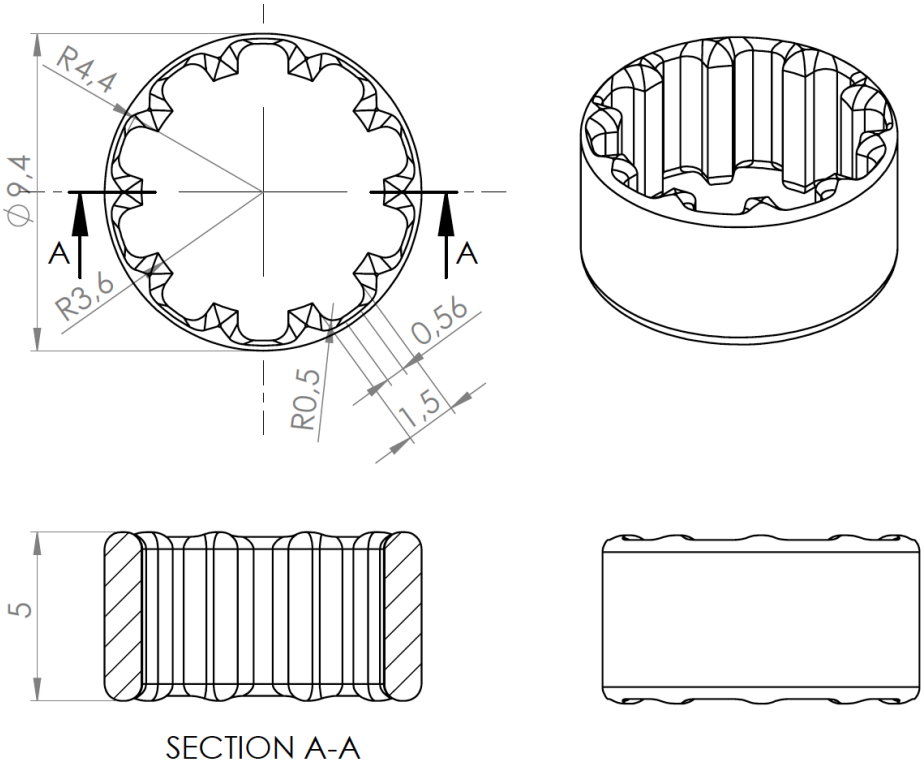

Figure 52: Selection of component views and dimensions (mm), C3 - Spacer

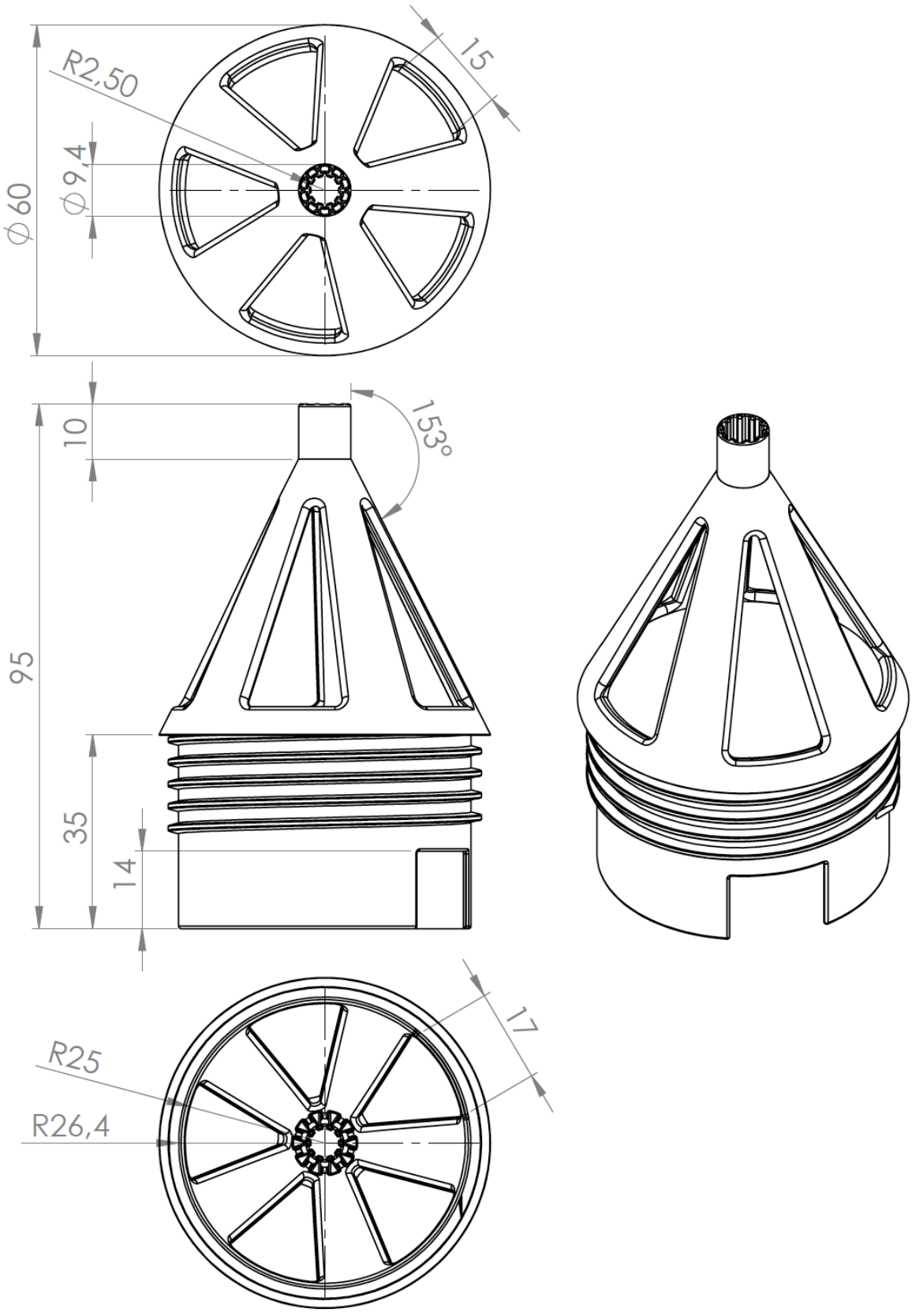

Figure 53: Selection of component views and dimensions (mm), C5 - Cone

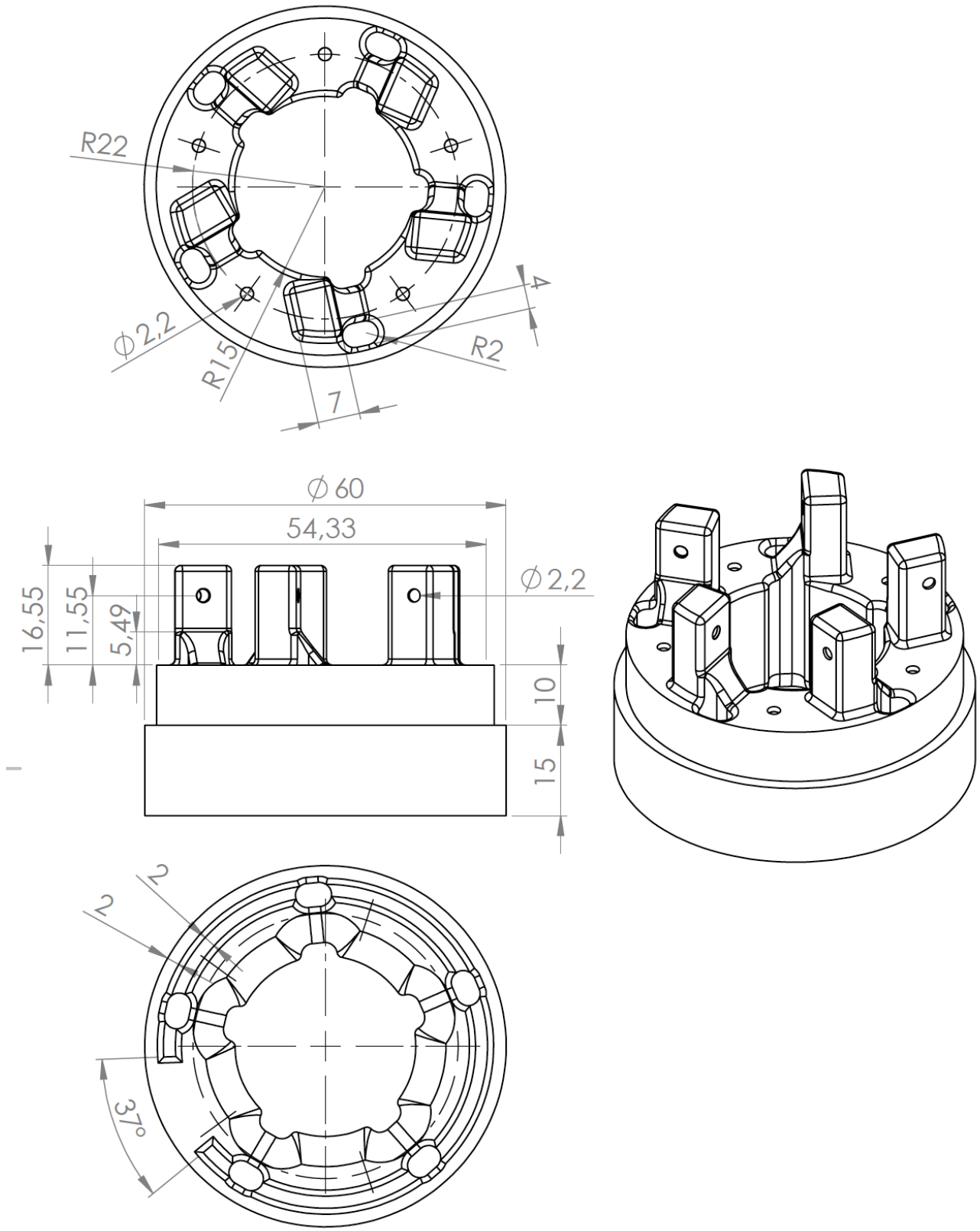

Figure 54: Selection of component views and dimensions (mm), C7 - Gear base

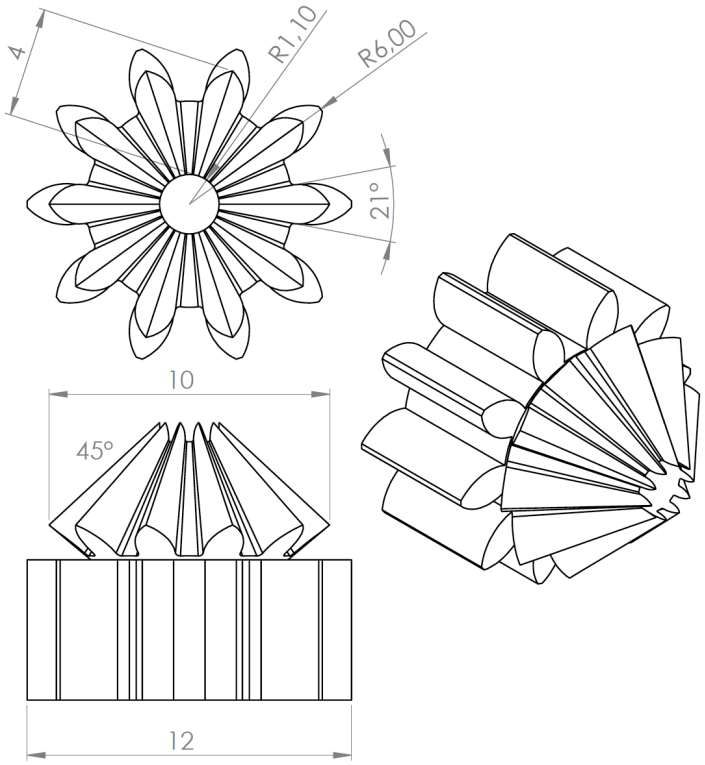

Figure 55: Selection of component views and dimensions (mm), C8 - Gears (1)

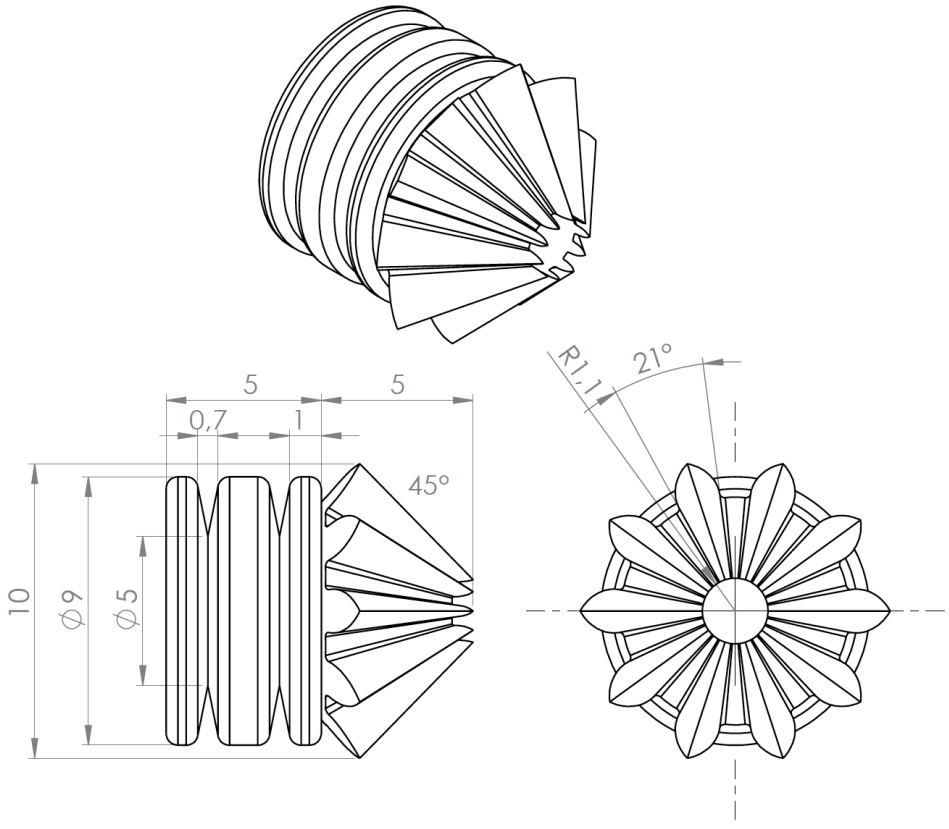

Figure 56: Selection of component views and dimensions (mm), C8 - Gears (2)

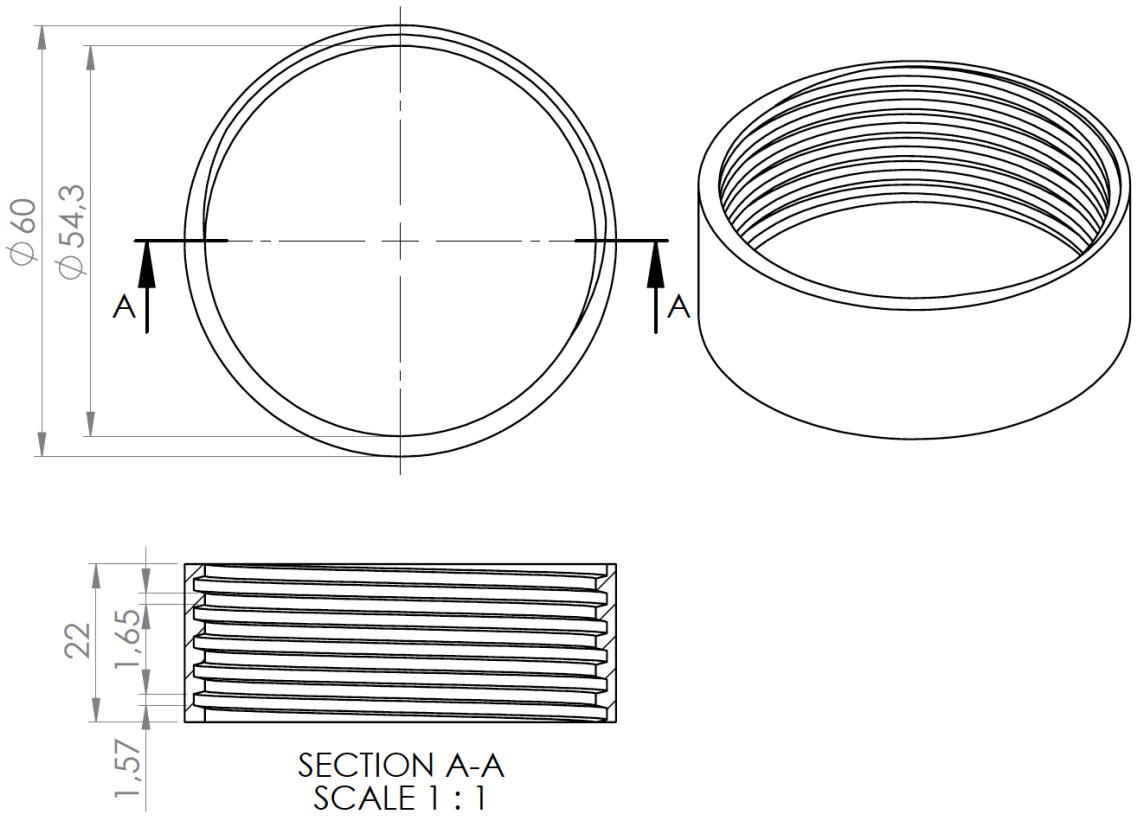

Figure 57: Selection of component views and dimensions (mm), C6 - Cap

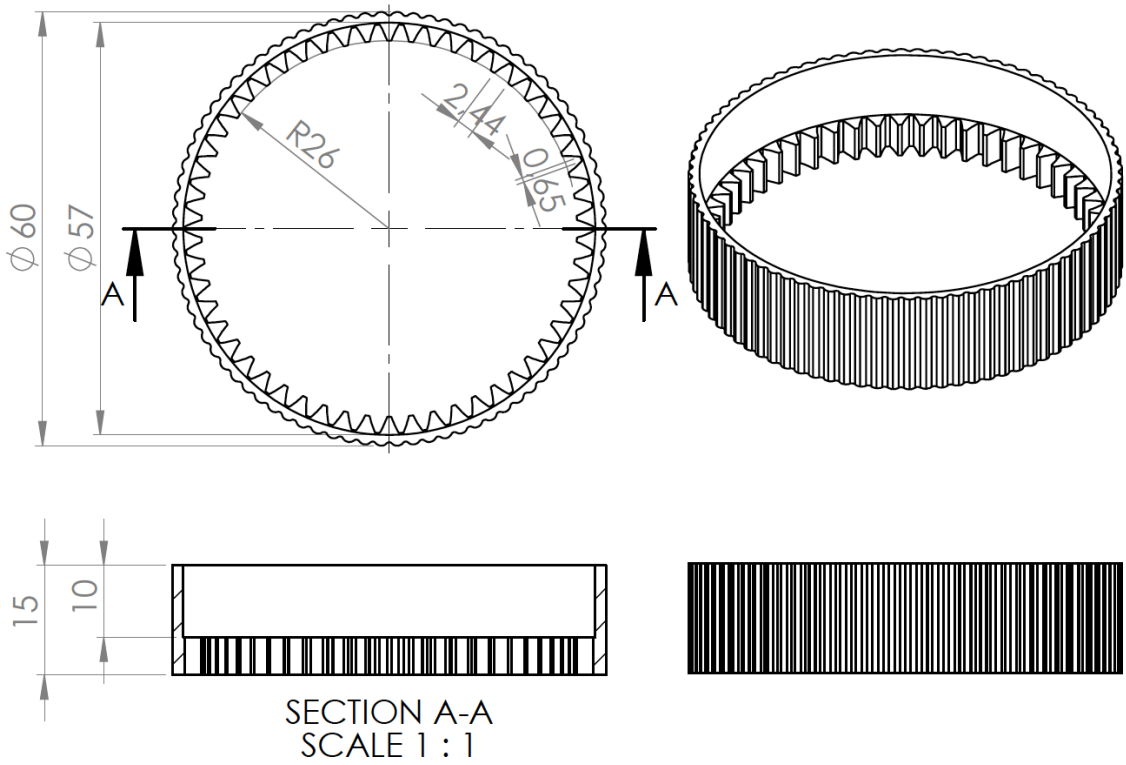

Figure 58: Selection of component views and dimensions (mm), C9 - Internal gear

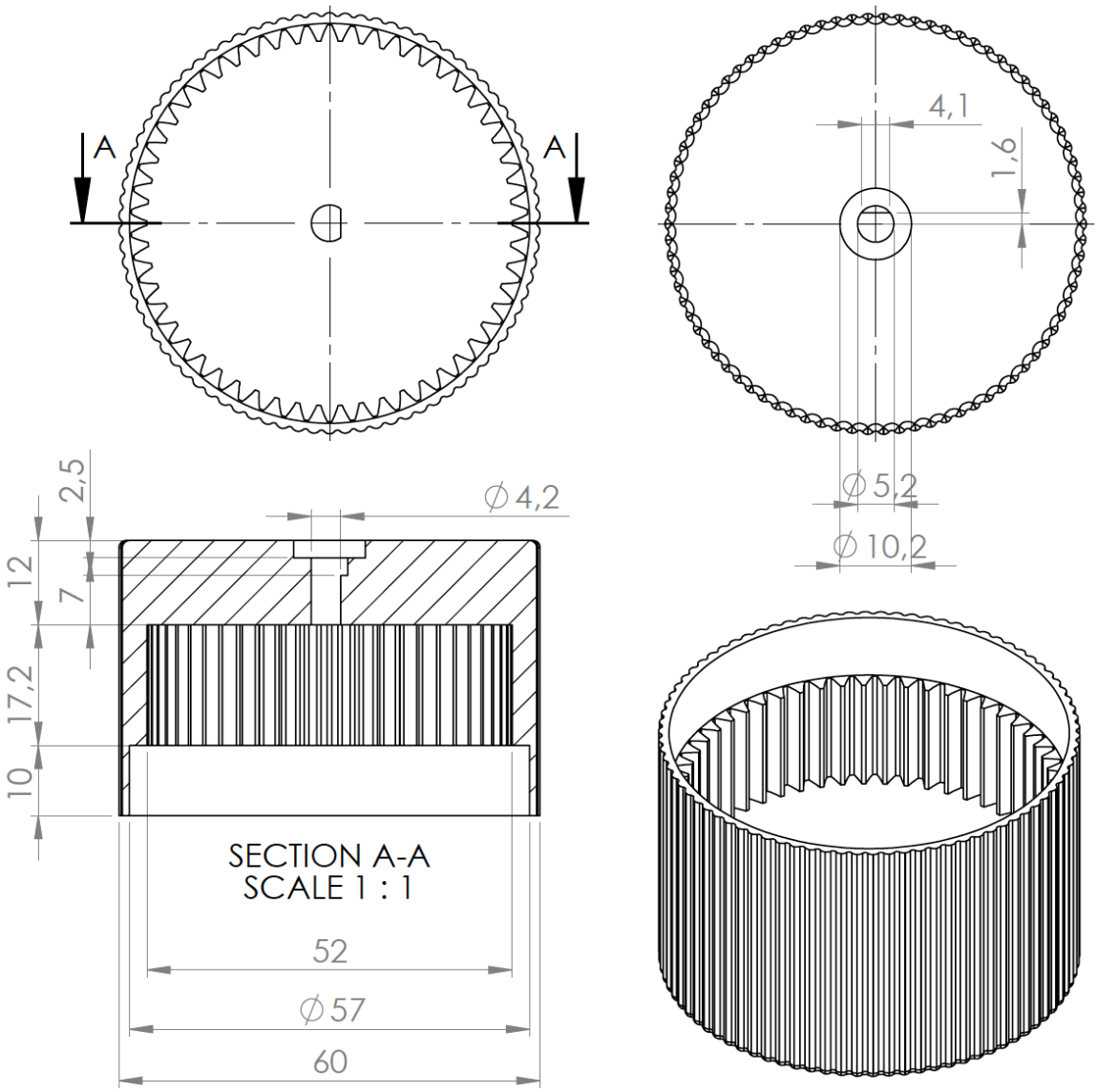

Figure 59: Selection of component views and dimensions (mm), C9 - Internal gear 2